



UNIVERSIDADE D  
COIMBRA



Joana Maria Vaz Ramos

**SYNTHESIS OF SUPERPARAMAGNETIC MESOPOROUS  
SILICA NANOPARTICLES TO MEDIATE ANTITUMOUR  
STRATEGIES**

Dissertation of the Integrated Master's Degree in Chemical Engineering,  
Specialization in Biosystems, with the orientation of Luísa Maria Rocha Durães, PhD,  
and Henrique Manuel dos Santos Faneca, PhD, and presented to the Department of  
Chemical Engineering of the Faculty of Sciences and Technology of the University of  
Coimbra.

September 2018



Department of Chemical Engineering

# SYNTHESIS OF SUPERPARAMAGNETIC MESOPOROUS SILICA NANOPARTICLES TO MEDIATE ANTITUMOUR STRATEGIES

Joana Maria Vaz Ramos

Dissertation of the Integrated Master's Degree in Chemical Engineering, Specialization in Biosystems, with the orientation of Luísa Maria Rocha Durães, PhD, and Henrique Manuel dos Santos Faneca, PhD, and presented to the Department of Chemical Engineering of the Faculty of Sciences and Technology of the University of Coimbra.

September 2018



UNIVERSIDADE DE  
COIMBRA





**Host institutions:**



Chemical Process Engineering and Forest Products Research Centre



**CENTER FOR NEUROSCIENCE AND CELL BIOLOGY**

UNIVERSITY OF COIMBRA, PORTUGAL

Center for Neuroscience and Cell Biology

**Colaborations:**

Centre for Physics of the University of Coimbra

Centre for Mechanical Engineering, Materials and Processes of the University of Coimbra



“The future is literally in our hands to mold as we like.  
But we cannot wait until tomorrow. Tomorrow is now.”

Eleanor Roosevelt





## Acknowledgements

I would like to thank multiple people for the contribution to this thesis.

First of all, I would like to thank my supervisors, Dr. Luísa Durães and Dr. Henrique Faneca, for all the guidance and support they always provided and for all the knowledge they transmitted.

I would like to acknowledge Dr. Teresa Vieira for allowing the utilization of TEM and Dr. Rúben Santos for performing this technique.

I would like to thank António Fonseca of LED&MAT for performing the SEM-EDS analysis.

I would also like to acknowledge Dr. José Paixão for allowing the utilization of VSM during this thesis and Dr. Benilde Costa for performing the Mössbauer spectroscopy measurements and for all the help and knowledge provided.

I would like to thank Engineer Isabel Gonçalves for all the advice and help given throughout the course of this work and Dr. Rosemeyre Cordeiro (CNC) for all the assistance during the experimental work.

I would also like to thank my colleagues from the research group for the working environment, as well as all the help they gave me.

To my friends, for all the motivation, support and patience during this part of my life.

To my family, specially my parents, for the unconditional support and without whom the elaboration of this thesis would not be possible.



## Abstract

The aim of the present thesis is to obtain nanoparticles with a superparamagnetic core, made of iron oxide, and a mesoporous shell, made of silica. Combining the magnetic properties and the mesoporosity of these nanoparticles, they can potentially be used for magnetically targeted delivery of antitumour drugs, as well as in other areas of biomedicine.

In this work, three different types of nanoparticles were obtained: IO-OAm/mSiO<sub>2</sub>, IO-APTES/mSiO<sub>2</sub> and IO/SiO<sub>2</sub>/mSiO<sub>2</sub>. In the first two, iron oxide (IO) was obtained by thermal decomposition, being this phase coated with oleylamine (OAm). These two types of nanoparticles differ only in the method to transfer iron oxide into water before the sol-gel reaction to obtain the mesoporous silica shell (mSiO<sub>2</sub>): while for IO-OAm/mSiO<sub>2</sub> a surfactant was used, for IO-APTES/mSiO<sub>2</sub> the OAm molecules were exchanged with (3-aminopropyl)triethoxysilane (APTES). Finally, in the case of IO/SiO<sub>2</sub>/mSiO<sub>2</sub>, iron oxide nanoparticles were obtained by microemulsion and a non-porous silica shell (SiO<sub>2</sub>) was first formed to protect iron oxide from oxidation, before the mesoporous silica shell was obtained (mSiO<sub>2</sub>).

The synthesised nanoparticles were characterized in terms of their physical, chemical and magnetic properties. Additionally, in order to assess their potential to mediate antitumour strategies, they were tested in loading and release of epirubicin, a model anticancer drug.

The presence of iron oxide and silica in the nanoparticles was confirmed by FTIR and EDS. On the other hand, the characterization of the synthesised nanoparticles by TEM and SEM led to the determination of their size. While IO-OAm/mSiO<sub>2</sub> and IO-APTES/mSiO<sub>2</sub> had an average size of 61.3±12.3 nm and 32.9±5.6 nm, the IO/SiO<sub>2</sub>/mSiO<sub>2</sub> were much bigger, having a mean diameter of 371.6±159.4 nm. The TEM images of the synthesised nanoparticles also confirmed the existence of porosity in the three types of nanoparticles.

VSM analysis showed that all the synthesised particles had superparamagnetic behaviour at 300 K. Furthermore, it also showed that the saturation magnetization of the synthesised nanoparticles decreased considerably in comparison with the iron oxide cores produced by thermal decomposition, leading to 4.0 and 1.8 emu.g<sup>-1</sup> for the IO-OAm/mSiO<sub>2</sub> and IO-APTES/mSiO<sub>2</sub> nanoparticles, respectively. This decrease was not as significant in the case of iron oxide obtained by microemulsion and the IO/SiO<sub>2</sub>/mSiO<sub>2</sub> particles, which had a saturation magnetization of 10.2 emu.g<sup>-1</sup>.

The potential application of these nanoparticles as drug carriers led to promising results. The loading content of epirubicin was 3.06±0.22, 3.31±0.87 and 3.37±0.11% for IO-OAm/mSiO<sub>2</sub>, IO-APTES/mSiO<sub>2</sub> and IO/SiO<sub>2</sub>/mSiO<sub>2</sub>, respectively, which is in accordance with

the results found in the literature. The release of the loaded drug from these nanoparticles was studied for 48 hours in a solution of phosphate-buffered saline (PBS) at pH=7.4 and led to the release of  $19.0\pm 2.8$ ,  $23.6\pm 5.6$  and  $31.6\pm 3.3\%$ , respectively. The values obtained for the release were higher than those found in the literature for similar drugs. Therefore, the good results obtained both in loading and release confirm the applicability of these nanoparticles for drug delivery. Additionally, the release profiles were also modelled with the Korsmeyer-Peppas model, leading to  $n$  values smaller than the lower limit established by the model (0.221, 0.288 and 0.187, respectively), which agrees with other  $n$  values found in the literature for nanoparticles.

**Keywords:** mesoporous silica; iron oxide; superparamagnetism; core-shell nanoparticles; drug delivery

## Resumo

O objetivo do presente trabalho é a obtenção de partículas com um *core* superparamagnético, constituído por óxido de ferro, e uma *shell* mesoporosa de sílica. Conjugando as propriedades magnéticas com a mesoporosidade destas nanopartículas, estas apresentam potencial para serem utilizadas para entrega magneticamente controlada de fármacos antitumorais, bem como em outras áreas da biomedicina.

Neste trabalho, três tipos de nanopartículas foram sintetizadas: IO-OAm/mSiO<sub>2</sub>, IO-APTES/mSiO<sub>2</sub> e IO/SiO<sub>2</sub>/mSiO<sub>2</sub>. Nas duas primeiras, o óxido de ferro (IO) foi produzido por decomposição térmica, ficando com uma camada protetora de oleilamina (OAm). Estes dois tipos de nanopartículas diferem apenas no método utilizado para transferir o óxido de ferro para a fase aquosa antes da reação sol-gel em que se obtém a *shell* de sílica mesoporosa (mSiO<sub>2</sub>): no caso de IO-OAm/mSiO<sub>2</sub>, foi utilizado um surfatante, enquanto que, no caso de IO-APTES/mSiO<sub>2</sub>, as moléculas de OAm foram substituídas por aminopropiltriétoxissilano (APTES). Por fim, no caso de IO/SiO<sub>2</sub>/mSiO<sub>2</sub>, as nanopartículas de óxido de ferro foram sintetizadas por microemulsão e uma *shell* de sílica não porosa (SiO<sub>2</sub>) foi obtida para proteger o óxido de ferro de oxidação, antes de se obter a *shell* de sílica mesoporosa (mSiO<sub>2</sub>).

As nanopartículas sintetizadas foram caracterizadas quanto às suas propriedades físicas, químicas e magnéticas. Para além disso, para avaliar o seu potencial para mediar estratégias antitumorais, foram também testadas quanto ao encapsulamento e libertação de epirrubicina, um fármaco modelo para o tratamento de cancro.

A presença de óxido de ferro e sílica foi confirmada por FTIR e EDS. Por outro lado, a caracterização das nanopartículas por TEM e SEM permitiu a determinação do seu tamanho. Enquanto as nanopartículas IO-OAm/mSiO<sub>2</sub> e IO-APTES/mSiO<sub>2</sub> tinham um tamanho médio de 61.3±12.3 nm e 32.9±5.6 nm, as partículas IO/SiO<sub>2</sub>/mSiO<sub>2</sub> tinham um tamanho muito superior, com um diâmetro médio de 371.6±159.4 nm. As imagens obtidas por TEM permitiram também confirmar a existência de porosidade nos três tipos de partículas sintetizadas.

A análise de VSM revelou que todas as partículas sintetizadas tinham comportamento superparamagnético a 300 K. Para além disso, mostrou também que a magnetização de saturação das nanopartículas diminuiu consideravelmente em comparação com os *cores* de óxido de ferro produzidos por decomposição térmica, tendo-se obtido 4.0 e 1.8 emu.g<sup>-1</sup> para as nanopartículas IO-OAm/mSiO<sub>2</sub> and IO-APTES/mSiO<sub>2</sub>, respetivamente. Esta diminuição não foi tão significativa no caso do óxido de ferro produzido por microemulsão e das partículas IO/SiO<sub>2</sub>/mSiO<sub>2</sub>, que tinham uma magnetização de saturação de 10.2 emu.g<sup>-1</sup>.

O estudo do potencial destas nanopartículas para aplicação como veículos de entrega de fármacos levou a resultados promissores. O encapsulamento de epirrubicina, dado pelo *loading content*, foi  $3.06\pm 0.22$ ,  $3.31\pm 0.87$  e  $3.37\pm 0.11\%$ , para IO-OAm/mSiO<sub>2</sub>, IO-APTES/mSiO<sub>2</sub> e IO/SiO<sub>2</sub>/mSiO<sub>2</sub>, respetivamente, o que está de acordo com os valores encontrados na literatura. A libertação do fármaco encapsulado nestas nanopartículas foi estudada durante 48 horas numa solução de tampão fosfato-salino (PBS) a pH=7.4 e levou à libertação de  $19.0\pm 2.8$ ,  $23.6\pm 5.6$  e  $31.6\pm 3.3\%$ , respetivamente. Os valores obtidos para a libertação foram superiores aos encontrados na literatura para fármacos semelhantes. Assim, os bons resultados obtidos, tanto no encapsulamento como na libertação, confirmam a aplicabilidade destas nanopartículas na entrega de fármacos. Adicionalmente, os perfis de libertação foram ainda modelados com o modelo de Korsmeyer-Peppas, levando a valores de  $n$  mais pequenos que o limite inferior estabelecido pelo modelo (0.221, 0.288 e 0.187, respetivamente), o que está de acordo com outros valores de  $n$  encontrados na literatura para nanopartículas.

**Palavras-chave:** sílica mesoporosa; óxido de ferro; superparamagnetismo; nanopartículas *core-shell*; entrega de fármacos.

# Table of Contents

Acknowledgements .....	v
Abstract .....	vii
Resumo .....	ix
List of Figures .....	xiii
List of Tables.....	xvii
Acronyms.....	xix
<b>1. Introduction .....</b>	<b>1</b>
<b>1.1. Motivation and Objectives .....</b>	<b>1</b>
<b>1.2. Thesis outline.....</b>	<b>2</b>
<b>2. Fundamental Concepts .....</b>	<b>3</b>
<b>2.1. Silica Nanoparticles .....</b>	<b>3</b>
<b>2.1.1. Mesoporous Silica Nanoparticles .....</b>	<b>3</b>
<b>2.1.2. Synthesis of MSNs .....</b>	<b>4</b>
<b>2.1.3. Functionalization of MSNs .....</b>	<b>8</b>
<b>2.1.4. Biomedical Applications of MSNs.....</b>	<b>9</b>
<b>2.2. Magnetic Nanoparticles.....</b>	<b>10</b>
<b>2.2.1. Magnetism .....</b>	<b>10</b>
<b>2.2.2. Iron Oxides .....</b>	<b>13</b>
<b>2.2.3. Synthesis of SPIONs .....</b>	<b>14</b>
<b>2.2.4. Biomedical Applications of SPIONs .....</b>	<b>19</b>
<b>2.3. Magnetic Mesoporous Silica Nanoparticles .....</b>	<b>21</b>
<b>3. Materials and Methods .....</b>	<b>27</b>
<b>3.1. Synthesis of IO-OAm/mSiO<sub>2</sub> and IO-APTES/mSiO<sub>2</sub> .....</b>	<b>27</b>
<b>3.1.1. Materials.....</b>	<b>27</b>
<b>3.1.2. Synthesis of iron oxide.....</b>	<b>27</b>
<b>3.1.3. Synthesis of IO-OAm/mSiO<sub>2</sub> .....</b>	<b>28</b>
<b>3.1.4. Synthesis of IO-APTES/mSiO<sub>2</sub>.....</b>	<b>29</b>
<b>3.2. Synthesis of IO/ SiO<sub>2</sub>/mSiO<sub>2</sub> .....</b>	<b>29</b>
<b>3.2.1. Materials.....</b>	<b>29</b>
<b>3.2.2. Synthesis of iron oxide.....</b>	<b>30</b>
<b>3.2.3. Synthesis of the silica shell .....</b>	<b>30</b>
<b>3.3. Supercritical Drying (SCD).....</b>	<b>31</b>
<b>3.4. Drug Loading and Release .....</b>	<b>32</b>
<b>3.4.1. Drug Loading .....</b>	<b>32</b>
<b>3.4.2. Drug Release .....</b>	<b>33</b>

<b>3.5. Characterization Techniques</b> .....	33
<b>3.5.1. Thermogravimetric Analysis (TGA)</b> .....	33
<b>3.5.2. Fourier-Transform Infrared Spectroscopy (FTIR)</b> .....	34
<b>3.5.3. Dynamic Light Scattering (DLS)</b> .....	34
<b>3.5.4. Zeta Potential</b> .....	35
<b>3.5.5. Transmission Electron Microscopy (TEM)</b> .....	36
<b>3.5.6. Scanning Electron Microscopy coupled with Energy Dispersive X-Ray Spectroscopy (SEM-EDS)</b> .....	36
<b>3.5.7. Vibrating Sample Magnetometer (VSM)</b> .....	37
<b>3.5.8. Mössbauer Spectroscopy</b> .....	38
<b>3.5.9. Ultraviolet-Visible (UV-Vis) Spectroscopy</b> .....	40
<b>4. Results and Discussion</b> .....	41
<b>4.1. IO-OAm/mSiO<sub>2</sub></b> .....	41
<b>4.1.1. Synthesis Aspects and Physicochemical Characterization</b> .....	41
<b>4.1.2. Magnetic Characterization</b> .....	50
<b>4.1.3. Drug Loading</b> .....	54
<b>4.1.4. Drug Release</b> .....	56
<b>4.2. IO-APTES/mSiO<sub>2</sub></b> .....	58
<b>4.2.1. Synthesis Aspects and Chemical Characterization</b> .....	58
<b>4.2.2. Magnetic Characterization</b> .....	62
<b>4.2.3. Drug Loading</b> .....	64
<b>4.2.4. Drug Release</b> .....	65
<b>4.3. IO/SiO<sub>2</sub>/mSiO<sub>2</sub></b> .....	66
<b>4.3.1. Synthesis Aspects and Chemical Characterization</b> .....	66
<b>4.3.2. Magnetic Characterization</b> .....	70
<b>4.3.3. Drug Loading</b> .....	72
<b>4.3.4. Drug Release</b> .....	73
<b>4.4. Comparison between the synthesised nanoparticles</b> .....	74
<b>5. Conclusions and Future Works</b> .....	77
<b>References</b> .....	81
<b>APPENDICES</b> .....	87
<b>APPENDIX A – Safety of the used chemical substances</b> .....	89
<b>APPENDIX B – VSM results of the IO-OAm/mSiO<sub>2</sub>*-APD and IO-OAm/mSiO<sub>2</sub>*-SCD nanoparticles</b> .....	97
<b>APPENDIX C – Additional data of the loading experiments</b> .....	99
<b>APPENDIX D – Additional data of the release experiments</b> .....	103



## List of Figures

<b>Figure 1.</b> Different types of MSNs. ....	4
<b>Figure 2.</b> Different stages of the surfactant-templated synthesis of MSN: (a) micelle formation, (b) condensation, (c) alignment, (d) surfactant removal. ....	5
<b>Figure 3.</b> Summary of the different strategies to obtain small-sized MSNs.....	6
<b>Figure 4.</b> Different types of core-shell nanoparticles. ....	7
<b>Figure 5.</b> Illustration of the functionalization of MSNs. ....	8
<b>Figure 6.</b> Illustration of the cargo loading possibilities of MSNs. ....	10
<b>Figure 7.</b> Illustration of the variation of magnetic moment (M) with the external magnetic field (H) in materials with different magnetic behaviour. ....	11
<b>Figure 8.</b> Illustration of the alignment of individual atomic magnetic moments in ferromagnetic, ferrimagnetic and antiferromagnetic materials. ....	12
<b>Figure 9.</b> Intrinsic coercivity as a function of the size of a magnetic particle.....	13
<b>Figure 10.</b> Representation of the magnetization curve for superparamagnetic and ferromagnetic materials. ....	13
<b>Figure 11.</b> Published works on the different methods used to produce SPIONs.....	15
<b>Figure 12.</b> Illustration of the synthesis of SPIONs in a w/o microemulsion. ....	17
<b>Figure 13.</b> Illustration of the synthesis of SPIONs by thermal decomposition. ....	18
<b>Figure 14.</b> Illustration of the ligand exchange process with APTES.....	18
<b>Figure 15.</b> Phase transfer of oleylamine coated SPION into water using CTAB.....	19
<b>Figure 16.</b> Biomedical applications of SPIONs.....	20
<b>Figure 17.</b> Experimental setup for the synthesis of SPIONs by thermal decomposition. ....	28
<b>Figure 18.</b> Experimental setup for the sol-gel reaction.....	29
<b>Figure 19.</b> Experimental setup for the synthesis of SPIONs by microemulsion. ....	30
<b>Figure 20.</b> Supercritical drying equipment. ....	31
<b>Figure 21.</b> Chemical structure of epirubicin. ....	32
<b>Figure 22.</b> Different hyperfine interactions in a <sup>57</sup> Fe nucleus: isomeric shift (left), quadrupole splitting (center) and magnetic hyperfine field (right) ....	39
<b>Figure 23.</b> IO-OAm/mSiO <sub>2</sub> * nanoparticles dried by SCD (left) and APD (right). ....	41
<b>Figure 24.</b> Thermogram of the oleylamine-coated SPIONs. ....	42
<b>Figure 25.</b> FTIR spectra obtained of the SPIONs produced by thermal decomposition and of the final magnetic MSNs dried by APD and SCD. (ν – stretching, δ – bending.) ....	43
<b>Figure 26.</b> TEM image and histogram of the size distribution (n=100) for the IO-OAm/mSiO <sub>2</sub> * - SCD nanoparticles.....	46

<b>Figure 27.</b> TEM image and histogram of the size distribution (n=100) for the IO-OAm/mSiO <sub>2</sub> * - APD nanoparticles. ....	47
<b>Figure 28.</b> Images obtained by TEM for (a) IO-OAm/mSiO <sub>2</sub> *-APD and (b) IO-OAm/mSiO <sub>2</sub> *-SCD particles. ....	47
<b>Figure 29.</b> SEM image of (a) the IO-OAm/mSiO <sub>2</sub> * - APD and (b) the IO-OAm/mSiO <sub>2</sub> * - SCD nanoparticles. ....	48
<b>Figure 30.</b> SEM images with magnetizations of (a) 20.00 kx and (c) 50.00 kx; (b) size distribution histogram and (d) EDS spectrum of the IO-OAm/mSiO <sub>2</sub> -SCD nanoparticles....	49
<b>Figure 31.</b> IO-OAm/mSiO <sub>2</sub> * and IO-OAm/mSiO <sub>2</sub> nanoparticles (a) in the absence and (b) presence of a magnet. ....	50
<b>Figure 32.</b> (a) Magnetization curves of the SPIONs produced by thermal decomposition and (b) detailed view around the origin of the plot. ....	51
<b>Figure 33.</b> (a) Magnetization curves of the IO-OAm/mSiO <sub>2</sub> -SCD nanoparticles and (b) detailed view around the origin of the plot. ....	51
<b>Figure 34.</b> FC and ZFC curves curves obtained with a magnetic field of 100 Oe for (a) the SPIONs synthesised by thermal decomposition and (b) the IO-OAm/mSiO <sub>2</sub> -SCD nanoparticles. ....	52
<b>Figure 35.</b> Mössbauer spectra for the oleylamine coated SPIONs (left) and for the IO-OAm/mSiO <sub>2</sub> - SCD nanoparticles (right). ....	53
<b>Figure 36.</b> Picture of the nanoparticles dispersed in drug solution at the beginning of the loading experiment (left) and picture of the supernatants (right) from the first, second and third centrifugations, in the same order. ....	54
<b>Figure 37.</b> Release profile of epirubicin and correspondent Korsmeyer-Peppas model for the IO-OAm/mSiO <sub>2</sub> nanoparticles. ....	57
<b>Figure 38.</b> Thermogram of the APTES-coated SPIONs. ....	58
<b>Figure 39.</b> FTIR spectra obtained for SPIONs produced by thermal decomposition, for SPIONs after ligand exchange and for the final magnetic MSNs dried by SCD. (ν – stretching, δ – bending.) ....	59
<b>Figure 40.</b> TEM images (a,c) and histogram (b) of the size distribution (n=85) for the IO-APTES/mSiO <sub>2</sub> nanoparticles. ....	61
<b>Figure 41.</b> SEM image and EDS spectrum of the IO-APTES/mSiO <sub>2</sub> nanoparticles. ....	62
<b>Figure 42.</b> IO-APTES/mSiO <sub>2</sub> nanoparticles (a) in the absence and (b) presence of a magnet. ....	63
<b>Figure 43.</b> (a) Magnetization curves of the IO-APTES/mSiO <sub>2</sub> nanoparticles and (b) detailed view around the origin of the plot. ....	63

<b>Figure 44.</b> FC and ZFC curves curves obtained with a magnetic field of 100 Oe for the IO-APTES/mSiO <sub>2</sub> nanoparticles.....	63
<b>Figure 45.</b> Mössbauer spectrum for the IO-APTES/mSiO <sub>2</sub> nanoparticles. ....	64
<b>Figure 46.</b> Release profile of epirubicin and correspondent Korsmeyer-Peppas model for the IO-APTES/mSiO <sub>2</sub> nanoparticles. ....	65
<b>Figure 47.</b> FTIR spectra of the SPIONs obtained by microemulsion and of the final magnetic MSNs dried by SCD. (ν – stretching, δ – bending.).....	66
<b>Figure 48.</b> TEM image and histogram of the size distribution (n=105) for the IO/SiO <sub>2</sub> /mSiO <sub>2</sub> particles.....	68
<b>Figure 49.</b> TEM images of the IO/SiO <sub>2</sub> /mSiO <sub>2</sub> nanoparticles, showing (a) the core nanoparticles and (b) the porosity. ....	69
<b>Figure 50.</b> SEM image and EDS spectrum of the IO/SiO <sub>2</sub> /mSiO <sub>2</sub> particles. ....	70
<b>Figure 51.</b> IO/SiO <sub>2</sub> /mSiO <sub>2</sub> particles (a) in the absence and (b) in the presence of a magnet. .	70
<b>Figure 52.</b> (a) Magnetization curves of the SPIONs produced by microemulsion and (b) detailed view around the origin of the plot.....	71
<b>Figure 53.</b> (a) Magnetization curves of the IO/SiO <sub>2</sub> /mSiO <sub>2</sub> particles and (b) detailed view around the origin of the plot. ....	71
<b>Figure 54.</b> FC and ZFC curves curves obtained with a magnetic field of 100 Oe for (a) the SPIONs obtained by microemulsion and (b) the IO/SiO <sub>2</sub> /mSiO <sub>2</sub> particles.....	72
<b>Figure 55.</b> Release profile of epirubicin and Korsmeyer-Peppas model for the IO/SiO <sub>2</sub> /mSiO <sub>2</sub> nanoparticles.....	73



## List of Tables

<b>Table 1.</b> Organosilanes used in functionalization of MSNs. ....	9
<b>Table 2.</b> Properties of magnetite and maghemite.....	14
<b>Table 3.</b> Published work on magnetic mesoporous silica nanoparticles.....	22
<b>Table 4.</b> DLS results for the different IO-OAm/mSiO <sub>2</sub> samples.....	44
<b>Table 5.</b> Zeta potential of the different IO-OAm/mSiO <sub>2</sub> samples .....	45
<b>Table 6.</b> Loading content and entrapment efficiency for IO-OAm/mSiO <sub>2</sub> nanoparticles. ....	55
<b>Table 7.</b> DLS results for the IO-APTES/mSiO <sub>2</sub> . ....	60
<b>Table 8.</b> Zeta potential of IO-APTES/mSiO <sub>2</sub> . ....	61
<b>Table 9.</b> Loading content and entrapment efficiency for IO-APTES/mSiO <sub>2</sub> nanoparticles. ...	65
<b>Table 10.</b> DLS results for the IO/SiO <sub>2</sub> /mSiO <sub>2</sub> . ....	67
<b>Table 11.</b> Zeta potential of IO/SiO <sub>2</sub> /mSiO <sub>2</sub> . ....	68
<b>Table 12.</b> Loading content and entrapment efficiency for IO/SiO <sub>2</sub> /mSiO <sub>2</sub> particles.....	73
<b>Table 13.</b> Comparison of the different properties and performance of the synthesised particles. .....	74



## Acronyms

APD	Ambient pressure drying
APTES	(3-aminopropyl)triethoxysilane
CTAB	Hexadecyltrimethylammonium bromide
DLS	Dynamic light scattering
DOX	Doxorubicin
EDS	Energy dispersive X-ray spectroscopy
EPI	Epirubicin
FC	Field cooling
Fe(acac) <sub>3</sub>	Iron(III) acetylacetonate
FTIR	Fourier transform infrared spectroscopy
IO	Iron oxide
mSiO <sub>2</sub>	Mesoporous silica
MRI	Magnetic resonance imaging
MSNs	Mesoporous silica nanoparticles
MMSNs	Magnetic mesoporous silica nanoparticles
PBS	Phosphate-buffered saline
OAm	Oleylamine
SCD	Supercritical drying
SEM	Scanning electron microscopy
SPIONs	Superparamagnetic iron oxide nanoparticles
TEM	Transmission electron microscopy
TEOS	Tetraethyl orthosilicate
TGA	Thermogravimetric analysis
UV	Ultraviolet radiation
Vis	Visible radiation
VSM	Vibrating sample magnetometer
ZFC	Zero field cooling





# 1. Introduction

## 1.1. Motivation and Objectives

In the last decades, many advances have been made in the field of nanotechnology. Due to their unique properties, nanomaterials are an interesting approach for different areas, particularly for biomedical applications.

Cancer is one of the main causes of death in the world and, therefore, continuous efforts are being made to overcome the limitations of existing treatments. Traditional chemotherapy is the most common used strategy, but the associated side effects and the development of multidrug resistance limit its efficacy (Alvarez-Berríos *et al.*, 2016). Consequently, there is a need to develop new drug delivery systems with high specificity for cancer cells, low toxicity for normal cells and also controlled and targeted release (Albulet *et al.*, 2017). All these features can be found in nanomaterials, which motivates the research in this area of science. Furthermore, nanoparticles are in the same size range of many biological systems, leading to a good interaction between the two. These materials can also combine therapy with diagnosis and imaging, creating new multipurpose platforms in cancer theranostics (Albulet *et al.*, 2017; Feng *et al.*, 2016).

Mesoporous silica nanoparticles have gained the attention as possible vehicles for drug delivery due to their high loading capacity in the pores, high biocompatibility and easy functionalization (S.-H. Wu *et al.*, 2011). On the other hand, magnetic nanoparticles, particularly iron oxide (SPIONs), are widely studied for their application as contrast agents in imaging, hyperthermia and targeted drug delivery (Laurent *et al.*, 2008), because of their superparamagnetic behaviour. The possibility to conjugate the properties of these two different nanomaterials prompts the development of hybrid magnetic mesoporous silica nanoparticles to serve as multifunctional platforms.

Therefore, the objective of this thesis is to synthesise mesoporous silica nanoparticles with SPIONs incorporated in their core to be posteriorly used as platforms for anticancer treatments. Different methods for the synthesis of iron oxide nanoparticles will be tested along with various strategies for the incorporation in the mesoporous silica shell. Moreover, the synthesised nanoparticles will be tested for the loading and release of an anticancer model drug, in order to evaluate their potential and efficiency in this application.

The nanoparticles will be characterized using different techniques, which include Fourier-Transform Infrared Spectroscopy (FTIR), Thermogravimetric Analysis (TGA), Dynamic Light Scattering (DLS), Zeta Potential, Transmission Electron Microscopy (TEM), Scanning

Synthesis of superparamagnetic mesoporous silica nanoparticles to mediate antitumour strategies

Electron Microscopy coupled with Energy Dispersive X-Ray Spectroscopy (SEM-EDS), Vibrating Sample Magnetometer (VSM) and Mössbauer Spectroscopy.

## **1.2. Thesis outline**

This work is divided in five main chapters, including the present chapter, where the motivations and objectives of this thesis are detailed.

In chapter 2, the fundamental concepts related to mesoporous silica nanoparticles and to magnetism and magnetic nanoparticles are described. In this chapter, the state of the art on superparamagnetic mesoporous silica nanoparticles is also presented.

Chapter 3 has the experimental methods and materials, as well as a description of the used characterization techniques.

In chapter 4, the relevant results of the synthesised nanoparticles are presented, discussed and compared.

Finally, in chapter 5, the conclusions are presented and future works are proposed based on the results.

## 2. Fundamental Concepts

### 2.1. Silica Nanoparticles

Silica (silicon dioxide) is a naturally occurring and very abundant compound on Earth. Due to its availability, it has found many uses in society. Furthermore, silica-based nanoparticles have also gained the attention of the scientific community, particularly in the biomedical field, due to their biosafety (Feng *et al.*, 2016).

The characteristics of these nanoparticles, such as porosity, size and shape, can be controlled during their synthesis. In terms of their porosity, they can be classified as micro-, meso- and macroporous, if their pore diameter is less than 2 nm, between 2 and 50 nm and more than 50 nm, respectively (Pednekar *et al.*, 2017). Within these, mesoporous silica nanoparticles (MSNs) are the ones that have attracted the most interest for biomedical applications (Suri *et al.*, 2013). Thus, the following chapters will be focused on them.

#### 2.1.1. Mesoporous Silica Nanoparticles

The first appearance of mesoporous silica nanoparticles dates back to 1992 when Mobil Co. researchers first obtained them and named them Mobil crystalline materials (MCMs) (Douroumis *et al.*, 2013). Since then, these nanoparticles have been widely studied, particularly after 2001 when they were first used for drug delivery (He *et al.*, 2017).

Owing to their porosity, mesoporous silica nanoparticles have unique features, including high pore volume ( $> 0.9 \text{ cm}^3/\text{g}$ ) and high surface area ( $> 700 \text{ m}^2/\text{g}$ ). They have uniform pores with tuneable size and ordered structure, good biocompatibility and easy functionalization due to the silanol groups on the surface (Douroumis *et al.*, 2013; S.-H. Wu *et al.*, 2013). Furthermore, these materials have good thermal and mechanical stability (Knežević *et al.*, 2013).

MSNs can be classified in different types according to their structure and composition. These include the M41S Family, Organically Modified (ORMOSIL) and Hollow Type (Feng *et al.*, 2016), as shown in Figure 1.

The M41S type includes MCM-41, which was the first kind of mesoporous silica nanoparticles obtained and is the most studied one. MCM-41 has a hexagonal porous structure (Figure 1.a.) but other structure arrangements can be found (Feng *et al.*, 2016). Other type of mesoporous silica nanoparticles is the Santa Barbara Amorphous (SBA-15) that, like MCM-41, has ordered hexagonal pore structure. However, they have some different characteristics, including higher pore and particle sizes (Saroj & Rajput, 2018).

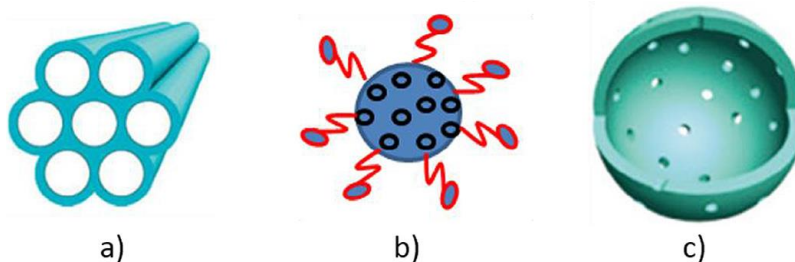


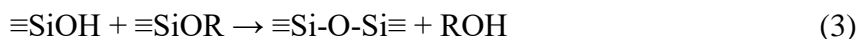
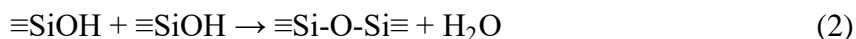
**Figure 1.** Different types of MSNs. Reproduced from Feng *et al.* (2016) with permission from Elsevier.

On the other hand, the ORMOSIL Type (Figure 1.b) are hybrid silica nanoparticles that have organic groups on their surface, which can be both hydrophobic and hydrophilic depending on the silica precursor. Hollow Type MSNs (Figure 1.c) have a large cavity inside, which means they have a higher capacity to load and encapsulate other components (Saroj & Rajput, 2018).

Alongside these types of MSN, nanoparticles of core-shell type are also of interest for the scientific community. They can be synthesised to have a shell of mesoporous silica and incorporate other nanoparticles in the core, for example metal oxides (Yamamoto & Kuroda, 2016). The presence of different components in this type of nanoparticles makes them interesting due to their multifunctionality.

### 2.1.2. Synthesis of MSNs

Since they were first produced, mesoporous silica nanoparticles have been synthesised in a large number of works. The synthesis of MSNs is based in sol-gel chemistry where silica precursors, *e.g.* tetramethyl orthosilicate (TMOS) and tetraethyl orthosilicate (TEOS), go through hydrolysis and condensation reactions (Z. Li *et al.*, 2012), as exemplified in the following equations:



For the building of an ordered structure, these reactions occur in the presence of structure-directing agents, such as surfactants, so that the condensation of silica precursors occurs around the templates formed by these compounds (Z. Li *et al.*, 2012). These agents can be removed later, leaving behind the empty mesopores, as shown in Figure 2. The mechanism for formation

of the mesoporous structure follows a cooperative self-assembly between the precursor and the template molecules (Yamamoto & Kuroda, 2016).

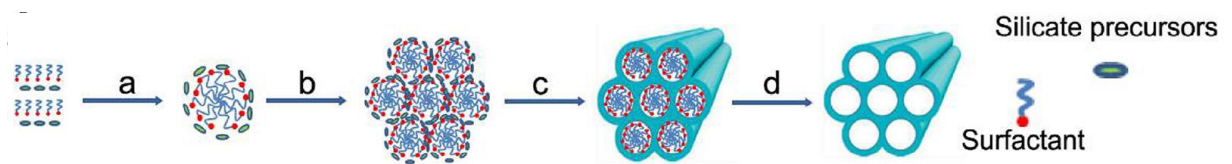


**Figure 2.** Different stages of the surfactant-templated synthesis of MSN: (a) micelle formation, (b) condensation, (c) alignment, (d) surfactant removal. Reproduced from Feng *et al.* (2016) with permission from Elsevier.

Usually, the silica synthesis is catalysed by the presence of a base, but it can also occur in acidic medium, which is the case for obtaining SBA-15. However, an alkaline medium normally leads to particles of nanosize, while the acidic medium commonly produces particles in the micrometre range (Knežević *et al.*, 2013).

The procedure to obtain these nanoparticles mainly consists in modifications of the Stöber process, which is a method first developed in 1968 for the synthesis of silica nanoparticles of monodisperse size (S.-H. Wu *et al.*, 2013). This method is based in the hydrolysis of silica precursors, particularly tetraalkyl orthosilicates, in the presence of water, an alcohol as co-solvent and ammonia as a catalyst. The main modification in the Stöber process is the addition of a surfactant or other templating agent to the mixture in order to obtain the mesoporous structure. Other variations in the procedure include the absence of a co-solvent and the use of different alkaline sources, *e.g.* sodium hydroxide or, more recently, triethanolamine (S.-H. Wu *et al.*, 2011).

The templating agent is very important, both its concentration and type, because it directly influences the structure and size of the mesopores. This compound is typically a cationic surfactant, particularly alkyltrimethylammonium cations, like cetyltrimethylammonium bromide (CTAB), due to their strong interaction with silica precursors (S.-H. Wu *et al.*, 2011). However, other soft or hard templates can be employed, depending on the application and intended pore size and structure. Alternatively, binary surfactant mixtures have been used (*e.g.* CTAB and Pluronic F127), in order to inhibit the growth of the nanoparticles and prevent their aggregation or to obtain nanoparticles with dual mesoporous structures (Suzuki *et al.*, 2004; S.-H. Wu *et al.*, 2013).

On the other hand, the concentration of surfactant affects the structure of the mesopores. Depending on its concentration, the template molecules assemble in different structures, which will create different porous structures, because the condensation of silicate species occurs around these templates (Alothman, 2012). Increasing the surfactant concentration leads to the transition from hexagonal assemblies to cubic and then lamellar assemblies (Alothman, 2012).

Accordingly, increasing the CTAB concentration on the synthesis of MSNs has led to formation of nanoparticles with a cubic porous structure, instead of hexagonally-ordered pores (Luo *et al.*, 2017). Additionally, this concentration also affects the size of the particles, with an increase in the amount of surfactant leading to an increase in particle size, for studies carried out with CTAB above the critical micellar concentration (Nooney *et al.*, 2002).

Along with the type and concentration of the templating agent, other parameters influence the size and structure of the MSNs, especially the ratio between this agent and the silica precursor. Other factors that are also important in the synthesis include the ratios between silica precursor, water and base, the type of silica precursor, the presence of other substances and temperature.

Two aspects that are important to control in MSNs are both their particle size and pore size. To obtain mesoporous silica nanoparticles of small size, there are three different approaches that can be followed: growth quench, confinement, and separation of nucleation and growth (S.-H. Wu *et al.*, 2011), as described in Figure 3.

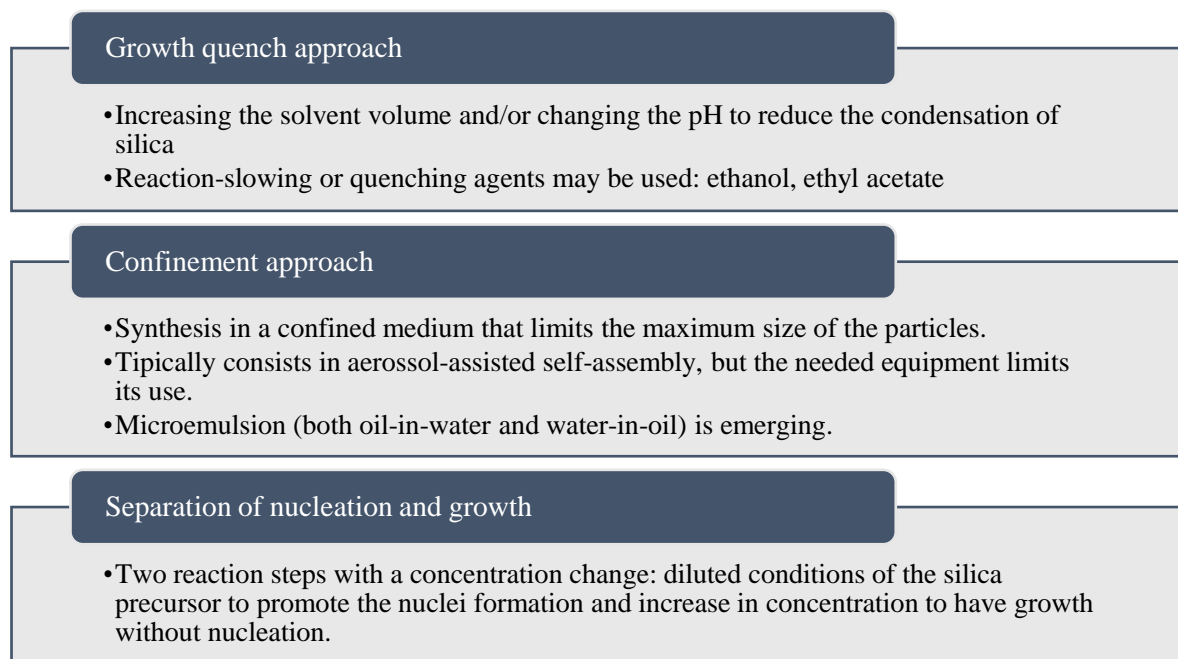


**Figure 3.** Summary of the different strategies to obtain small-sized MSNs. Adapted from S.-H. Wu *et al.* (2011) and Pednekar *et al.* (2017).

On the other hand, in terms of porosity, there are some strategies to increase the pore size. When using alkyltrimethylammonium surfactants, the alkyl length can be varied in order to tune the pore size. However, this only allows limited increase of the pore size. Alternatively, the use of swelling agents such as trimethylbenzene (TMB) can lead to the formation of larger pores during synthesis (S.-H. Wu *et al.*, 2013). The use of block copolymers as hard templates

instead of surfactants has also been shown to lead to larger pores (Sayari, 2003; S.-H. Wu *et al.*, 2013). Another common strategy consists in doing a hydrothermal step after the synthesis, which also induces porosity in the nanoparticles (Sayari, 2003).

### Core-Shell Nanoparticles

The methods for the synthesis of core-shell nanoparticles, which are of interest for the present thesis, are very similar to those presented for mesoporous silica nanoparticles without a different core. The main difference is indeed the presence of the core nanoparticles in the reaction media. These nanoparticles are stabilized in solution by the surfactant molecules (most commonly, CTAB), which work both as stabilizer of the core nanoparticles and template for the mesoporous structure (S.-H. Wu *et al.*, 2011).

The formation of the mesoporous shell usually follows a seed-growth mechanism, where the core nanoparticles act as nuclei for the growth of mesoporous silica (Yamamoto & Kuroda, 2016). The condensation of the silica precursors takes place around these seeds, creating nanoparticles of core-shell type. Depending on the quantity of the different substances, nanoparticles of heterogeneous composition might be obtained instead of nanoparticles with one single core (W. Wu *et al.*, 2016). The different types of nanoparticles that might be formed are illustrated in Figure 4.

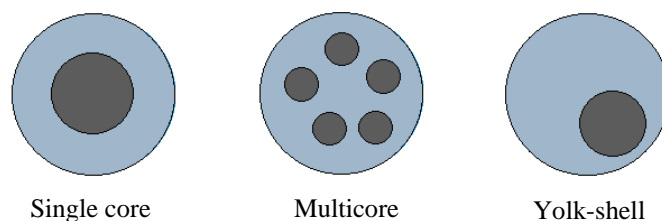


**Figure 4.** Different types of core-shell nanoparticles.

### Surfactant Removal

In order to obtain the mesoporous structure, the surfactant or other templating agent needs to be removed. This step can be done either by calcination or by solvent extraction and ion exchange.

Calcination is a process that involves the use of high temperature, normally around 500-600°C in the case of MSNs, in order to decompose the surfactant molecules. However, these temperatures also promote the condensation of silanol groups, which can lead to irreversible aggregation of the nanoparticles (Asefa & Tao, 2012). Furthermore, in the case of core-shell nanoparticles, the temperature can also have a negative impact in the core compounds, such as undesirable oxidation.

In the case of extraction, MSNs are mixed with the extracting solution, which is normally an acidic solution. The extracting solutions interact with the surfactant and promote its removal from the mesoporous silica structure. Even though this method does not have the problem of additional aggregation, it is possible that residual template molecules remain in the nanoparticles.

There is not an agreement on which is the best method to remove the template molecules, with some claiming that it is solvent extraction (S.-H. Wu *et al.*, 2013), while others defend calcination (Asefa & Tao, 2012).

### 2.1.3. Functionalization of MSNs

Mesoporous silica nanoparticles are a versatile platform because they are easily functionalized with many different groups, due to the silanol groups present on their surface. They can be modified both in their outer surface and in the inner surface of their pores. These modifications can occur by two methods: co-condensation and post-synthetic grafting. In co-condensation, organosilanes with the intended functional groups are added during the synthesis, while in post-synthetic grafting the functional groups are added to the surface after the synthesis (Z. Li *et al.*, 2012). Furthermore, these two methods can be combined to obtain MSNs with different functionalities. Post-synthetic grafting can also be used prior to surfactant removal in order to have selective functionalization, as shown in Figure 5.

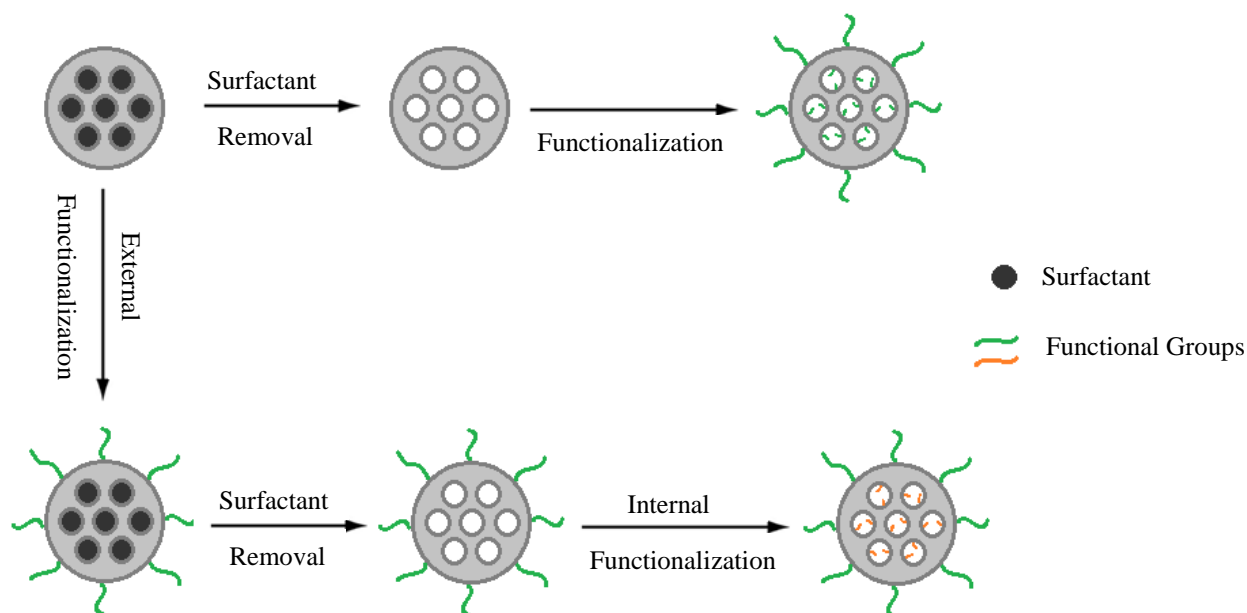


**Figure 5.** Illustration of the functionalization of MSNs. Adapted from S.-H. Wu *et al.*, 2011.

Organosilanes are very effective for the surface functionalization of silica materials because they have hydrolysable groups that react with the hydroxyl groups on the surface of



silica nanoparticles, while the organofunctional group remains unreacted. (Rahman & Padavettan, 2012). Furthermore, there is a large variety of organic groups that can be present in organosilanes, making them versatile compounds. MSNs are frequently functionalised with amine, thiol, carboxylic acid, phenyl or other groups (Douroumis *et al.*, 2013; Liberman *et al.*, 2014). Some of the most commonly used organosilanes are presented in Table 1.

**Table 1.** Organosilanes used in functionalization of MSNs. Compiled from Rahman & Padavettan (2012) and Douroumis *et al.* (2013).

Name	Chemical formula
3-Aminopropyltriethoxysilane	$(\text{C}_2\text{H}_5\text{O})_3\text{Si}-\text{CH}_2\text{CH}_2\text{CH}_2\text{NH}_2$
3-Mercaptopropyltriethoxysilane	$(\text{C}_2\text{H}_5\text{O})_3\text{Si}-\text{CH}_2\text{CH}_2\text{CH}_2\text{SH}$
Phenylethyltrimethoxysilane	$(\text{CH}_3\text{O})_3\text{Si}-\text{CH}_2\text{CH}_2\text{C}_6\text{H}_5$
Vinyltriethoxysilane	$(\text{C}_2\text{H}_5\text{O})_3\text{Si}-\text{CH}=\text{CH}_2$

The functionalization of MSNs can be done with different intents, which include controlling the surface charge of the nanoparticles, making the nanoparticles hydrophobic and allowing the chemical attachment of other molecules to the surface (*e.g.* drugs, proteins and pH-responsive polymers) (Mai & Meng, 2013; S.-H. Wu *et al.*, 2011).

#### 2.1.4. Biomedical Applications of MSNs

In the past years, the interest in MSNs for applications in the field of biomedicine has grown. However, they have the potential to be used in other areas, such as catalysis, optics, adsorption and photochemistry (S.-H. Wu *et al.*, 2011; Yamamoto & Kuroda, 2016).

For biomedical applications, it is important to evaluate the biosafety and cytotoxicity of the nanoparticles. MSNs have shown good biocompatibility and low toxicity, which sets them apart from other inorganic materials. Furthermore, their high pore volume makes them attractive for the encapsulation of substances for subsequent release. These aspects, along with the high surface area and easy functionalization, make them interesting for applications in the diagnosis and treatment of different diseases, such as cancer, diabetes and infectious diseases (Mai & Meng, 2013).

MSNs are particularly attractive for cancer therapy, because, depending on their functionalization, they can encapsulate not only hydrophilic but also hydrophobic anticancer drugs in their pores. Tumour cells have enhanced permeability and retention (EPR) of nanoparticles, allowing particles in the 30-200 nm size range to enter and accumulate in them (Shi *et al.*, 2016). Therefore, the possibility to control the size of MSNs during their synthesis to fall in this range is another reason for their use in anticancer strategies. Moreover, they can

Synthesis of superparamagnetic mesoporous silica nanoparticles to mediate antitumour strategies

be used to develop drug delivery systems with controlled and targeted release, which are more efficient and cause less damage to non-cancerous cells.

MSNs can also incorporate different substances simultaneously (Colilla *et al.*, 2013) as illustrated in Figure 6, such as contrast agents for imaging, multiple drugs, DNA and stimuli-responsive substances, creating versatile platforms (Suri *et al.*, 2013). As a result, they can be attractive in cancer theranostics, which is an emerging field that encompasses both the diagnosis and the therapy of this disease (Z. Li *et al.*, 2012; Mai & Meng, 2013; S.-H. Wu *et al.*, 2013).

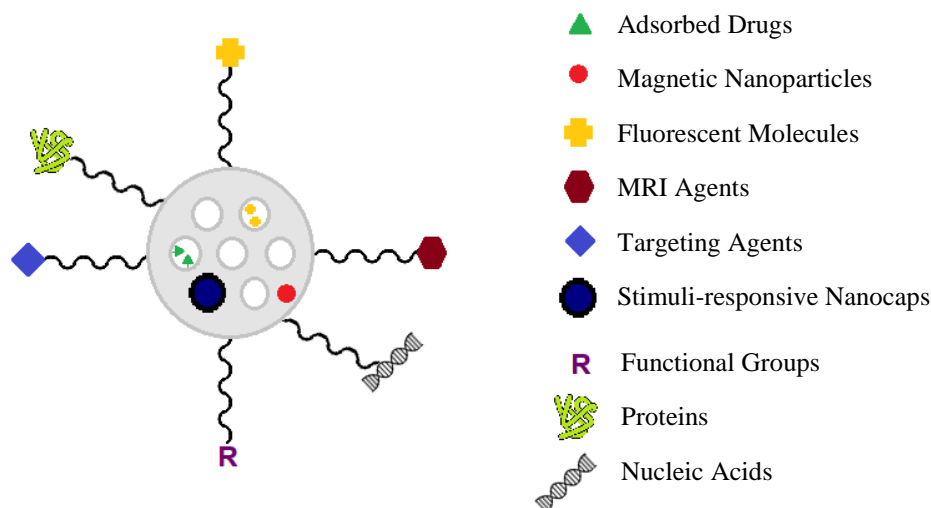


**Figure 6.** Illustration of the cargo loading possibilities of MSNs. Adapted from Colilla *et al.*, 2013.

## 2.2. Magnetic Nanoparticles

Magnetic nanoparticles have also caught the attention of the scientific community and a lot of research regarding these materials has been done in the past 20 years (Angelakeris, 2017). These nanoparticles have been the object of study especially in the environmental and biomedical fields (Mohammed *et al.*, 2017) because of their unique properties and distinctive behaviour, which are related to their magnetic nature.

### 2.2.1. Magnetism

The first mentions of magnetism date back to nearly three thousand years ago in Ancient Greece. However, progress in this field only came much later with William Gilbert writing the first scientific book about Earth's magnetic field in 1600 (Campbell, 2001). After that, much has been done to better understand magnetism, particularly in the last two centuries (Blundell, 2001; Buschow & de Boer, 2003a).

Nowadays, magnetism and magnetic materials are of great value for many different technological fields and have found their way to multiple everyday-life objects (Buschow & de Boer, 2003a).

Magnetism is intrinsic to matter, and materials can be classified according to their response to an external magnetic field, which is given in terms of their magnetic susceptibility (Buschow & de Boer, 2003a; Sodipo & Aziz, 2016). Materials can, therefore, be considered diamagnetic, paramagnetic, ferromagnetic, antiferromagnetic and ferrimagnetic (Figure 7. a-c).

Diamagnetic materials, in the presence of an external magnetic field, exhibit a weak induced magnetic moment that is contrary to the magnetic field that caused it. In paramagnetic materials, the induced magnetic moment is stronger and generally along the same direction as the external magnetic field. In the absence of this magnetic field, diamagnetic materials do not have magnetic moment, while the atoms of paramagnetic materials have magnetic moments that are orientated in random directions (Blundell, 2001).

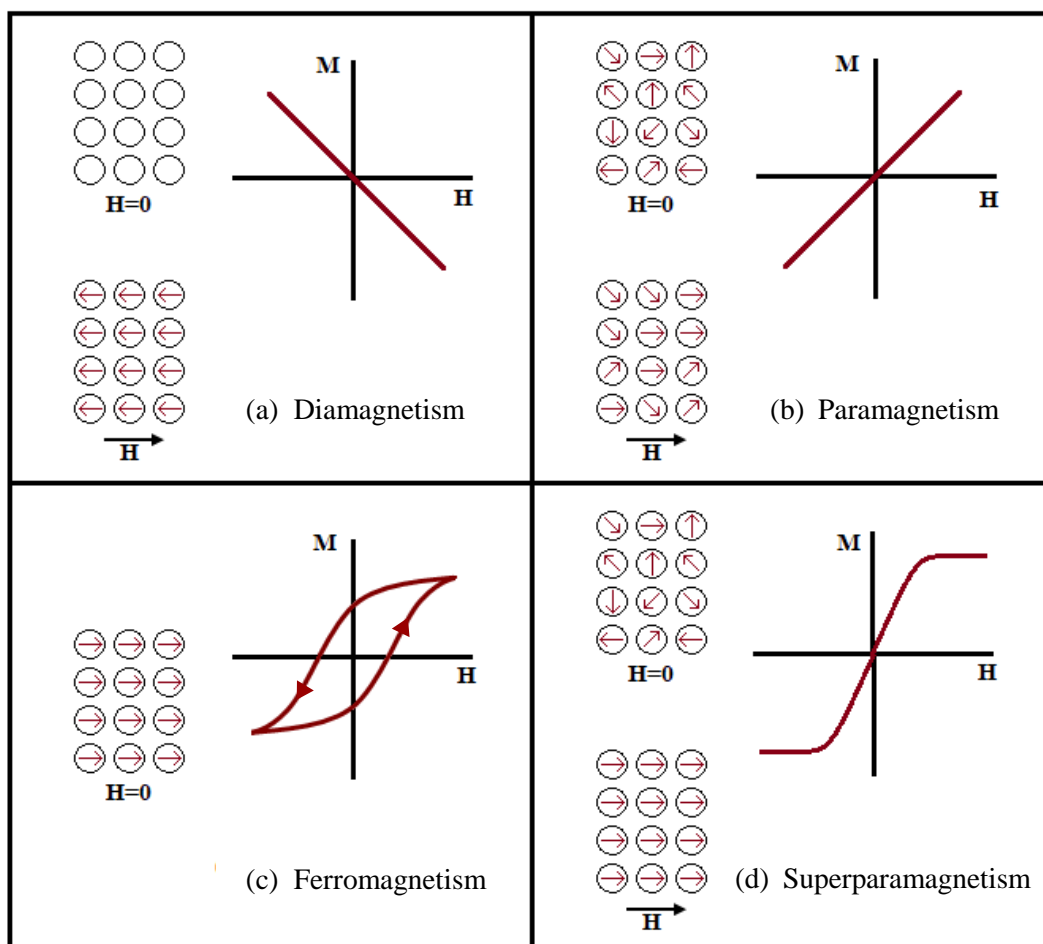


**Figure 7.** Illustration of the variation of magnetic moment ( $M$ ) with the external magnetic field ( $H$ ) in materials with different magnetic behaviour. Adapted from Sodipo & Aziz (2016).

Ferromagnetic materials present spontaneous magnetization even without the presence of an external magnetic field, with all magnetic moments of the same domain aligned in one direction (Blundell, 2001). Antiferromagnetism and ferrimagnetism can be considered subclasses of ferromagnetism (Sodipo & Aziz, 2016; Teja & Koh, 2009) and they occur when two sublattices are present and their magnetic moments point in opposite directions (Figure 8). In ferrimagnetic materials, the magnetic moments are not equivalent and, consequently, the net magnetic moment is not zero. In antiferromagnetic materials, the two magnetic moments are identical but of opposite signs and, thus, they cancel each other (Blundell, 2001).

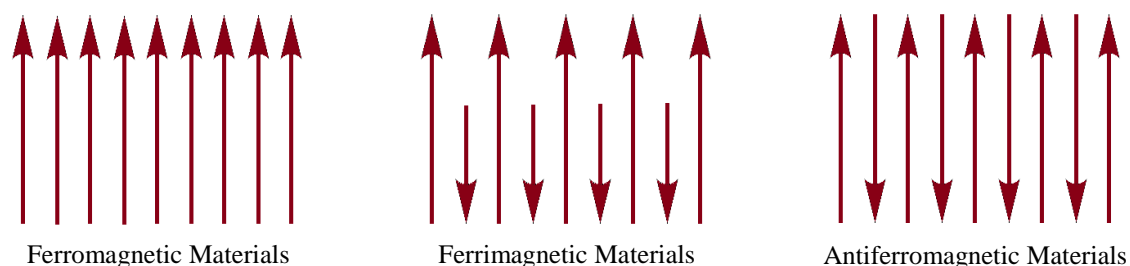


**Figure 8.** Illustration of the alignment of individual atomic magnetic moments in ferromagnetic, ferrimagnetic and antiferromagnetic materials.

### Superparamagnetism

Superparamagnetism is a phenomenon that can be found in nanoparticles of ferromagnetic or ferrimagnetic materials and its occurrence is directly related to their size (Sodipo & Aziz, 2016) - Figure 7.d.

Bulk ferromagnets and ferrimagnets present multiple magnetic domains and, therefore, have a complex magnetization structure. However, with a decrease in size, the surface energy between domain walls becomes progressively more relevant and, below a certain critical size ( $D_s$ ), it becomes more favourable, in terms of energy, to have particles with a single domain. Another property that is affected by the size decrease is coercivity, which is the required magnetic field to compensate the remaining magnetization on a material after the removal of an external magnetic field. The intrinsic coercivity of a material,  $H_C$ , reaches a maximum value at  $D_s$ , as seen in Figure 9. This critical size is usually in the nanometre range and thus, nanoparticles below this size generally present one single magnetic domain (Angelakeris, 2017; Blundell, 2001; O' Connor *et al.*, 2001).

Below  $D_s$ , as shown in Figure 9, coercivity decreases until it reaches zero at another critical diameter ( $D_p$ ), which corresponds to the transition to superparamagnetic behaviour.

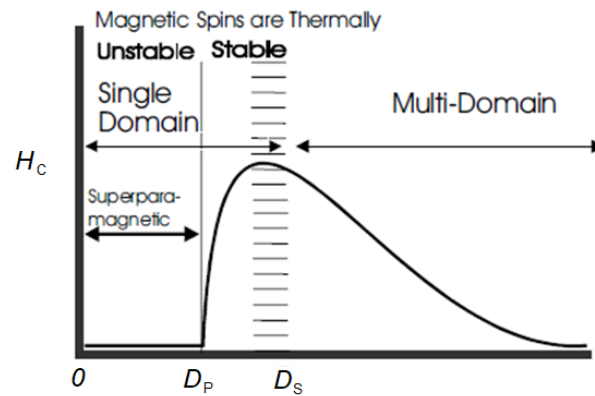


**Figure 9.** Intrinsic coercivity as a function of the size of a magnetic particle (O' Connor *et al.*, 2001).

Superparamagnetic nanoparticles can therefore be found at sizes below  $D_p$  and have zero coercivity and no remanence (Figure 10) or, in other words, they have zero magnetization when an external magnetic field is not present. Superparamagnetic materials are also characterized by their thermally unstable magnetic moments and their superparamagnetic behaviour ceases to occur below a temperature called blocking temperature ( $T_b$ ) (Angelakeris, 2017; O' Connor *et al.*, 2001).

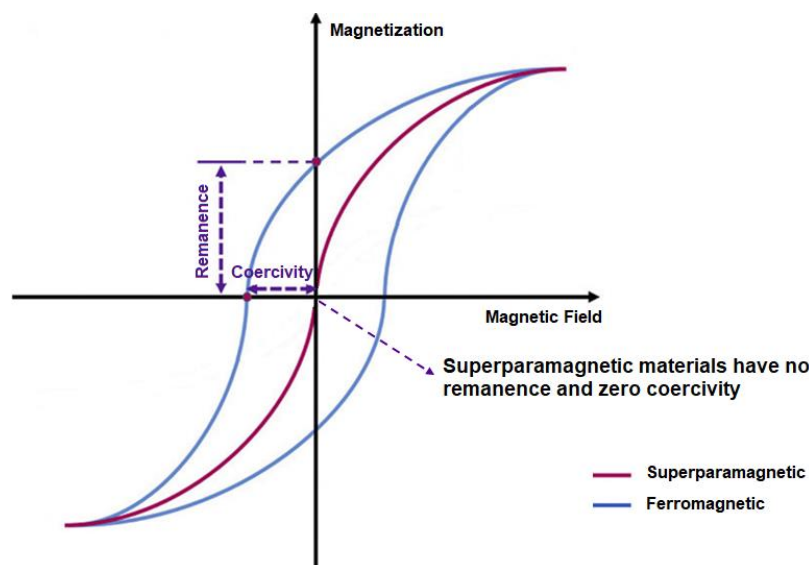


**Figure 10.** Representation of the magnetization curve for superparamagnetic and ferromagnetic materials. Adapted from Mohammed *et al.*, 2016.

### 2.2.2. Iron Oxides

Iron oxides can be found in nature in different forms, which include oxides, hydroxides and oxyhydroxides. In these compounds, Fe is linked by O and/or OH bridges, differing in the composition, crystal structure and iron valence (Cornell & Schwertmann, 2003).

These compounds are very important in several fields of application, ranging from mineralogy and chemical industry to nanomedicine and biology. Superparamagnetic iron oxide

nanoparticles (SPIONs) have particularly emerged in the last two fields. SPIONs consist mainly of two iron oxides: magnetite ( $\text{Fe}_3\text{O}_4$ ) and maghemite ( $\gamma\text{-Fe}_2\text{O}_3$ ). They are both ferrimagnetic below their Curie temperature ( $T_C$ ) (Cornell & Schwertmann, 2003; Teja & Koh, 2009; Tombácz *et al.*, 2015). Some of their properties are presented in Table 2.

**Table 2.** Properties of magnetite and maghemite. Compiled from Teja & Koh. (2009) and Cornell & Schwertmann (2006).

Iron Oxide	Crystallographic system	Structural type	Lattice parameter /nm	Density /g.cm <sup>-3</sup>	$T_C$ /K	Saturation magnetization at 300 K /emu.g <sup>-1</sup>
Magnetite	Cubic	Inverse spinel	0.8396	5.18	850	92-100
Maghemite	Cubic or tetrahedral	Defect spinel	0.8347	4.87	820 - 986	60-80

Magnetite is a black mineral and is also the most magnetic of all transition metal oxides. It contains both Fe(II) and Fe(III) in its composition, which differentiates it from maghemite. Magnetite has an inverse spinel structure, where Fe(III) ions are both in octahedral and tetrahedral sites, while Fe(II) ions are only in octahedral positions. Because iron can be in these two different sites, two sublattices are formed with antiparallel magnetic moments. Since these have different magnitude, magnetite exhibits ferrimagnetic behaviour below its Curie temperature, as stated above (Cornell & Schwertmann, 2003; Teja & Koh, 2009). Furthermore, magnetite nanoparticles smaller than 6 nm have superparamagnetic behaviour at room temperature, although this magnetic behaviour is strongly dependent on the synthesis method (Teja & Koh, 2009).

Maghemite is a red-brownish mineral, with a similar spinel structure to that of magnetite with two antiparallel sublattices. It is composed in majority by trivalent iron. Due to the absence of bivalent iron, cation vacancies are found in the octahedral sites. As a result of these defects, the sublattices have different magnitude and thus, maghemite also has a ferrimagnetic behaviour below its Curie temperature and nanoparticles smaller than 10 nm exhibit superparamagnetic behaviour (Cornell & Schwertmann, 2003; Teja & Koh, 2009). Maghemite can be obtained by the oxidation of magnetite and it can also form continuous solid solutions with this iron oxide (Teja & Koh, 2009).

### 2.2.3. Synthesis of SPIONs

Considerable research has been done regarding the synthesis of SPIONs. They can be obtained by physical, chemical and biological methods, though the chemical synthetic routes are the most common (Mahmoudi *et al.*, 2011), as shown in Figure 11.

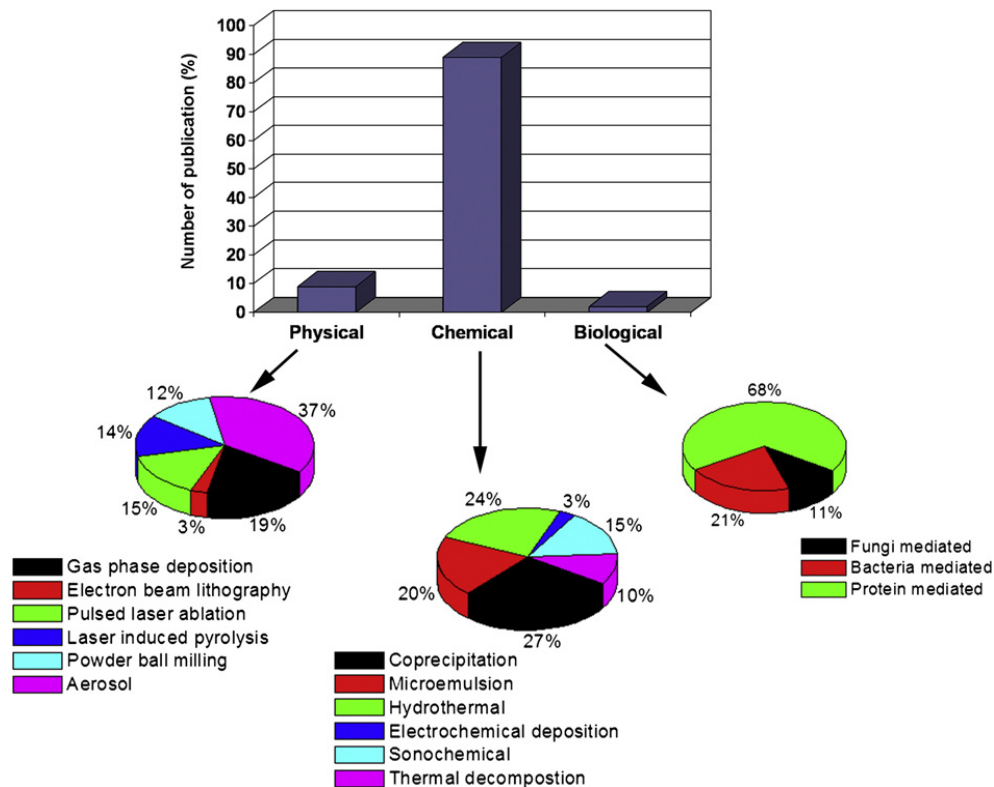


**Figure 11.** Published works on the different methods used to produce SPIONs.

Reproduced from Mahmoudi *et al.* (2011) with permission from Elsevier.

As it can be seen in Figure 11, the three most cited methods for the synthesis of SPIONs are coprecipitation, the hydrothermal process and microemulsion.

Coprecipitation is one of the most employed strategies for the production of SPIONs because of its simplicity and high yield. This synthesis occurs at room conditions and allows a good size control of the nanoparticles by adjusting the reaction parameters. However, agglomeration of the nanoparticles is a common problem, as well as a wide size distribution and poor crystallinity (Sodipo & Aziz, 2016; Stanicki *et al.*, 2015). The hydrothermal method involves the use of high pressure and temperature to reach supercritical water conditions. It produces SPIONs with high crystallinity and monodisperse size and it leads to very good size control and less agglomeration, but also a lower yield than coprecipitation (Sodipo & Aziz, 2016). Finally, microemulsion is another alternative for the production of SPIONs. It leads to the formation of nanoparticles with monodisperse size and low agglomeration. However, even though it occurs at room conditions, the synthesis is complicated, the yield is low and high amounts of organic chemicals are needed (Qiao *et al.*, 2009; Roca *et al.*, 2009; Sodipo & Aziz, 2016).

Besides these three methods, thermal decomposition, though less cited, is also another well-known method for the synthesis of SPIONs. The synthesis is complex, employing high

temperature and needing an inert atmosphere. However, it allows very good size control and leads to monodisperse and highly crystalline particles with very low agglomeration. Moreover, the obtained nanoparticles are highly stable, due to the organic protective coating formed during the synthesis. The main disadvantage is that the produced SPIONs are hydrophobic (Roca *et al.*, 2009; Sodipo & Aziz, 2016; Stanicki *et al.*, 2015).

Considering the knowledge of the research group where this work is inserted, the two methods employed during this thesis were thermal decomposition and microemulsion. Thus, they are described next in more detail.

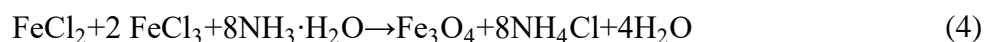
### **Microemulsion**

Microemulsions are thermodynamically stable systems of two immiscible liquids. These systems consist of nanosized droplets that are stabilized by a surfactant (Singh *et al.*, 2014). The droplets provide a confined media where chemical synthesis may occur, leading to the formation of uniform sized nanoparticles.

Water-in-oil (w/o) microemulsions are generally used for the synthesis of SPIONs. In these systems, small water droplets are dispersed in oil, creating constrained environments for the nucleation and controlled growth of SPIONs. These confined environments limit the size of nanoparticles and control their size distribution. Moreover, the size of the nanoparticles can be tuned by changing the water/surfactant ratio and the concentrations of the iron oxide precursors and surfactant (Sodipo & Aziz, 2016; Teja & Koh, 2009).

In order to obtain SPIONs, coprecipitation occurs inside the water droplets. Therefore, two different microemulsions are needed: one with the iron oxide precursors and another with the precipitating agent. These two microemulsions are then mixed together and the reactants are interchanged between the water droplets, consequently initiating the formation of the nanoparticles and their subsequent growth (Sodipo & Aziz, 2016), as represented in Figure 12.

The coprecipitation reaction is expressed by equation 4, using ammonium hydroxide as the precipitating agent:



Different types of surfactants can be used, both ionic and non-ionic, with cetyltrimethylammonium bromide (CTAB) and sodium dodecylsulfate (SDS) often being reported in the literature (Laurent *et al.*, 2008). The type of surfactant has influence in the properties of the nanoparticles, along with their concentration and the reaction temperature (Laurent *et al.*, 2008).



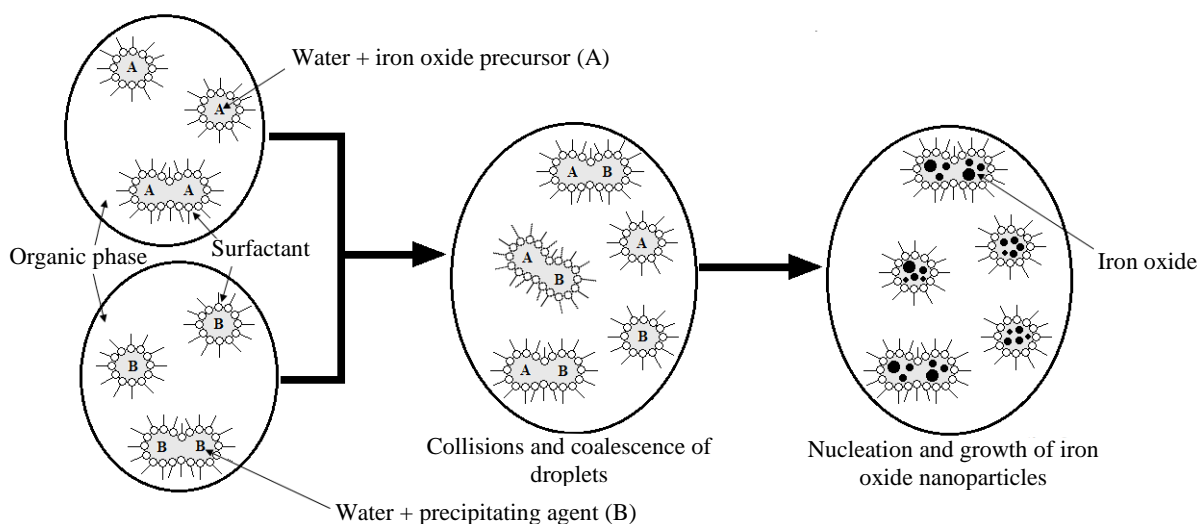


**Figure 12.** Illustration of the synthesis of SPIONs in a w/o microemulsion. Adapted from Sodipo & Aziz (2016) and Teja & Koh (2009).

The disadvantages of this method, along with the already mentioned, include the residual surfactant molecules remaining in the nanoparticles and the difficulty of scale-up (Teja & Koh, 2009).

### Thermal Decomposition

SPIONs can be obtained by thermal decomposition of organometallic precursors at high temperatures, in the presence of organic solvents with high boiling points and surfactants. This synthesis occurs in an inert atmosphere (Sodipo & Aziz, 2016).

The organometallic precursors include iron(III) acetylacetonate ( $\text{Fe}(\text{acac})_3$ ), iron carboxylate, iron carbonyls, *etc.* Iron(III) acetylacetonate is particularly important because it leads to the formation of magnetite nanoparticles of very good controlled size (Roca *et al.*, 2009; Teja & Koh, 2009). In terms of surfactants, oleic acid, oleylamine and stearic acid are typically used and organic solvents include phenyl ether and benzyl ether (Roca *et al.*, 2009; Sodipo & Aziz, 2016).

The type of iron precursor and surfactant, along with their ratio and reaction time, influence the nanoparticles size and their magnetic properties. Furthermore, temperature also plays a very important role in the size and morphology of the obtained SPIONs and, in order to obtain highly crystalline nanoparticles, temperatures up to 300°C are needed (Sodipo & Aziz, 2016).

The synthesis of SPIONs by thermal decomposition involves two different stages: nucleation and growth, according to the La Mer mechanism (Tombácz *et al.*, 2015). In order to

obtain nanoparticles of uniform size, the separation of these two stages is very important. This process is illustrated in Figure 13.

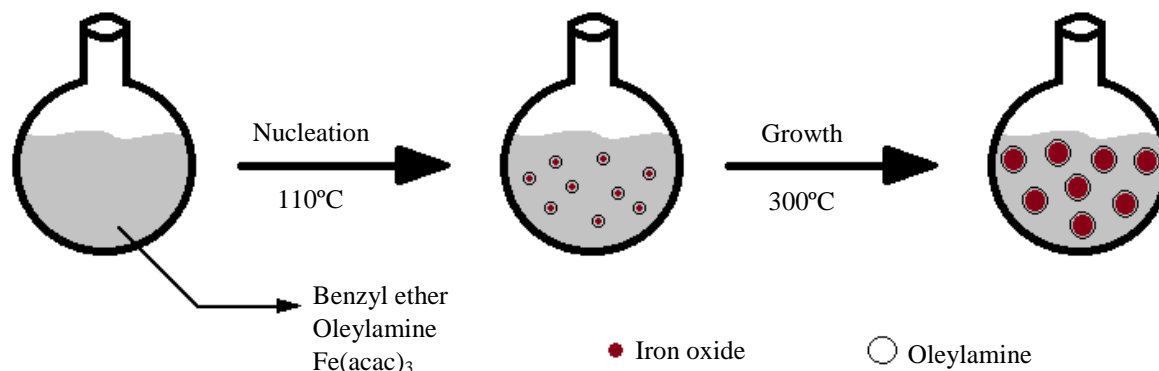


**Figure 13.** Illustration of the synthesis of SPIONs by thermal decomposition.

During the current thesis, iron(III) acetylacetonate, benzyl ether and oleylamine were used for the synthesis of SPIONs by thermal decomposition, taking advantage of the knowledge of the research group and the good results obtained previously. Furthermore, two temperature thresholds were established: 75 minutes at 110°C for the nucleation stage and 45 minutes at 300°C for the nanoparticles' growth (Campos-Gonçalves *et al.*, 2017; Gaspar *et al.*, 2017; Gonçalves, 2016; Santos, 2015).

SPIONs obtained by thermal decomposition are hydrophobic due to the surfactant coating (in this case, oleylamine). Therefore, different strategies exist in order to disperse these nanoparticles in water, including ligand exchange and coating with amphiphilic species, such as polymers or alkylammonium salts (Roca *et al.*, 2009; Stanicki *et al.*, 2015).

During the present work, the hydrophobic SPIONs must be transferred into water and the two strategies referred above were considered to accomplish this: ligand exchange with 3-aminopropyltriethoxysilane (APTES) and coating with CTAB.

Ligand exchange is commonly used to modify the surface chemistry of nanoparticles because it does not modify the core particle size and shape (Davis *et al.*, 2016). In this case, the coated SPIONs are mixed with APTES in an organic solvent and left under stirring (Davis *et al.*, 2016; De Palma *et al.*, 2007; Larsen *et al.*, 2012). Consequently, the oleylamine coating on SPIONs is removed and exchanged with APTES (Figure 14).

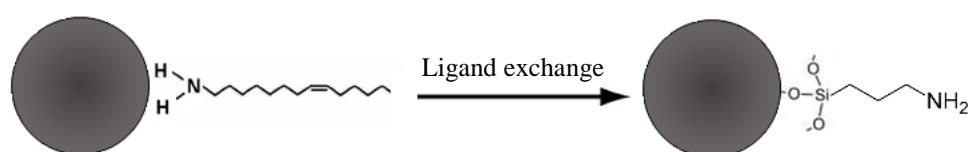


**Figure 14.** Illustration of the ligand exchange process with APTES. Adapted from Larsen *et al.* (2012) and De Palma *et al.* (2007).

In this way, the resulting iron oxide nanoparticles become hydrophilic and can be dispersed in water.

The second procedure involves the dispersion of SPIONs in an organic solvent of easy evaporation, namely chloroform, and the mixture with a CTAB aqueous solution. The hydrophobic chains of oleylamine and CTAB interact with each other and the hydrophilic part of CTAB allows the dispersion of the hydrophobic SPIONs in water (Ye *et al.*, 2012), as exemplified in Figure 15.

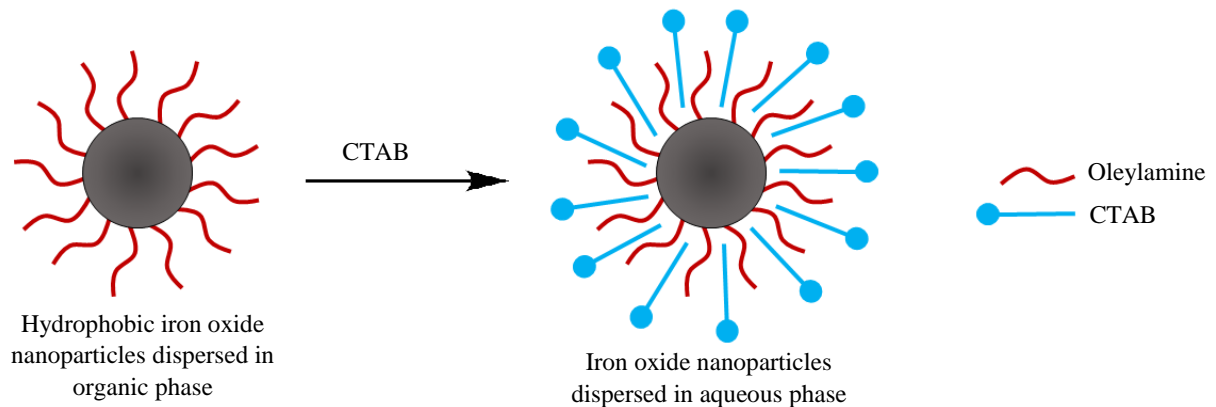


**Figure 15.** Phase transfer of oleylamine coated SPION into water using CTAB. Adapted from W. Wu *et al.* (2016).

#### 2.2.4. Biomedical Applications of SPIONs

SPIONs have great potential for different biomedical applications, with a lot of research being done in this field (Roca *et al.*, 2009). They can also be used for other applications, such as magnetic seals, magnetic recording media, ferrofluids, catalysts, environmental applications and magnetic separation (Mohammed *et al.*, 2017; Teja & Koh, 2009).

For biomedical applications, it is important that the SPIONs have uniform physicochemical characteristics and are stable in water at physiological salinity and pH (Mahmoudi *et al.*, 2011; Roca *et al.*, 2009). SPIONs have proven to be interesting for these applications due to their biocompatibility, biodegradability and superparamagnetic behaviour. This last aspect is important because the lack of residual magnetization after the presence of an external magnetic field helps to avoid agglomeration *in vivo* (Mohammed *et al.*, 2017).

These nanoparticles can be used as contrast agents for magnetic resonance imaging for the detection and diagnosis of different diseases (Qiao *et al.*, 2009). Nowadays, five different contrast agents based on SPIONs have already been clinically approved and can be found on the market.

SPIONs can also be used for targeted and controlled release of drugs. By applying an external magnetic field, SPIONs can be separated from other components and directed to specific sites. However, there can be some limitations in magnetic targeting due to the distance

Synthesis of superparamagnetic mesoporous silica nanoparticles to mediate antitumour strategies

between the magnet and the specific sites (Mahmoudi *et al.*, 2011; Mohammed *et al.*, 2017). SPIONs can also be engineered with different sites for the interaction with targeted cells, in order to avoid cytotoxic effects in non-diseased cells. Therefore, they are interesting for cancer therapy, where the severe side effects of chemotherapy drugs are one of the main issues.

Another important use of SPIONs in cancer therapy is in hyperthermia treatments. These nanoparticles, when in the presence of a high-frequency alternating magnetic field, release heat that induces the rise in temperature of cells up to 45°C. This increase in temperature causes reversible damage to normal cells but the damage is irreversible in tumorous cells (Mohammed *et al.*, 2017).

SPIONs can also find use as nanocarriers for radioimmunotherapy and in the delivery, not only of many different drugs, but also of DNA, peptides and antibodies. Furthermore, they can be incorporated in other nanomaterials, creating multifunctional platforms for different applications in nanomedicine (Malekigorji *et al.*, 2014).

Their biomedical applications are summarized in Figure 16.

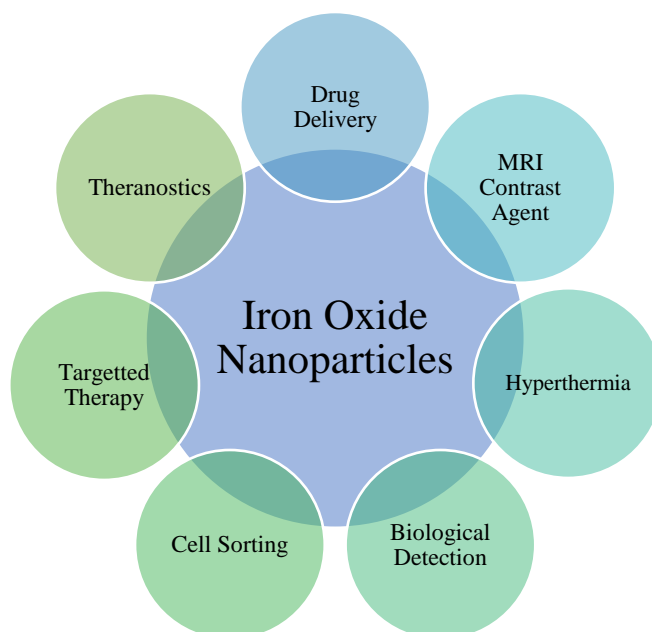


**Figure 16.** Biomedical applications of SPIONs. Adapted from Malekigorji *et al.* (2014).

### 2.3. Magnetic Mesoporous Silica Nanoparticles

Hybrid nanomaterials are interesting because of the possibility to conjugate the properties of the different components. Among these, magnetic mesoporous silica nanoparticles (MMSNs) are particularly interesting because they retain the appealing characteristics that have already been mentioned, of both magnetic and mesoporous nanoparticles.

Nanoparticles with iron oxide and mesoporous silica in their composition have been widely studied in the last years. These nanoparticles have shown potential in different fields of application, such as catalysis, environmental remediation, optics and especially in the field of nanomedicine, both in drug delivery systems and magnetic resonance imaging (MRI) (Chang *et al.*, 2010; Mueller *et al.*, 2015; Suteewong *et al.*, 2010). In particular, magnetic mesoporous silica nanoparticles are being tested to be used in cancer treatment. This interest arises from the fact that, together with the porosity, biocompatibility and stability of MSNs, they allow the imaging of cancerous tissue both in diagnosis and during treatment and the magnetic guiding of drugs to specific locations. Furthermore, by applying an external magnetic field, it can also be possible to have controlled drug release (Avedian *et al.*, 2018; Knežević *et al.*, 2012; Yoshikawa *et al.*, 2017).

There are a few different strategies to incorporate iron oxide and mesoporous silica in the same nanomaterial. The probably most common is the synthesis of core-shell nanoparticles with iron oxide as core nanoparticles and mesoporous silica as shell. This method implies the previous synthesis of iron oxide and then the condensation of silica precursors around it, in the presence of a surfactant, as was described in section 2.1.2. (Avedian *et al.*, 2018; Chang *et al.*, 2010; Luong *et al.*, 2016; Ronhovde *et al.*, 2017; Sodipo & Aziz, 2016; Suteewong *et al.*, 2010; Ye *et al.*, 2012). The main disadvantage is that the presence of the silica shell leads to a significant decrease in the saturation magnetization of the final nanoparticles (Sodipo & Aziz, 2016). Another strategy involves the previous synthesis of MSNs and, then, their pores are impregnated with iron precursors to obtain iron oxide inside the pores (Omar *et al.*, 2017; Sodipo & Aziz, 2016; Zapotoczny *et al.*, 2015). The disadvantage of this method is that, because iron oxide is already in the pores of mesoporous silica, their loading capacity for other components is much lower. Finally, the last approach consists of iron oxide nanoparticles capping the pores of the mesoporous silica nanoparticles (Chen *et al.*, 2016; Gan *et al.*, 2011).

For the present thesis, it is of interest to obtain iron oxide/mesoporous silica core-shell nanoparticles and, thus, different methods to synthesise these nanomaterials were studied. Table 3 presents relevant scientific publications that are in accordance with the intended objectives of this work.

**Table 3.** Published work on magnetic mesoporous silica nanoparticles.

Ref.	Chemical System <sup>(a)</sup>		Synthesis Method		Particle Characteristics	Drug Release Results <sup>(a)</sup>
	Iron Oxide	Silica	Iron Oxide	Silica		
Luong <i>et al.</i> , 2016	<ul style="list-style-type: none"> <li>– Precursor: iron-oleate complex</li> <li>– Stabilizer: oleic acid</li> <li>– Solvent: 1-octadecene</li> </ul>	<ul style="list-style-type: none"> <li>– Precursor: TEOS</li> <li>– Catalyst: NaOH</li> <li>– Surfactant: CTAB</li> </ul>	Thermal decomposition: <ul style="list-style-type: none"> <li>– To prepare the precursor, reaction of sodium oleate and iron(III) chloride hexahydrate at 70°C for 4 h.</li> <li>– Main reaction at 320°C for 30 min.</li> </ul>	Sol-gel: <ul style="list-style-type: none"> <li>– SPIONs transferred into water using chloroform and an aqueous solution of CTAB (0.11 M).</li> <li>– Addition of NaOH (2 M), water, TEOS and ethyl acetate.</li> <li>– Reaction at 70°C for 3 h under reflux.</li> <li>– Solution of HCl (37%) to remove the surfactant.</li> </ul>	<ul style="list-style-type: none"> <li>– Particle size: 50 nm.</li> <li>– Saturation magnetization: 3.86 emu.g<sup>-1</sup>.</li> </ul>	Loading of Rhodamine B fluorescent dye: <ul style="list-style-type: none"> <li>– Release of 40% after 4 days at 50°C under a 6 kA/m external magnetic field.</li> </ul>
Ye <i>et al.</i> , 2012	<ul style="list-style-type: none"> <li>– Precursor: iron-oleate complex</li> <li>– Stabilizer: oleic acid</li> <li>– Solvent: dioctyl ether</li> </ul>	<ul style="list-style-type: none"> <li>– Precursor: TEOS</li> <li>– Catalyst: NaOH</li> <li>– Surfactant: CTAB</li> </ul>	Thermal decomposition: <ul style="list-style-type: none"> <li>– Precursor prepared as in the last entry.</li> <li>– Reaction at 297°C.</li> </ul>	Sol-gel: <ul style="list-style-type: none"> <li>– SPIONs transferred into water using chloroform and an aqueous solution of CTAB.</li> <li>– Addition of NaOH, water, TEOS and ethyl acetate.</li> <li>– Reaction at 70°C for 2 h.</li> <li>– Solution of NH<sub>4</sub>NO<sub>3</sub> (10 mg/mL) in ethanol to remove the surfactant.</li> </ul>	<ul style="list-style-type: none"> <li>– Particle size: 25 – 95 nm.</li> <li>– Pore size: 1.4 – 2.7 nm.</li> <li>– Saturation magnetization: 48.3 emu.g<sup>-1</sup> Fe</li> </ul>	Not tested.
Suteewong <i>et al.</i> , 2010	<ul style="list-style-type: none"> <li>– Precursor: FeO(OH)</li> <li>– Stabilizer: oleic acid</li> <li>– Solvent: 1-octadecene</li> </ul>	<ul style="list-style-type: none"> <li>– Precursor: TEOS</li> <li>– Catalyst: NH<sub>4</sub>OH</li> <li>– Surfactant: CTAB</li> </ul>	Thermal decomposition: <ul style="list-style-type: none"> <li>– Reaction at 320°C for 1 h.</li> </ul>	Sol-gel: <ul style="list-style-type: none"> <li>– SPIONs transferred into water using chloroform and an aqueous solution of CTAB (54.8 mM).</li> <li>– Addition of NH<sub>4</sub>OH, TEOS, ethyl acetate and water and reaction at room temperature.</li> <li>– Solution of acetic acid in ethanol to remove the surfactant.</li> </ul>	<ul style="list-style-type: none"> <li>– Particle size: 62±10 nm.</li> <li>– Pore size: 2.74 nm.</li> </ul>	Not tested.

<sup>(a)</sup> CTAB - hexadecyltrimethylammonium bromide, TEOS – tetraethyl orthosilicate.

**Table 3.** Published work on magnetic mesoporous silica nanoparticles. (cont.)

Ref.	Chemical System <sup>(a)</sup>		Synthesis Method		Particle Characteristics	Drug Release Results <sup>(a)</sup>
	Iron Oxide	Silica	Iron Oxide	Silica		
Liong <i>et al.</i> , 2008	<ul style="list-style-type: none"> <li>– Precursor: iron-oleate complex</li> <li>– Stabilizer: oleic acid</li> <li>– Solvent: octadecene</li> </ul>	<ul style="list-style-type: none"> <li>– Precursor: TEOS, APTES, THSPMP</li> <li>– Catalyst: NaOH</li> <li>– Surfactant: CTAB</li> </ul>	Thermal decomposition: <ul style="list-style-type: none"> <li>– Reaction of sodium oleate and iron(III) chloride hexahydrate under reflux for 4 h.</li> <li>– Iron-oleate dissolved in oleic acid and octadecene and placed under vacuum for 30 min at 80°C.</li> <li>– Reaction at 320°C for 1 h.</li> </ul>	Sol-gel: <ul style="list-style-type: none"> <li>– SPIONs transferred into water using chloroform and an aqueous solution of CTAB.</li> <li>– Addition of NaOH (2 M) and water, heating to 80°C and addition of a solution of FITC–APTES in ethanol and TEOS.</li> <li>– Reaction with THSPMP for 2 h.</li> <li>– Solution of NH<sub>4</sub>NO<sub>3</sub> in ethanol to remove the surfactant.</li> </ul>	<ul style="list-style-type: none"> <li>– Particle size: 100 – 200 nm.</li> <li>– Pore size: ~3 nm.</li> </ul>	Loading of CPT and TXL: <ul style="list-style-type: none"> <li>– Release of 29% of CPT in DMSO after 15 min.</li> <li>– Release of 26% of TXL in methanol after 15 min.</li> </ul>
Avedian <i>et al.</i> , 2018	<ul style="list-style-type: none"> <li>– Precursors: iron(III) chloride and iron(II) chloride</li> <li>– Precipitating agent: NH<sub>4</sub>OH</li> </ul>	<ul style="list-style-type: none"> <li>– Precursor: TEOS</li> <li>– Catalyst: NH<sub>4</sub>OH</li> <li>– Surfactant: CTAB</li> </ul>	Coprecipitation: <ul style="list-style-type: none"> <li>– Dissolution of iron chlorides in water at 80°C under N<sub>2</sub>.</li> <li>– Addition of NH<sub>4</sub>OH and reaction for 30 min.</li> </ul>	Sol-gel: <ul style="list-style-type: none"> <li>– SPIONs dispersed in water and ethanol, addition of TEOS and reaction at 40°C under N<sub>2</sub>.</li> <li>– Nanoparticles added to an aqueous solution of CTAB and NH<sub>4</sub>OH, heating to 60°C, addition of TEOS and reaction under reflux for 2 h.</li> <li>– Stirring at room temperature for 3 days.</li> <li>– Calcination at 600°C for 5 h.</li> <li>– Functionalization with folic acid–conjugated PEI.</li> </ul>	<ul style="list-style-type: none"> <li>– Particle size: 200.8 nm (DLS).</li> <li>– Pore size: 2.4 nm.</li> <li>– Saturation magnetization: 24 emu.g<sup>-1</sup></li> </ul>	Loading of erlotinib: <ul style="list-style-type: none"> <li>– 65% of the loaded drug released after 100 h at pH=7.</li> </ul>
Ronhovde <i>et al.</i> , 2017	<ul style="list-style-type: none"> <li>– Precursors: iron(III) chloride and iron(II) chloride</li> <li>– Precipitating agent: NH<sub>4</sub>OH</li> </ul>	<ul style="list-style-type: none"> <li>– Precursor: TEOS</li> <li>– Catalyst: NH<sub>4</sub>OH</li> <li>– Surfactant: CTAC</li> </ul>	One-pot procedure: <ul style="list-style-type: none"> <li>– Dissolution of iron chlorides in water at 80°C under N<sub>2</sub>.</li> <li>– Addition of NH<sub>4</sub>OH and reaction for 30 min.</li> <li>– Addition of a CTAC aqueous solution and stirring for 15 min.</li> <li>– Heating to 60°C, addition of TEOS and reaction at 60°C.</li> <li>– Overnight evaporative drying and calcination in air at 600°C for 6 h.</li> </ul>		<ul style="list-style-type: none"> <li>– Particle size: 70.8 nm.</li> <li>– Pore size: 3.14 nm.</li> </ul>	Loading of DOX: <ul style="list-style-type: none"> <li>– Loading content: 15 mg. g<sup>-1</sup>.</li> <li>– Release of ~3.5% of DOX at pH=7.4 and 37°C after 300 min.</li> </ul>

<sup>(a)</sup> APTES – (3-aminopropyl)triethoxysilane, CPT – camptothecin, CTAC - hexadecyltrimethylammonium chloride, DMSO – dimethyl sulfoxide, DOX – doxorubicin, FITC – fluorescein isothiocyanate, PEI – polyethyleneimine, TEOS – tetraethyl orthosilicate, THSPMP – 3-(trihydroxysilyl)propyl methylphosphonate, TXL – paclitaxel.

**Table 3.** Published work on magnetic mesoporous silica nanoparticles. (cont.)

Ref.	Chemical System <sup>(a)</sup>		Synthesis Method		Particle Characteristics	Drug Release Results <sup>(a)</sup>
	Iron Oxide	Silica	Iron Oxide	Silica		
Tao & Zhu, 2014	<ul style="list-style-type: none"> <li>– Precursors: iron(III) chloride and iron(II) chloride</li> <li>– Precipitating agent: NaOH</li> </ul>	<ul style="list-style-type: none"> <li>– Precursor: TEOS</li> <li>– Catalyst: TEA</li> <li>– Surfactant: CTAT</li> </ul>	Coprecipitation: <ul style="list-style-type: none"> <li>– Dissolution of iron chlorides in water for 30 min by ultrasonication.</li> <li>– Addition of HCl.</li> <li>– Dropwise addition of a NaOH solution and stirring at room temperature for 1 h.</li> <li>– Nanoparticles vacuum dried at 60°C for 24 h.</li> </ul>	Sol-gel: <ul style="list-style-type: none"> <li>– SPIONs dispersed in water by ultrasonication for 30 min.</li> <li>– Addition of CTAT and TEA.</li> <li>– Heating to 80°C, stirring, rapid addition of TEOS and reaction for 2 h.</li> <li>– Nanoparticles vacuum dried at 60°C for 24 h.</li> <li>– Calcination at 540°C for 7 h.</li> </ul>	<ul style="list-style-type: none"> <li>– Particle size: ~150 nm.</li> <li>– Pore size: 3.2 – 12.5 nm.</li> <li>– Saturation magnetization: 4.2 – 8.1 emu.g<sup>-1</sup> at 298 K.</li> </ul>	Loading and release of DOX: <ul style="list-style-type: none"> <li>– Loading content: 43.9 – 45.4 µg.mg<sup>-1</sup></li> <li>– Release of 7 – 8% and 55 – 65% of the loaded DOX at pH=7.4 and pH=5.0, respectively, after 23 h.</li> </ul>

<sup>(a)</sup> 9AA – 9-aminoacridine, CPT – camptothecin, CTAB - hexadecyltrimethylammonium bromide, CTAT – hexadecyltrimethylammonium p-toluene-sulfonate, DOX – doxorubicin, Ph-TMS – Phenylethyltrimethoxysilane, TEA – triethanolamine, TEOS – tetraethyl orthosilicate.



**Table 3.** Published work on magnetic mesoporous silica nanoparticles. (cont.)

Ref.	Chemical System <sup>(a)</sup>		Synthesis Method		Particle Characteristics	Drug Release Results <sup>(a)</sup>
	Iron Oxide	Silica	Iron Oxide	Silica		
Chang <i>et al.</i> , 2010	<ul style="list-style-type: none"> <li>– Precursor: iron(III) chloride and iron(II) sulfate</li> <li>– Precipitating agent: NH<sub>4</sub>OH</li> <li>– Stabilizer: oleic acid</li> </ul>	<ul style="list-style-type: none"> <li>– Precursor: TEOS</li> <li>– Catalyst: NH<sub>4</sub>OH</li> <li>– Surfactant: CTAB</li> </ul>	<ul style="list-style-type: none"> <li>– Coprecipitation: Dissolution of iron precursors in water.</li> <li>– Heating to 90°C and addition of the NH<sub>4</sub>OH and oleic acid.</li> <li>– Reaction for 3 h.</li> <li>– Nanoparticles dispersed in octane.</li> </ul>	<ul style="list-style-type: none"> <li>– Sol-gel: SPIONs transferred into water using chloroform and an aqueous solution of CTAB.</li> <li>– Addition of water at 40°C and stirring for 2 h</li> <li>– Addition of NH<sub>4</sub>OH, TEOS and ethyl acetate and reaction at 40°C for 6 h.</li> <li>– Solution of NH<sub>4</sub>NO<sub>3</sub> in ethanol to remove the surfactant.</li> <li>– Functionalization of the nanoparticles with –COOH, –NH<sub>2</sub>, –PO<sub>3</sub><sup>–</sup> and –Phenyl.</li> </ul>	<ul style="list-style-type: none"> <li>– Particle size: 210 – 219 nm (DLS); 130 ± 20 nm (TEM).</li> <li>– Pore size: 2.6 – 3.1 nm.</li> <li>– Saturation magnetization: ~2 emu.g<sup>-1</sup></li> </ul>	<ul style="list-style-type: none"> <li>– Loading of DOX: <ul style="list-style-type: none"> <li>– Loading content: MMSN – 5.8%; MMSN-COOH – 10.5%; MMSN-PO<sub>3</sub><sup>–</sup> – 31.0%.</li> <li>– At pH=7.4 release of 23% and 45.2% of the loaded DOX in MMSN-COOH and MMSN- PO<sub>3</sub><sup>–</sup>, respectively, after 120 h.</li> <li>– At pH=5.5 release of 47.6% and 54.9% of the loaded DOX in MMSN-COOH and MMSN- PO<sub>3</sub><sup>–</sup>, respectively, after 120 h.</li> </ul> </li> </ul>

<sup>(a)</sup> α-Fe<sub>2</sub>O<sub>3</sub> – hematite, γ-Fe<sub>2</sub>O<sub>3</sub> – maghemite, CTAB - hexadecyltrimethylammonium bromide, DOX – doxorubicin, MMSN – magnetic mesoporous silica nanoparticle, TEOS – tetraethyl orthosilicate, THSPMP – 3-(trihydroxysilyl)propyl methylphosphonate, TXL – paclitaxel.

By analysing Table 3 it is noticeable that considerable different works have been done regarding this type of hybrid nanomaterials in the last years. The analysis of these publications, in terms of synthetic routes and final characteristics of the nanoparticles, was very important to establish the procedures to follow during the present work.

As it can be seen in Table 3, iron oxide for the intended purposes is mainly obtained by thermal decomposition and coprecipitation. Regarding the mesoporous silica formation, the methods have small differences, mainly in temperature, reaction time and alkaline source. TEOS is the silica precursor of choice, although Knežević *et al.* (2012) and Liong *et al.* (2008) used other silica precursors along with TEOS to functionalize the nanoparticles by co-condensation. On the other hand, CTAB is the most often used surfactant.

In the publications where iron oxide was obtained by thermal decomposition, small magnetic mesoporous silica nanoparticles were synthesised (50 and 62 nm by Luong *et al.* (2016) and Suteewong *et al.* (2010), respectively). It is important to take into account that oleic acid is the surfactant used in these publications, while in the present work oleylamine will be used. Furthermore, in Luong *et al.* (2016), Suteewong *et al.* (2010) and Ye *et al.* (2012), phase transfer of SPION into water was done using chloroform and CTAB. No publications were found where ligand exchange with APTES was performed as an intermediate step before the formation of the mesoporous silica shell, which will also be tested during this thesis.

On the other hand, for iron oxide prepared by microemulsion, attention was given to the publications where coprecipitation was employed. It is evident that the work developed by Avedian *et al.* (2018) is slightly different from the other scientific articles presented in Table 3, because SPIONs were first coated with non-porous silica and the mesoporous silica shell was only formed after. This strategy was found interesting because the non-porous silica might act as a protecting coat to avoid the oxidation of iron oxide, which leads to a considerably higher saturation magnetization ( $24 \text{ emu.g}^{-1}$ ) than in the other works, such as Tao & Zhu (2014).

In Table 3, it is also evident that magnetic mesoporous silica nanoparticles have been widely studied for applications in drug delivery. They have been used for the loading and release of different anticancer drugs, both hydrophobic, such as camptothecin, and hydrophilic, particularly doxorubicin hydrochloride (DOX) (Ronhovde *et al.*, 2017; Tao & Zhu, 2014). Doxorubicin is a commonly used model drug for loading and release studies in MSNs because it is very potent and efficient against cancerous tissue. However, its applicability is limited because of its severe cardiotoxic effects (T. Li *et al.*, 2016; Ronhovde *et al.*, 2017). Therefore, the preparation of MMSNs loaded with drugs, such as doxorubicin, is very promising because these multifunctional drug delivery systems can be used for targeted release and thus, reduce the serious effects associated with the traditional method of administration of the drug.

### 3. Materials and Methods

#### 3.1. Synthesis of IO-OAm/mSiO<sub>2</sub> and IO-APTES/mSiO<sub>2</sub>

To synthesise these nanomaterials, iron oxide (IO) is firstly obtained by thermal decomposition. Then, the iron oxide nanoparticles coated with oleylamine (IO-OAm) or with APTES (IO-APTES) are transferred into water and finally the mesoporous silica shell (mSiO<sub>2</sub>) is obtained.

##### 3.1.1. Materials

Iron(III) acetylacetonate (Fe(acac)<sub>3</sub>, Fe(C<sub>5</sub>H<sub>7</sub>O<sub>2</sub>)<sub>3</sub>, 97%), oleylamine (C<sub>18</sub>H<sub>35</sub>NH<sub>2</sub>, >70%), benzyl ether ((C<sub>6</sub>H<sub>5</sub>CH<sub>2</sub>)<sub>2</sub>O, 98%), ethanol (C<sub>2</sub>H<sub>6</sub>O, 99.99%), hexane (CH<sub>3</sub>(CH<sub>2</sub>)<sub>4</sub>CH<sub>3</sub>, 99%), hexadecyltrimethylammonium bromide (CTAB, CH<sub>3</sub>(CH<sub>2</sub>)<sub>15</sub>N(Br)(CH<sub>3</sub>)<sub>3</sub>, >99%), chloroform (CHCl<sub>3</sub>, >99.80%), sodium hydroxide (NaOH, >97%), tetraethyl orthosilicate (TEOS, Si(OC<sub>2</sub>H<sub>5</sub>)<sub>4</sub>, 98%), ethyl acetate (CH<sub>3</sub>COOC<sub>2</sub>H<sub>5</sub>, >99.5%), ammonium nitrate (NH<sub>4</sub>NO<sub>3</sub>, >99%), (3-aminopropyl) triethoxysilane (APTES, H<sub>2</sub>N(CH<sub>2</sub>)<sub>3</sub>Si(OC<sub>2</sub>H<sub>5</sub>)<sub>3</sub>, 98%), acetic acid (CH<sub>3</sub>COOH, 99.83%) and toluene (C<sub>6</sub>H<sub>5</sub>CH<sub>3</sub>, >99%) were used as purchased without additional purification. Ultrapure water was used throughout the synthesis.

These substances were handled in agreement with the safety information presented in Appendix A.

##### 3.1.2. Synthesis of iron oxide

The method used for the synthesis of iron oxide by thermal decomposition was according to the knowledge of our research group (Campos-Gonçalves *et al.*, 2017; Gaspar *et al.*, 2017; Gonçalves, 2016).

Briefly, 2 mmol of Fe(acac)<sub>3</sub>, 1 mL of oleylamine and 4 mL of benzyl ether are added to a three-neck round-bottom flask. The reaction is kept under magnetic agitation in nitrogen atmosphere and under reflux, as shown in Figure 17.

The reaction occurs in two steps: 110°C for 75 minutes and then 300°C for 45 minutes. After the second stage of temperature, the mixture is cooled to room temperature and the particles are centrifuged (5000 rpm, 10 minutes) and washed with ethanol three times. Finally, the nanoparticles are dispersed in hexane.



**Figure 17.** Experimental setup for the synthesis of SPIONs by thermal decomposition.

### 3.1.3. Synthesis of IO-OAm/mSiO<sub>2</sub>

This synthesis follows the procedure published by Luong *et al.* (2016). 12 mg of oleylamine-coated SPIONs are oven dried and dispersed in 0.5 mL of chloroform. An aqueous solution of CTAB (0.11 M) is prepared by dissolving CTAB in 5 mL of water at 35°C and is then added to the SPION dispersed in chloroform. The solution is vigorously stirred for two hours and, afterwards, it is heated to 61.5°C for 20 minutes to evaporate the chloroform and promote the interaction between the hydrophobic chains of oleylamine and CTAB.

The previous mixture is transferred to a 100 mL three-neck round-bottom flask, and 0.3 mL of a NaOH aqueous solution (2 M) and 45 mL of water are added. The mixture is heated in an oil bath to 70°C before 0.5 mL of TEOS and 3 mL of ethyl acetate are added. The reaction occurs for 3 hours under magnetic stirring and reflux conditions, as shown in Figure 18.

After cooling to room temperature, the nanoparticles are centrifuged and washed three times with ethanol.

To remove the surfactant, the procedure was according to Liong *et al.* (2008). A solution of ethanolic NH<sub>4</sub>NO<sub>3</sub> is prepared by dissolving 160 mg of NH<sub>4</sub>NO<sub>3</sub> in 30 mL of ethanol and the nanoparticles, dispersed in 30 mL of ethanol, are added to this solution and left under magnetic stirring for 30 minutes at 60°C.

Afterwards, the nanoparticles are again centrifuged and washed three times with ethanol. To dry the nanoparticles, two different methods were performed: drying in an oven at 60°C and supercritical drying.



**Figure 18.** Experimental setup for the sol-gel reaction.

#### 3.1.4. Synthesis of IO-APTES/mSiO<sub>2</sub>

The ligand exchange procedure with APTES is according to Davis *et al.* (2016) with slight modifications.

Briefly, 25 mg of oleylamine-coated SPIONs are dispersed in 3 mL of toluene. Acetic acid (5  $\mu$ L), water (0.25 mL) and APTES (0.75 mL) are then added and the mixture is left under magnetic stirring for 3 days at room temperature.

The nanoparticles are then washed once with ethanol and three times with hexane before being redispersed and washed two times in water.

For the formation of the silica shell, 12 mg of SPION dispersed in 15 mL of water are sonicated for 5 minutes and transferred to a 100 mL three-neck round-bottom flask. 5 mL of an aqueous CTAB solution (0.11 M), 0.3 mL of an aqueous NaOH solution (2 M) and 30 mL of water are added and the remaining procedure is similar to that described in section 3.1.3.

### 3.2. Synthesis of IO/ SiO<sub>2</sub>/mSiO<sub>2</sub>

To obtain these nanoparticles, iron oxide is firstly synthesised by microemulsion. Then, there is the synthesis of a non-porous silica shell to protect iron oxide from oxidation and finally, the mesoporous silica shell is obtained.

#### 3.2.1. Materials

Iron(III) chloride hexahydrate (FeCl<sub>3</sub>·6H<sub>2</sub>O, 97%), iron(II) chloride tetrahydrate (FeCl<sub>2</sub>·4H<sub>2</sub>O, 99%), hexadecyltrimethylammonium bromide (CTAB, CH<sub>3</sub>(CH<sub>2</sub>)<sub>15</sub>N(Br)(CH<sub>3</sub>)<sub>3</sub>, >99%), toluene (C<sub>6</sub>H<sub>5</sub>CH<sub>3</sub>, >99%), 1-butanol (C<sub>4</sub>H<sub>10</sub>O, >99.5%), ammonium hydroxide

Synthesis of superparamagnetic mesoporous silica nanoparticles to mediate antitumour strategies

( $\text{NH}_4\text{OH}$ , 25%), ethanol ( $\text{C}_2\text{H}_6\text{O}$ , 99.99%), tetraethyl orthosilicate (TEOS,  $\text{Si}(\text{OC}_2\text{H}_5)_4$ , 98%), ammonium nitrate ( $\text{NH}_4\text{NO}_3$ , >99%) were used as purchased without additional purification. Ultrapure water was used throughout the synthesis.

### 3.2.2. Synthesis of iron oxide

The synthesis of iron oxide by microemulsion follows the procedure of Gonçalves (2016) and Maleki *et al.* (2012). Briefly, two similar microemulsions are prepared, with 4 mL of water, 58 mL of toluene, 5.6 g of CTAB and ~4 mL of butanol (added until a transparent solution is obtained).

To one of the microemulsions, the iron oxide precursors are added: 1.50 mmol of Fe(III) and 0.74 mmol of Fe(II); to the other, 4 mL of ammonium hydroxide are added. The first microemulsion is transferred to a 250 mL reactor, where it is kept for 30 min under mechanical stirring (4000 rpm) and under  $\text{N}_2$  atmosphere. Next, the other microemulsion is added, initiating the reaction that occurs at 50°C for 1 h.

Afterwards, the nanoparticles are magnetically separated, washed 3 times with ethanol and finally dispersed in 60 mL of ethanol.



**Figure 19.** Experimental setup for the synthesis of SPIONs by microemulsion.

### 3.2.3. Synthesis of the silica shell

To obtain the non-porous silica shell around the iron oxide nanoparticles, 30 mL of these nanoparticles dispersed in ethanol are placed in a bath at 0°C under stirring. Then, 200  $\mu\text{L}$  of TEOS are added and, after 5 min of stirring, 3 mL of ammonium hydroxide are added. The reaction proceeds for 2 h under stirring at 0°C and the nanoparticles are then magnetically separated, washed three times with ethanol and redispersed in 30 mL of ethanol (Gonçalves, 2016).

Next, to obtain the mesoporous silica shell, the procedure was inspired on Avedian *et al.* (2018) and Yang *et al.* (2009) with some modifications. A solution of 0.30 g of CTAB in 20 mL of water is first prepared. Then, in a round-bottom flask, the nanoparticles dispersed in ethanol are mixed with the CTAB solution, 1 mL of ammonium hydroxide, 30 mL of ethanol and 60 mL of water. The mixture is heated to 60°C and 0.6 mL of TEOS are added to the mixture. The reaction proceeds for 2 h under reflux, is cooled to room temperature and stirred for 2h at room temperature. The nanoparticles are washed three times with ethanol.

To remove the surfactant, a solution of  $\text{NH}_4\text{NO}_3$  in ethanol is prepared by dissolving 240 mg of  $\text{NH}_4\text{NO}_3$  in 60 mL of ethanol. The nanoparticles, dispersed in 30 mL of ethanol, are added to this solution and left under magnetic stirring for 30 minutes at 60°C.

Afterwards, the nanoparticles are again washed three times with ethanol. To dry the nanoparticles, the methods mentioned in section 3.2 were employed.

### 3.3. Supercritical Drying (SCD)

Supercritical drying is used to dry the nanoparticles, avoiding their aggregation and inducing porosity.

For the supercritical fluids drying, an autoclave reactor is used with pressure and temperature control. The SCD equipment used is presented in Figure 20.



**Figure 20.** Supercritical drying equipment.

First, the nanoparticles dispersed in ethanol are transferred to test tubes. These along with glass spheres are placed inside the autoclave, which is then filled with ethanol. The autoclave is then closed with a torque wrench and all the valves are closed, except the one feeding the

reactor. Next, flushing of the system with nitrogen must be done at least five times to remove the oxygen from the system.

In order to increase the temperature, a heating mantle is used and the temperature increase pattern must be programmed in the SCD software. The temperature sequence is: room temperature for 5 minutes, 260°C for 180 minutes, 260°C for 5 minutes and room temperature for 5 minutes. The program is then started and when pressure reaches  $\approx 80$  bar, the valve of the reactor must be opened intermittently to maintain this pressure with an error of  $\pm 4$  bar. This procedure must be repeated until the temperature reaches 260°C. After this temperature is reached, the valve of the reactor is opened slightly for the pressure to drop slowly and gradually. Ethanol leaves the system in supercritical state and enters a serpentine that is in contact with ice, to cool and condensate the solvent. When air pressure is reached, the flushing process with  $N_2$  is repeated, and when the temperature reaches room temperature, the autoclave can be opened and the dried nanoparticles are stored.

### 3.4. Drug Loading and Release

To evaluate the drug loading and release capacity of the nanoparticles, epirubicin was used as model drug. Epirubicin (EPI) is an anticancer drug and an analogue of doxorubicin, mentioned in section 2.3. Its chemical structure is presented in Figure 21.

In these procedures, a solution for injection of Epirubicin (2 mg/mL) from Teva was used.

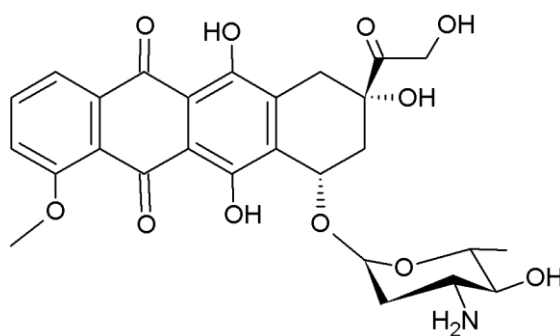


**Figure 21.** Chemical structure of epirubicin.

#### 3.4.1. Drug Loading

For the drug loading experiments, 5 mg of the synthesised MMSNs are dispersed in 3.75 mL of water and left in contact for a day. Then, 1.25 mL of an aqueous solution of EPI (2 mg/mL) are added and the mixture is placed in a roller mixer at room temperature for 24 h. After this time, the mixture is centrifuged for 10 min at 4000 rpm to collect the nanoparticles



and the supernatant is kept to posteriorly calculate the loading content. The nanoparticles are washed twice with water and centrifuged and the supernatants are also kept.

In order to evaluate the amount of loaded EPI, the supernatants are analysed by UV-Vis spectroscopy at a wavelength of 480 nm (Chang *et al.*, 2010) (vd. section 3.6.8). The loading content and entrapment efficiency can then be calculated by the following equations:

$$\text{Loading content (LC) (\%)} = \frac{\text{mass of EPI in NPs}}{\text{mass of drug loaded NPs}} \times 100 \quad (5)$$

$$\text{Entrapment efficiency (EE) (\%)} = \frac{\text{mass of EPI in NPs}}{\text{initial mass of EPI}} \times 100 \quad (6)$$

### 3.4.2. Drug Release

For the release experiments, drug loaded nanoparticles are dispersed in PBS (pH=7.4) in a concentration of 0.5 mg/mL. The glass vial containing the suspension is put in a shaking incubator at 37°C and with a shaking speed of 160 rpm. At pre-established times, the flask is removed from the incubator and placed on top of a magnet for 5 min, in order for the nanoparticles to magnetically deposit at the bottom. Then, a 0.5 mL aliquot is removed into an Eppendorf for the UV-Vis readings (vd. section 3.6.8). The aliquot is reintroduced in the vial using a micropipette in order to account for the lost volume, since not all of it is reintroduced back into the vial because some of it adheres to the walls of the Eppendorf and to the walls of the microplate wells.

## 3.5. Characterization Techniques

### 3.5.1. Thermogravimetric Analysis (TGA)

Thermogravimetric analysis is a method of thermal analysis that measures the mass change of a sample under pre-programmed conditions. The weight loss can be measured as function of temperature or as a function of time with constant temperature (Loganathan *et al.*, 2017).

In TGA, the sample is put in a crucible and placed inside a furnace. The crucible is connected to the weighting arm of an electronic balance of high precision, which measures the mass change of the sample during the pre-established program (Loganathan *et al.*, 2017).

In this work, TGA is used to quantify the oleylamine coating of the iron oxide nanoparticles and to obtain information about the extent of the ligand exchange procedure on iron oxide with APTES. The equipment used was a *TA Instruments SDTQ600* and the previously dried samples were heated to 600°C, with a heating rate of 10°C/min.

### 3.5.2. Fourier-Transform Infrared Spectroscopy (FTIR)

Fourier-Transform Infrared Spectroscopy is commonly used to study the chemical structure of organic and some inorganic molecules present in a certain sample. In this case, it is used to confirm the presence of both iron oxide and silica in the nanoparticles and identify the main existing chemical groups.

In this technique, infrared radiation is passed through a sample and part of this radiation is absorbed. This absorption occurs at certain energy values that correspond to the frequencies of vibration of chemical bonds in the molecules (Stuart, 2004). Because each chemical bond has a different frequency of vibration, it is possible to identify the chemical bonds and groups present in the compounds of the sample.

With this instrument, an infrared spectrum is obtained, which represents the percentage of transmitted/absorbed energy as a function of the wavelength of the incident radiation. These equipments can work in different infrared regions but most of them work in the mid-infrared region, which is between  $4000\text{ cm}^{-1}$  and  $400\text{ cm}^{-1}$  (Stuart, 2004).

For the characterization of the synthesised materials, the analysis is performed in a *Jasco FT/IR 4200* spectrometer, in the  $4000\text{ cm}^{-1}$  to  $400\text{ cm}^{-1}$  region and with a resolution of  $4\text{ cm}^{-1}$ .

To prepare the samples, KBr is finely milled and then dried at  $60^{\circ}\text{C}$  for at least one day. Then, for each sample, 78.5-80 mg of KBr and 0.20-0.30 mg of dried nanoparticles are needed. To obtain the pellet, these are mixed and milled until a homogeneous powder is obtained. Finally, the sample is pressed into a thin, translucent pellet.

Before the acquisition of the sample spectrum, it is necessary to obtain a baseline with a pellet only containing KBr. Afterwards, the sample pellet is introduced in the equipment and infrared radiation passes through sample, thus generating the infrared spectrum.

### 3.5.3. Dynamic Light Scattering (DLS)

Dynamic Light Scattering is widely used to obtain the size distribution and average size of particles of submicron size suspended in a liquid. In this work, it is used to obtain the hydrodynamic diameter of the final magnetic mesoporous silica nanoparticles.

In this technique, a suspension is illuminated with a laser beam, which interacts with the particles. This interaction causes the scattering of light in several directions and, due to Brownian motion, the position of the suspended particles varies, which causes fluctuations in the intensity of the scattered light (Figueiredo, 2013). These fluctuations are analysed as a function of time, in order to obtain the average diffusion coefficient of the particles ( $D$ ), which in turn can be converted in the hydrodynamic diameter ( $D_H$ ) by the Stokes-Einstein equation:

$$D_H = \frac{k_B T}{3\pi\eta D} \quad (7)$$

where  $k_B$  is the Boltzmann's constant,  $T$  is the temperature and  $\eta$  is the viscosity.

The intensity of scattered light is measured by a detector positioned at a certain angle (typically,  $90^\circ$  or  $175^\circ$ ) and the signal created by the detector is then fed to a correlator, which generates a correlation function. The data obtained in the correlation curve needs to be deconvulsed and different methods exist (e.g. cumulants method, CONTIN, NNLS), depending on the polydispersity of the particles (Figueiredo, 2013).

The size distribution is typically based on intensity, but volume and number distributions can also be obtained.

For the analysis of the produced nanoparticles, the equipment used was a *Zetasizer Nano ZS* from *Malvern Instruments*. To prepare the samples, 0.20 mg of dried nanoparticles are dispersed in 2 mL of ultrapure water (pH=7) and sonicated in an ultrasounds probe for 10 min. The sample is then transferred to a cuvette and inserted in the equipment.

The analysis is made in the *Zetasizer Software*, available with the equipment.

#### 3.5.4. Zeta Potential

Particles with a surface net charge that are dispersed in a liquid attract ions of the opposite charge (counter-ions) to neutralize this surface charge. These counter-ions are strongly bound around the surface, creating the Stern layer. Outside of this layer, other counter-ions are still attracted to the particle, but these are also repelled by the Stern layer and by each other, creating a diffuse layer. In this layer, the concentration of counter-ions decreases until it is in equilibrium with their concentration in the bulk liquid, while the concentration of the ions with the same charge as the surface increases with the distance (Xu, 2002).

Between the Stern layer and the diffuse layer, an imaginary boundary can be defined, called the shear plane. When a particle moves, all the liquid and ions existing between the shear plane and the surface of the particle move along with it (Xu, 2002). However, the liquid and other species beyond this plane don't move when the particle moves. Zeta potential is the charge of a particle at this shear plane and, by knowing its value, it is possible to evaluate the electrostatic stabilization of a suspension. If the particles in a suspension have a large negative or positive zeta potential, there is high repulsion between the particles and the suspension is stable. Usually, particles with a zeta potential higher than +30 mV or lower than -30 mV are considered stable.

The equipment used to determine the zeta potential is based on electrophoretic light scattering. An electric field is applied to the suspension and the charged particles will move to

Synthesis of superparamagnetic mesoporous silica nanoparticles to mediate antitumour strategies

an electrode of the opposed signal. The motion of the particles causes the scattering of light and its frequency will be different from the frequency of the incident radiation due to Doppler effect. This frequency change can be related to the electrophoretic mobility of the particles, which is then converted to zeta potential using Henry's equation (Xu, 2002).

Given the similarity between these instruments and a DLS equipment, these measurements are most often combined in an equipment that can do both. For the present work, the *Zetasizer* from *Malvern Instruments* was used simultaneously with DLS measurements. The samples analysed were also the final nanoparticles in order to evaluate their stability.

The sample preparation is already described in section 3.5.3 and the cuvettes used are zeta potential cells, which have the electrodes inside. It is also important to mention that the suspensions are prepared at pH=7, because the zeta potential is affected by this parameter.

### **3.5.5. Transmission Electron Microscopy (TEM)**

Transmission electron microscopy is used in the characterization of nanomaterials, giving information about the size and morphology of these materials. In this work, it was used to obtain images of the magnetic mesoporous silica nanoparticles and obtain information about their size distribution, morphology and porosity.

In TEM, an electron beam is produced at the top of the equipment and it is focused towards the sample. When the beam reaches the sample, it penetrates it and interacts with it. Electrons are transmitted through the sample, which are then analysed and a two-dimensional image of the sample is obtained, providing detailed information about the internal structure of the particles. The samples need to be thin and transparent to electrons, which limits the size of the materials that can be observed in TEM (Figueiredo, 2013).

The equipment used in this work was a *FEI Tecnai G2*. The employed accelerating voltage was 200 kV and bright field imaging was used. To prepare the samples, the nanoparticles were dispersed in ethanol and sonicated. The grids used were 200 mesh copper with a carbon film from *Agar Scientific* and they were dipped in the suspension of nanoparticles and the solvent was evaporated before the grids were inserted in the equipment.

### **3.5.6. Scanning Electron Microscopy coupled with Energy Dispersive X-Ray Spectroscopy (SEM-EDS)**

Scanning electron microscopy is used to study the size distribution, morphology and topography of the surface of the samples. In this work, SEM-EDS was used to obtain images of the final nanoparticles, obtain information about their topography and confirm the presence of specific elements in the nanoparticles.

In SEM, similarly to TEM, there is an incident electron beam. However, instead of going through the sample as in TEM, this electron beam is scanned over the surface of the sample (Figueiredo, 2013; Goodhew *et al.*, 2001). When this beam comes in contact with the sample, secondary electrons are ejected from the outer shell of the sample atoms and backscattered electrons from the electron beam and characteristic X-rays are also emitted (Figueiredo, 2013).

The detection of secondary electrons is important to obtain good topographical images, while backscattered electrons are related to the atomic number of sample atoms and their detection allows the identification of regions with elements of different atomic number (Figueiredo, 2013; Goodhew *et al.*, 2001). Additionally, the characteristic X-rays can be detected through EDS, in order to obtain the abundance of specific elements in the sample (Figueiredo, 2013).

For SEM, the sample needs to be electrically conductive. When this is not the case, the sample is coated, typically with gold, by sputter deposition (Figueiredo, 2013).

To prepare the samples, the dried nanoparticles were deposited in carbon tape and subjected to gold sputter deposition for 20 seconds. The SEM equipment was a *Compact/VP Compact FESEM* from *Zeiss Merlin* and the EDS was a *XMaxN* from *Oxford*.

### 3.5.7. Vibrating Sample Magnetometer (VSM)

The vibrating sample magnetometer is a technique used to obtain different magnetic properties of a material, such as its magnetic moment and magnetic hysteresis, including its coercivity and remanence (Thompson & Oldfield, 1986).

The VSM is based on Faraday's law of electromagnetic induction, which states that, when there is a change in flux through a coil, an electromotive force is created in the coil (Buschow & de Boer, 2003b; Thompson & Oldfield, 1986). For a coil with  $n$  turns and a cross-section area  $a$ , the electromotive force is given by:

$$V = -na \frac{dB}{dt} \quad (8)$$

where  $B$  is the magnetic flux density. When the coil is subjected to a constant magnetic field ( $H$ ),  $B$  is expressed by the following equation:

$$B = \mu_0 H \quad (9)$$

where  $\mu_0$  is the permeability constant in vacuum. If a material with magnetization  $M$  is placed in the coil, equation (10) applies and the respective change in flux is given by equation (11).

$$B = \mu_0 (H + M) \quad (10)$$

$$\Delta B = \mu_0 M \quad (11)$$

By combining equations (8) and (11), the equation (12) is obtained:

$$Vdt = -na\mu_0M \quad (12)$$

It is noticeable by equation (12) that the output signal of the coil is proportional to the magnetization ( $M$ ) but independent of the applied magnetic field ( $H$ ).

Following this principle, a sample in the VSM is submitted to a sinusoidal motion of frequency  $\nu$  under a constant magnetic field ( $H_0$ ) and the corresponding voltage is detected in the pick-up coils. The intensity of the output signal of these coils is proportional to the magnetic moment of the material (Buschow & de Boer, 2003b; Thompson & Oldfield, 1986). Because this signal is also proportional to the vibration amplitude and the frequency  $\nu$ , a vibrating capacitor is used to create a reference signal and eliminate the error associated with variations in the vibration amplitude and the frequency  $\nu$ . Therefore, the final output signal obtained depends only on the magnetic moment of the sample (Buschow & de Boer, 2003b).

This technique was used to analyse both the final magnetic silica nanoparticles and iron oxides. The analysis was performed with a cryogen-free Physical Properties System from *Dynacool PPMS*, with an operating vibrating frequency of 40 Hz and an amplitude of 2 mm in the central area of the coils. The samples were previously dried.

### 3.5.8. Mössbauer Spectroscopy

Mössbauer spectroscopy gives information about the chemical structure and magnetism of materials. It is based on the Mössbauer effect, which involves the resonant absorption of gamma radiation by nuclei in solids.

In this technique, there is a source of  $^{57}\text{Co}$  (for iron samples), which decays into an excited  $^{57}\text{Fe}$  nuclei and then into ground state  $^{57}\text{Fe}$ , emitting gamma radiation. The source oscillates slightly, which leads to small variations in the frequency of the emitted gamma radiation, due to the Doppler effect. This radiation goes through the sample and a detector measures the transmitted gamma radiation as function of the velocity of the source. With the oscillation of the source, the energy of the gamma radiation can match a nuclear transition in the sample, leading to resonant absorption of the radiation (Blundell, 2001). Consequently, a peak is recorded in the spectrum. In different nuclear environments, modifications in the spectrum occur, depending on the interactions between the nuclei and the surrounding environment. The number and position of the maxima of this spectrum are determined by the hyperfine interactions, which lead to a resultant interaction that reflects itself in the complexity of the absorption spectrum. The nuclei can be subjected to three types of hyperfine interactions, which are illustrated in Figure 22 (Cornell & Schwertmann, 2003):

- i. Isomer shift ( $\delta$ ): function of the densities of the s electrons surrounding the nucleus that causes a displacement of the spectrum; gives information about the coordination number, valency and spin of the iron atoms in the sample.
- ii. Quadrupole interaction ( $\Delta E_Q$ ): created when a gradient in the electric field acts on the nucleus, causing the separation of the nuclear energy levels; provides details about the iron sites distortion.
- iii. Magnetic hyperfine field ( $B_{hf}$ ): caused by magnetic dipole interaction; gives details about the valence and magnetic properties of the material.

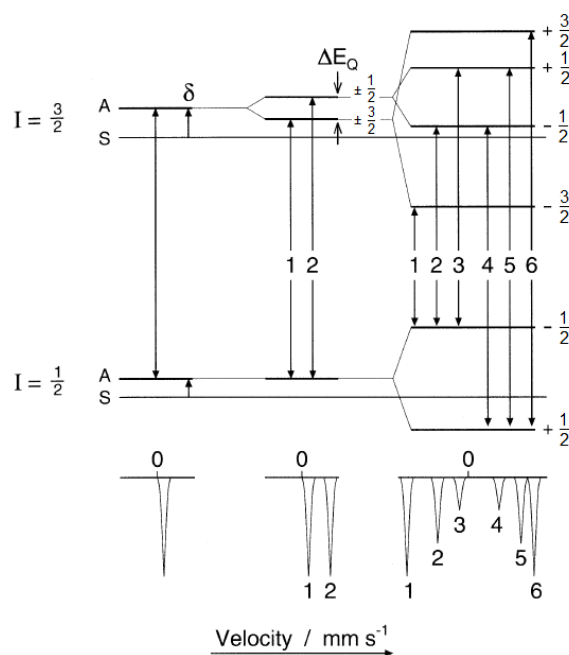


**Figure 22.** Different hyperfine interactions in a  $^{57}\text{Fe}$  nucleus: isomeric shift (left), quadrupole splitting (center) and magnetic hyperfine field (right) (Cornell & Schwertmann, 2003).

After obtaining the Mössbauer spectrum, a set of Lorentzian lines can be fitted to the data, making it possible to assess the magnitude of these hyperfine interactions. The obtained hyperfine parameters can then be compared to reference values found in the literature, giving information about the phases present in the sample and their amount, as well as their magnetic behaviour.

Mössbauer spectroscopy is used in this work to identify the phases of iron oxide present in the IO-OAm/mSiO<sub>2</sub> and IO-APTES/mSiO<sub>2</sub> nanoparticles. The spectra were obtained in a *Wissel* spectrometer, using  $^{57}\text{Fe}$  as isotope. A source of  $^{57}\text{Co}$  with a decay energy of 14.4 keV and embedded in a matrix of Rh with an activity of 25 mCi was used. The measurements were performed at room temperature and  $\alpha$ -Fe was used as reference to obtain the isomeric shift.

### 3.5.9. Ultraviolet-Visible (UV-Vis) Spectroscopy

UV-Vis spectroscopy is commonly used to quantify different analytes. In this work, it is used to determine quantitatively the loading and release of epirubicin in the nanoparticles.

In this type of spectroscopy, electromagnetic radiation in the ultraviolet (200-400 nm) or visible (400-800 nm) regions is absorbed by the molecules, leading to transitions between electronic levels in the molecules (Chirayil *et al.*, 2017; Perkampus, 1992).

UV-Vis spectroscopy obeys the Beer-Lambert law, which is presented in equation (13):

$$A = \log \left( \frac{I_0}{I} \right) = \varepsilon \cdot d \cdot c \quad (13)$$

where  $A$  is the absorbance,  $I_0$  is the intensity of the monochromatic light received by the sample,  $I$  is the intensity of the light transmitted through the sample,  $\varepsilon$  is the molar absorptivity,  $d$  is the pathlength of the light through the sample and  $c$  is the concentration of the substance absorbing the light (Perkampus, 1992). This law states that, when a beam of a monochromatic light passes through a substance, the absorbance is proportional to the concentration of the substance which absorbs the light.

In this technique, quartz or glass cuvettes or microplates are used to hold the sample. However, part of the incident light is scattered on the surface of these materials and, therefore, a reference measurement is needed to eliminate this interference (Perkampus, 1992). Furthermore, since UV-Vis spectroscopy is used with solutions, in the reference measurement, the cuvette is filled with the solvent, in order to account for the interference of the matrix (Perkampus, 1992).

The used equipment was a *SpectraMax Plus 384* from *Molecular Devices*. In this work, 96-well microplates were used and 0.100 mL were introduced in each well. Triplicates were made of each aliquot and the mean of the three values was considered. In order to obtain the calibration curve, different solutions of epirubicin were prepared, in aqueous media (loading experiments) and in PBS (release experiments), with concentrations of 25, 12.5, 6.25, 3.125 and 1.5625  $\mu\text{g/mL}$  and 14.0, 7.0, 3.5, 1.75 and 0,875  $\mu\text{g/mL}$ , respectively. The absorbance of the solvent was measured and subtracted to the measured absorbances of the aliquots. Additionally, the analysis of the aliquots from the loading tests was performed after diluting the samples with a dilution factor of 20.



## 4. Results and Discussion

In this chapter, the synthesised nanoparticles are firstly presented in terms of their physical, chemical and magnetic properties, followed by their drug loading and release capacity. The sections were defined according to the nanoparticles composition/hierarchical architecture.

### 4.1. IO-OAm/mSiO<sub>2</sub>

#### 4.1.1. Synthesis Aspects and Physicochemical Characterization

As mentioned in section 3.1, to obtain these nanoparticles, iron oxide was synthesised by thermal decomposition, then transferred into water using chloroform and an aqueous CTAB solution and, finally, there was the formation of the mesoporous silica shell, using TEOS as the silica precursor. The surfactant was then removed with a solution of NH<sub>4</sub>NO<sub>3</sub> in ethanol.

Initially, for one synthesis, in the procedure of the formation of silica shell, water was added alongside TEOS and ethyl acetate, instead of in the beginning. The nanoparticles from this synthesis will be denoted IO-OAm/mSiO<sub>2</sub>\* throughout this chapter. For these nanoparticles, the two drying processes – supercritical drying (SCD) and ambient pressure drying (APD) at 60°C – were studied.

The nanoparticles synthesised following the procedure of section 3.1.3. are denoted IO-OAm/mSiO<sub>2</sub>.

It was observed that the nanoparticles dried by SCD had a greyish colour, while the ones dried by APD were light brown, as shown in Figure 23 . Moreover, when trying to disperse the SCD nanoparticles in water, it was found that they had become hydrophobic. It was hypothesised that, during the SCD process with alcohol at high temperatures, ethanol reacted with the silanol groups on the surface of the nanoparticles, creating hydrophobic ethoxy groups (-OCH<sub>2</sub>CH<sub>3</sub>) (Pierre & Rigacci, 2011).

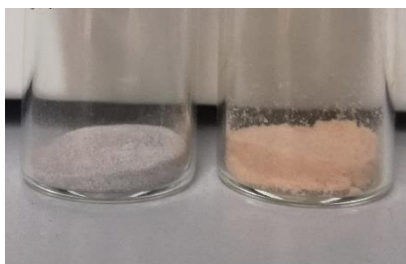


**Figure 23.** IO-OAm/mSiO<sub>2</sub>\* nanoparticles dried by SCD (left) and APD (right).

### Thermogravimetric Analysis

As mentioned before, in order to obtain the quantity of oleylamine coating on the SPIONs obtained by thermal decomposition, TGA was used. The obtained thermogram for these nanoparticles is presented in Figure 24.

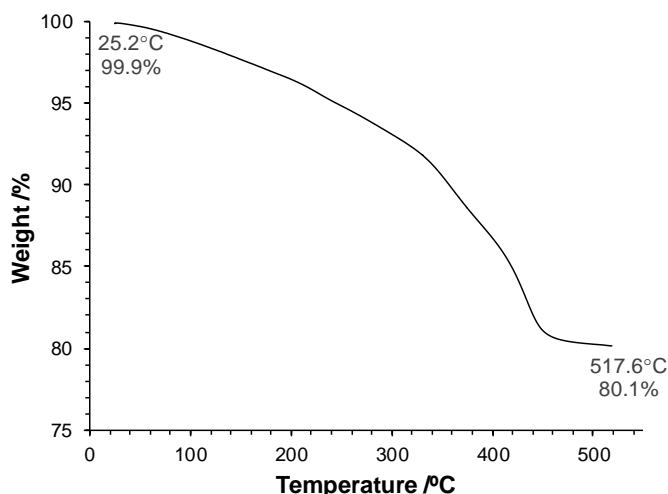


**Figure 24.** Thermogram of the oleylamine-coated SPIONs.

As it can be seen in Figure 24, the sample started losing weight with the increase in temperature, particularly after 300°C and until around 450°C, where the sample weight became almost constant. At this temperature, organic matter, in this case oleylamine, has decomposed. Considering that iron oxide is stable until this temperature (Cornell & Schwertmann, 2003), this weight loss can be attributed to the organic coating, which can include both oleylamine and residual benzyl ether (Santos, 2015). Therefore, the nanoparticles are made of 80.1% of iron oxide, in weight.

### Fourier-Transform Infrared Spectroscopy

FTIR was used to confirm the presence of iron oxide and silica in the nanoparticles. The results obtained for SPIONs produced by thermal decomposition and for the MMSNs dried by APD and SCD are presented in Figure 25.

In the spectrum obtained for SPIONs, the expected band characteristic of these nanoparticles can be found, such as the band between 550 and 800  $\text{cm}^{-1}$  of the Fe-O bonds (Pedrosa *et al.*, 2015). On the other hand, the presence of oleylamine can also be confirmed by FTIR. The band at around 3400  $\text{cm}^{-1}$  is related to the N-H stretching vibration of oleylamine, which can be further confirmed by the baseline reduction at around 3000  $\text{cm}^{-1}$ , as well as the band at  $\sim 1600 \text{ cm}^{-1}$  that can be attributed to the bending of the N-H bond. The three bands between 2800 and 3000  $\text{cm}^{-1}$  and between 1350 and 1500  $\text{cm}^{-1}$  correspond to C-H stretching

and bending vibrations, respectively, in the alkyl chain of oleylamine. Moreover, the band at around  $\sim 1650\text{ cm}^{-1}$  is related to the stretching in the C=C bond in this compound. The small bands existent between  $1000\text{ cm}^{-1}$  and  $1300\text{ cm}^{-1}$  can be due to the C-N vibration of oleylamine and to the C-O-C vibrations of residual benzyl ether present in the nanoparticles.

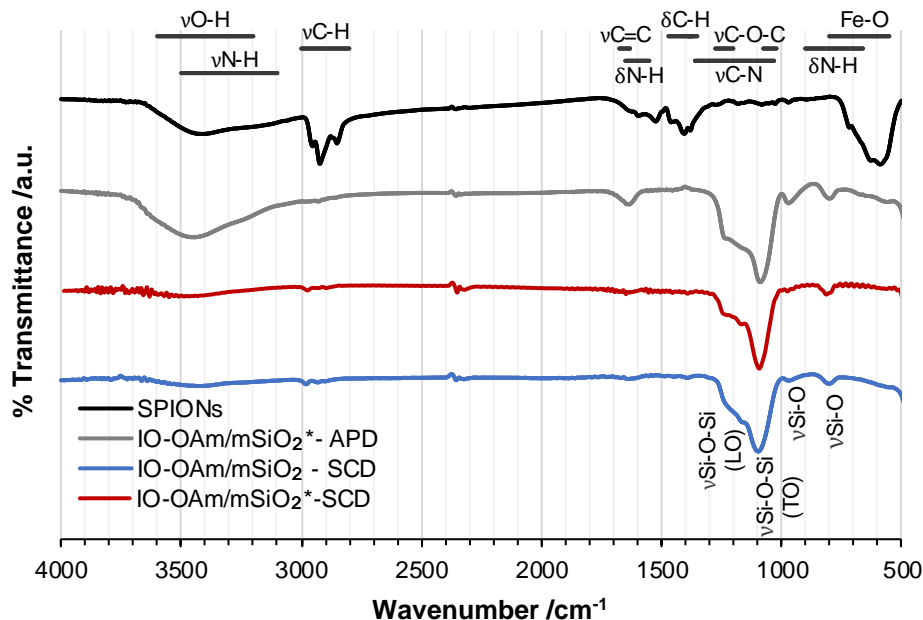


**Figure 25.** FTIR spectra obtained of the SPIONs produced by thermal decomposition and of the final magnetic MSNs dried by APD and SCD. ( $\nu$  – stretching,  $\delta$  – bending.)

In the spectra of IO-OAm/mSiO<sub>2</sub> and IO-OAm/mSiO<sub>2</sub>\*, the presence of silica can be confirmed by the four characteristic band: the band at  $\sim 1100\text{ cm}^{-1}$  and the shoulder at  $\sim 1200\text{ cm}^{-1}$  that correspond to the asymmetric stretching Si-O-Si vibrations, the band at  $\sim 970\text{ cm}^{-1}$  related to the Si-OH in-plane stretching and the band at  $\sim 800\text{ cm}^{-1}$  that be attributed to the Si-O in-plane stretching vibration in the  $\equiv\text{Si-O-Si}\equiv$  bonds (Al-Oweini & El-Rassy, 2009). Furthermore, there is also a small band around  $550\text{ cm}^{-1}$ , which is in the region of the Fe-O vibration. This band, as well as others, appear very small because of the presence of silica in high quantity.

The spectra of IO-OAm/mSiO<sub>2</sub> - SCD and IO-OAm/mSiO<sub>2</sub>\* - SCD were very similar, showing the same bands.

The spectrum of IO-OAm/mSiO<sub>2</sub>\*- APD nanoparticles has a broad band at  $3450\text{ cm}^{-1}$  that corresponds to the O-H stretching vibration of the silanol groups on the surface of the nanoparticles and adsorbed water. This vibration mode almost does not appear in SCD spectra, which can be because, during the drying, when high temperatures are reached, ethanol reacts with the silanol groups, creating -OCH<sub>2</sub>CH<sub>3</sub> groups on the surface, as mentioned before. However, this could not be confirmed by FTIR because, once again, the overwhelming presence

of silica makes the visualization of smaller band difficult. Additionally, observing the spectrum of IO-OAm/mSiO<sub>2</sub>\*- APD, there is a band at ~1620 cm<sup>-1</sup>, which does not appear on SCD spectra. This band appears in the region of H-O-H vibration, suggesting that water was adsorbed by the sample, due to the hydrophilicity of both KBr and the nanoparticles.

### Dynamic Light Scattering and Zeta Potential

In the DLS measurements, it was found that there was considerable aggregation of the nanoparticles as well as high size dispersity, given by the polydispersity index (PDI). The estimate of the mean diameter calculated by the software is influenced by presence of very large aggregates and the high PDI, which, for some nanoparticles, led to an overestimation of the diameter. Therefore, more attention was given to the obtained intensity peaks than to the mean diameter. The results obtained in the DLS measurements are presented in Table 4.

**Table 4.** DLS results for the different IO-OAm/mSiO<sub>2</sub> samples.

NPs	Replicate	Intensity Peaks									PDI	$\bar{d}$ /nm
		Peak /nm	St. Dv. /nm	Area (%)	Peak /nm	St. Dv. /nm	Area (%)	Peak /nm	St. Dv. /nm	Area (%)		
IO-OAm/mSiO <sub>2</sub> *-APD	1	-	-	-	799.6	109.2	100	-	-	-	0.953	3524
	2	-	-	-	784.5	135.8	100	-	-	-	1.00	3035
	3	-	-	-	861.1	115.3	100	-	-	-	0.910	4134
	Mean				815.1	120.1					0.954	3531
IO-OAm/mSiO <sub>2</sub> *-SCD	1	156.1	32.5	18.2	810.8	178.8	81.8	-	-	-	0.791	1651
	2	116.3	15.4	12.1	684.9	128.2	87.9	-	-	-	0.788	1357
	3	153.7	23.1	15.9	744.5	156.8	84.1	-	-	-	0.693	1177
	Mean	142.0	23.7		746.7	154.6					0.757	1395
IO-OAm/mSiO <sub>2</sub> -SCD	1	92.88	20.31	19.1	507.6	160.7	79.4	5560	0	1.5	0.577	381.3
	2	88.45	21.18	17.9	387.8	136.5	78.2	5469	246	3.9	0.516	402.2
	3	-	-	-	525.9	388.8	93.8	5154	510	6.2	0.693	351.9
	Mean	90.7	20.75		473.8	228.7		5394.3	252.03		0.595	378.5

Observing at the results obtained for IO-OAm/mSiO<sub>2</sub>\* nanoparticles, it is notorious that with SCD the nanoparticles are smaller, because they aggregate less during the drying process. They have an intensity peak at around 142 nm, while the APD nanoparticles only have an intensity peak at around 815 nm. Moreover, the PDI values are higher for the APD samples, which is also related to the disordered aggregation during the drying process that leads to high dispersity in the nanoparticles' size.

On the other hand, in the IO-OAm/mSiO<sub>2</sub> nanoparticles, which were only dried by SCD, the first two intensity peaks occur at diameter values considerably smaller than for IO-OAm/mSiO<sub>2</sub>\* - SCD, thus indicating that IO-OAm/mSiO<sub>2</sub> are smaller. The intensity peak

above 5000 nm can be attributed to large aggregates. Additionally, the PDI values for these nanoparticles were also lower. The IO-OAm/mSiO<sub>2</sub> nanoparticles have a mean diameter of 378.5 nm. However, it is important to consider that when using intensity distributions, even though the bigger particles might be present in smaller number, they scatter more light than small particles, thus leading to diameter values that might be higher than the number-weighted mean diameter. Therefore, since there are different peaks, one can just perceive that there are nanoparticles with a diameter around 90.7 nm, while others have a diameter of 473.8 nm.

The nanoparticles were also characterized in terms of the zeta potential in water (pH=7) and the obtained results are present in Table 5.

**Table 5.** Zeta potential of the different IO-OAm/mSiO<sub>2</sub> samples

Nanoparticles	Replicate	Zeta Potential /mV	St. Dv. /mV
<b>IO-OAm /mSiO<sub>2</sub>* -APD</b>	1	-16.3	3.7
	2	-16.2	3.6
	3	-16.9	3.8
	Mean	-16.5	3.7
<b>IO-OAm /mSiO<sub>2</sub>* -SCD</b>	1	-26.4	3.8
	2	-27.7	3.5
	3	-28.3	3.6
	Mean	-27.5	3.6
<b>IO-OAm /mSiO<sub>2</sub> - SCD</b>	1	-21.5	4.3
	2	-21.9	3.5
	3	-20.5	4.7
	Mean	-21.3	4.2

As expected, the zeta potential of the nanoparticles is negative, due to the negative partial charge of the silanol groups on the surface. Moreover, the highly negative zeta potential is also an indication that the step to remove the surfactant was successful, because CTAB has a positive charge.

Comparing the two types of drying used, the nanoparticles obtained by SCD have more negative zeta potential than those dried by APD, which can be related to the porosity of the nanoparticles. Supercritical fluids drying is known to preserve the porosity in the nanoparticles, while APD leads to the collapsing of pores. Therefore, particles dried by SCD have higher surface area and, consequently, higher zeta potential.

All three samples have zeta potential between -30 and 30 mV, indicating they do not form stable suspensions in water.

### Transmission Electron Microscopy

TEM was used to study the size distribution of the IO-OAm/mSiO<sub>2</sub>\* nanoparticles. The IO-OAm/mSiO<sub>2</sub> nanoparticles were not analysed by TEM. Furthermore, the SPIONs incorporated in the nanoparticles were also not characterized by TEM but they are expected to have a mean size of 9.174±2.974 nm, according to the results of similar nanoparticles characterized by Santos (2015).

In Figure 26 and Figure 27, images obtained by TEM as well as the histograms of the size distribution are presented for IO-OAm/mSiO<sub>2</sub>\*-SCD and for IO-OAm/mSiO<sub>2</sub>\*-APD, respectively. When observing the nanoparticles through TEM, it was noticeable that the aggregation between the nanoparticles was extensive, even though they were sonicated for a long period. It was hypothesised that this could be due to chemical bonding, due to further condensation reactions between silanols.

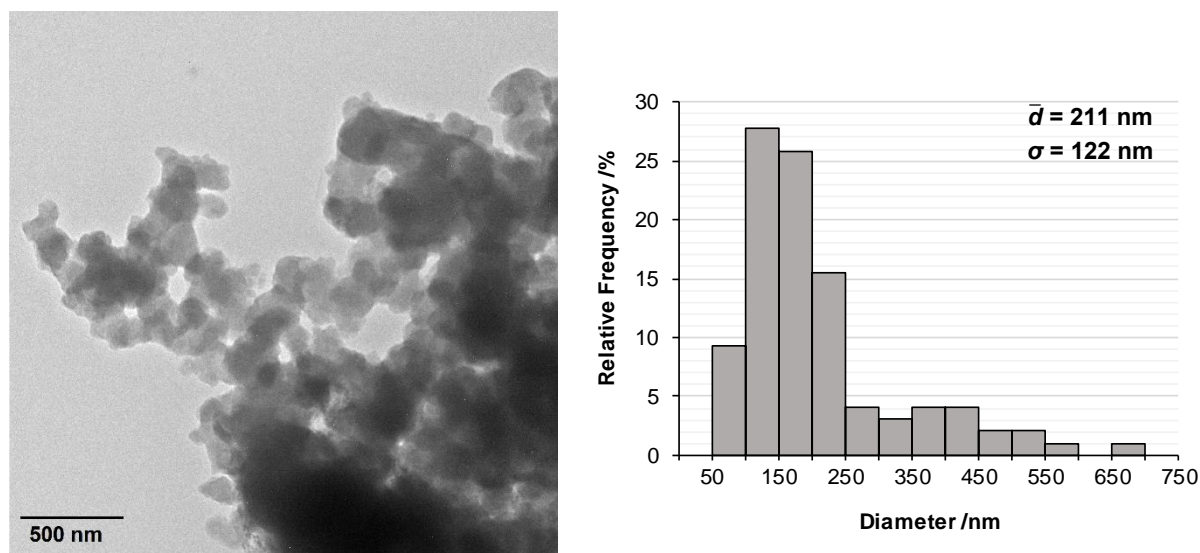


**Figure 26.** TEM image and histogram of the size distribution (n=100) for the IO-OAm/mSiO<sub>2</sub>\* - SCD nanoparticles.

The IO-OAm/mSiO<sub>2</sub>\*-SCD nanoparticles are very aggregated and polydisperse and do not have a regular shape (Figure 26). The iron oxide cores cannot be seen in the TEM images, which can be due to the fact that they are very small in size in comparison to the silica shell. The histogram created from the analysis of the TEM images using *Image J* reveals that the nanoparticles have a mean diameter of 211 nm with a standard deviation of 122 nm. The standard deviation is very high, which is an indication of the high polydispersity of the nanoparticles.

Figure 27 shows aggregation and size dispersity also for the IO-OAm/mSiO<sub>2</sub>\*-APD nanoparticles. According to the correspondent histogram, they have a mean size of 238 nm with a standard deviation of 137 nm. Both the mean and the standard deviation of the diameter are

higher than in the case of the IO-OAm/mSiO<sub>2</sub>\*-SCD, which confirms the results obtained in DLS. Furthermore, according to the histogram, there are more nanoparticles bigger than 550 nm, which, as already mentioned, might be due to the uncontrolled aggregation and polycondensation during drying.

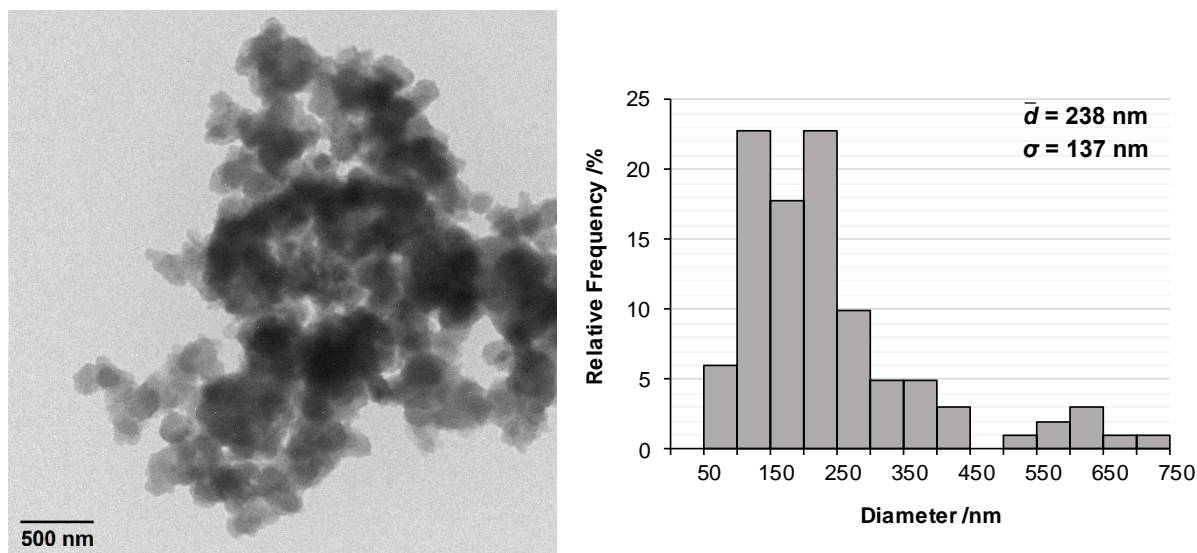


**Figure 27.** TEM image and histogram of the size distribution ( $n=100$ ) for the IO-OAm/mSiO<sub>2</sub>\* - APD nanoparticles.

The mean diameters obtained by TEM are much smaller than those obtained in DLS, which was expected, because DLS only provides good results for the analysis of monodisperse samples. Moreover, DLS considers the hydrodynamic diameter, while TEM shows the real particles' contours.

TEM was also used to investigate the porosity of the nanoparticles, using higher resolution in order to visualise the pores (Figure 28).

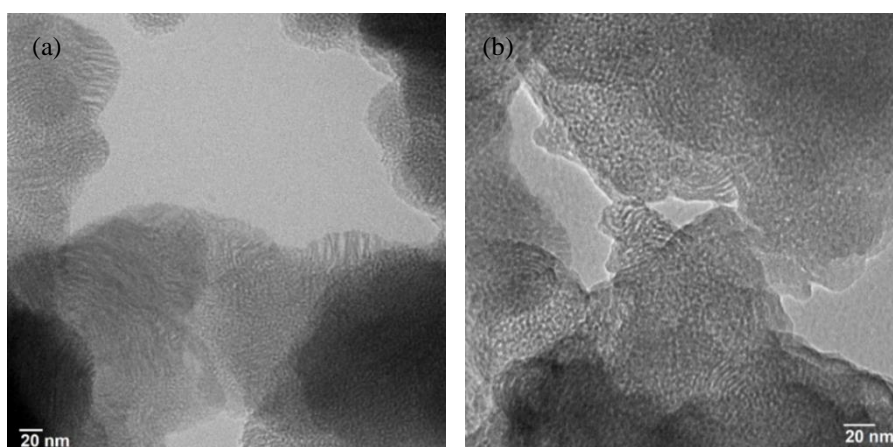


**Figure 28.** Images obtained by TEM for (a) IO-OAm/mSiO<sub>2</sub>\*-APD and (b) IO-OAm/mSiO<sub>2</sub>\*-SCD particles.

As it can be seen in Figure 28, the nanoparticles present lighter zones in their structure, where more electrons are transmitted, and these zones might correspond to the pores of the nanoparticles. At the periphery of the particles, brush-like structures are also visible, as if the surfactant was removed and left small channels in silica.

Since it is known that when looking at magnetic samples through TEM they can cause deviations in the electron beam and shifts in the images, it is important to assure that what appears to be the pores is not an effect of this interaction. Given the good focus and quality of the obtained images, it is believed that these zones correspond to porosity and are not an effect of the presence of magnetic nanoparticles. Furthermore, these images were compared to those of mesoporous silica nanoparticles without magnetic cores and similar structures were found in them (Suzuki *et al.*, 2004). Thus, it is possible to conclude that the IO-OAm/mSiO<sub>2</sub>\* particles indeed present porosity.

### Scanning Electron Microscopy coupled with Energy Dispersive X-Ray Spectroscopy

SEM was used to have an image in depth of the nanoparticles. In Figure 29, SEM micrographs of IO-OAm/mSiO<sub>2</sub>\*- APD and IO-OAm/mSiO<sub>2</sub>\*- SCD are presented.

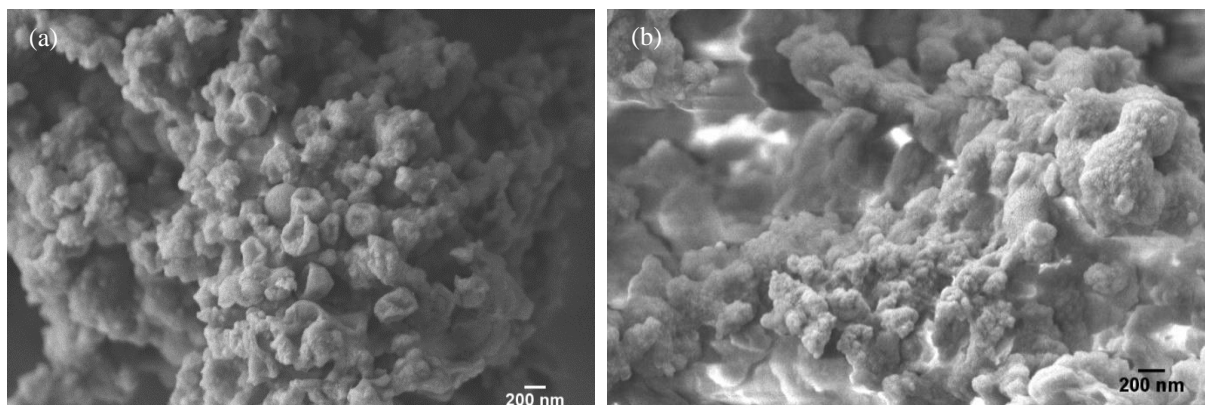


**Figure 29.** SEM image of (a) the IO-OAm/mSiO<sub>2</sub>\* - APD and (b) the IO-OAm/mSiO<sub>2</sub>\* - SCD nanoparticles.

The microstructure of the IO-OAm/mSiO<sub>2</sub>\*- APD nanoparticles shown in Figure 29 looks as if they were spherical and collapsed, which does not happen for the IO-OAm/mSiO<sub>2</sub>\* - SCD particles. This can be related to the drying method, because APD leads to collapsing of the pores and shrinking and, thus, can be responsible for the presented morphology of the nanoparticles.

Since IO-OAm/mSiO<sub>2</sub> - SCD were not characterized by TEM, SEM was used to study the size distribution of these nanoparticles. Additionally, EDS was also used on this sample to confirm the presence of iron oxide in the nanoparticles. In Figure 30, images obtained in SEM, as well as a histogram of the size distribution and the EDS spectrum are presented.



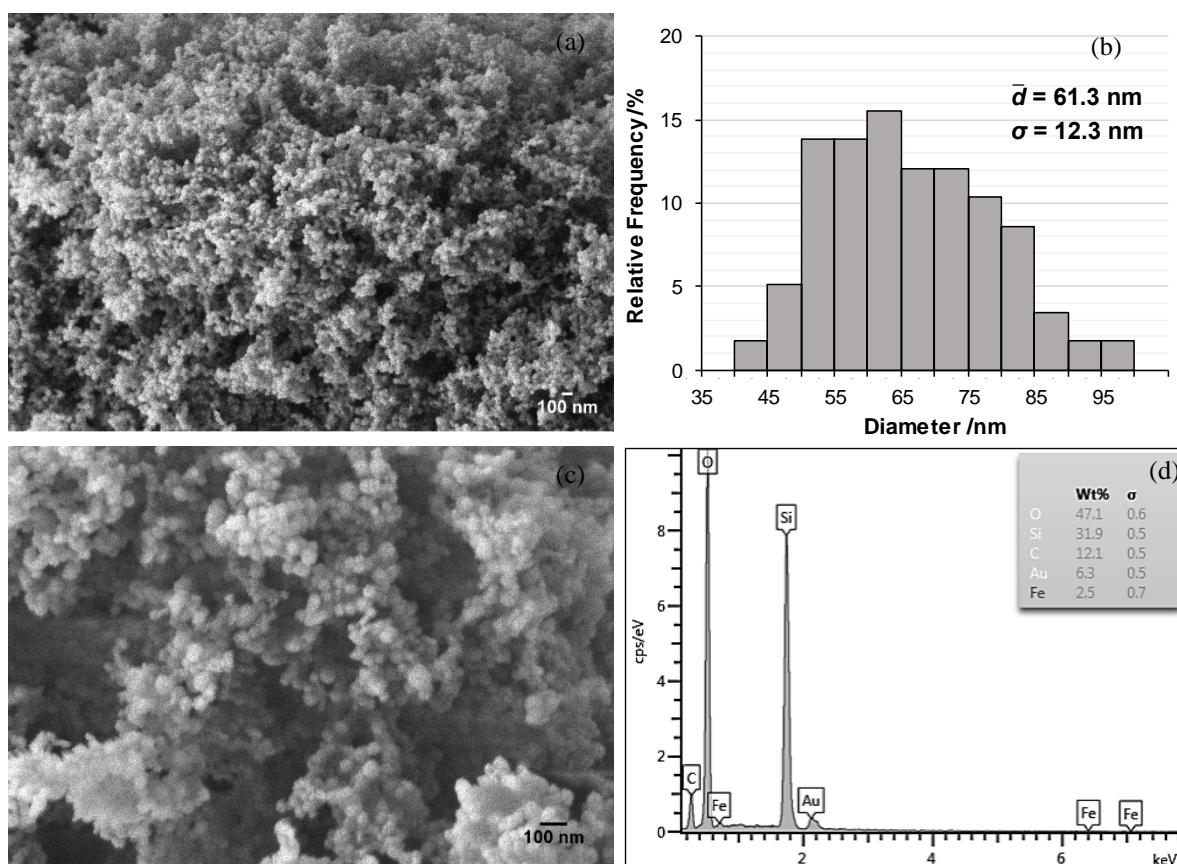


**Figure 30.** SEM images with magnetizations of (a) 20.00 kx and (c) 50.00 kx; (b) size distribution histogram ( $n=60$ ) and (d) EDS spectrum of the IO-OAm/mSiO<sub>2</sub>-SCD nanoparticles.

It is visible that the IO-OAm/mSiO<sub>2</sub> nanoparticles are smaller than 100 nm. This confirms the results obtained by DLS that showed that these nanoparticles had a smaller size than IO-OAm/mSiO<sub>2</sub>\* nanoparticles. The mean size of the IO-OAm/mSiO<sub>2</sub> nanoparticles obtained by SEM was  $61.3 \pm 12.3$  nm, which is comparable to the size obtained by Luong *et al.* (2016), where the final MMSNs had a mean size of 50 nm and whose procedure was followed to obtain the IO-OAm/mSiO<sub>2</sub> nanoparticles. Considering the size of the SPIONs and of the final nanoparticles, the silica shell can be estimated to have a thickness of  $\sim 26$  nm.

Furthermore, the size obtained by SEM of these nanoparticles is also smaller than the mean diameter obtained by DLS. However, it is only slightly smaller than the first intensity peak (90.7 nm), confirming that the information given by the intensity peaks of DLS was more useful as an early estimate of particle size than the mean diameter given by the software.

On the other hand, in the EDS spectrum, it can be confirmed that silicon, iron and oxygen exist in the sample. Oxygen and silicon were detected in higher quantity, which was expected given the silica shell. Gold was also detected in this analysis because of the sputter coating of the nanoparticles before the analysis. The small percentage of iron can be explained by its presence in smaller quantity. Finally, the quantity of carbon detected was also considerable, which can be related to the -OCH<sub>2</sub>CH<sub>3</sub> groups formed on the surface during SCD.

#### 4.1.2. Magnetic Characterization

The different nanoparticles in suspension were put in the presence of a magnet in order to observe their magnetic behaviour. Figure 31 presents images of suspensions of the IO-OAm/mSiO<sub>2</sub>\*- APD, IO-OAm/mSiO<sub>2</sub>\*- SCD and IO-OAm/mSiO<sub>2</sub>- SCD nanoparticles with and without the magnet.

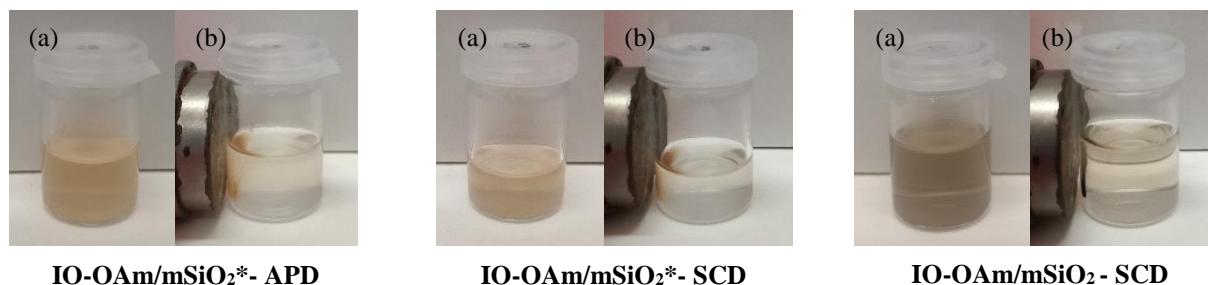


**Figure 31.** IO-OAm/mSiO<sub>2</sub>\* and IO-OAm/mSiO<sub>2</sub> nanoparticles (a) in the absence and (b) presence of a magnet.

As it can be observed, all the three types of nanoparticles exhibit magnetic behaviour, since the particles move towards the magnet and the suspensions clear in its presence.

#### Vibrating Sample Magnetometer

VSM was used to study the magnetic behaviour of both the SPIONs and the MMSNs, as well as determine their saturation magnetization.

In Figure 32, the magnetization curves at 1.8 K and at 300 K, which show the variation of the magnetic moment as a function of the magnetic field, are represented for the SPIONs produced by thermal decomposition. In the elaboration of these curves, the presence of oleylamine was accounted for, in order to obtain the magnetic moment in emu per g of iron oxide so that it could be compared with the magnetization of the SPIONs obtained by microemulsion. In Figure 33, the magnetization curves for the IO-OAm/mSiO<sub>2</sub> - SCD nanoparticles are also presented.

From the magnetization curves in Figure 32.(a) and in Figure 33.(a), it can be seen that the SPIONs synthesised by thermal decomposition have a saturation magnetization of 73.2 emu.g<sup>-1</sup> at 300 K, while for the IO-OAm/mSiO<sub>2</sub> -SCD nanoparticles the saturation magnetization is only 4.0 emu.g<sup>-1</sup> at the same temperature. This difference between the SPIONs and the final nanoparticles is very significant and it can be attributed to the mesoporous silica shell, which is present in large quantity around the iron oxide core, leading to a decrease on the saturation magnetization (Sodipo & Aziz, 2016). Additionally, partial oxidation of iron oxide might also occur, which also leads to lower saturation magnetization.

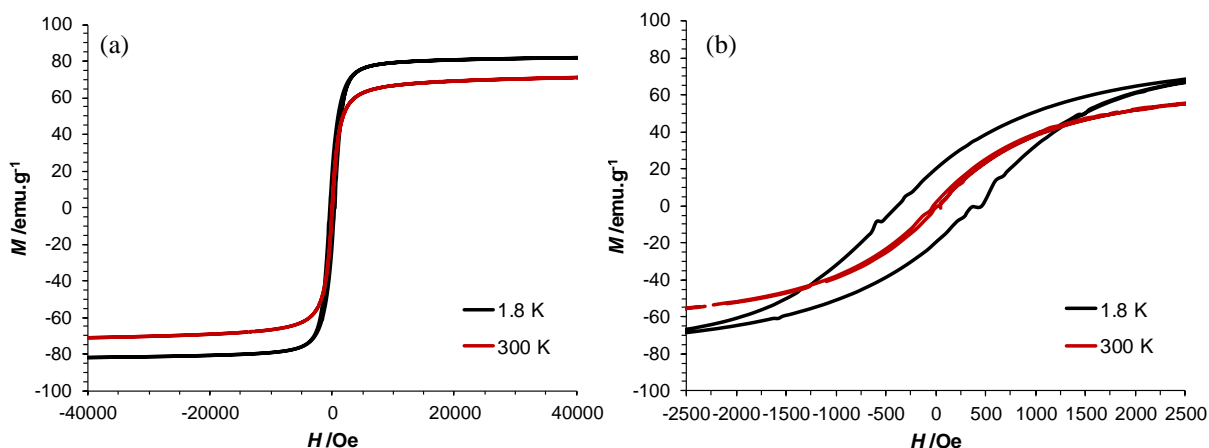


**Figure 32.** (a) Magnetization curves of the SPIONs produced by thermal decomposition and (b) detailed view around the origin of the plot.

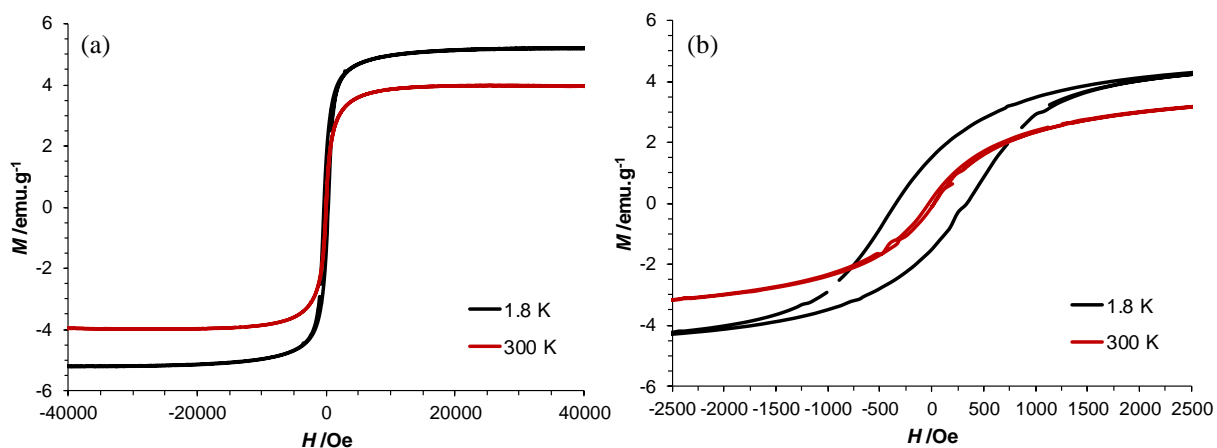


**Figure 33.** (a) Magnetization curves of the IO-OAm/mSiO<sub>2</sub>-SCD nanoparticles and (b) detailed view around the origin of the plot.

Since it was determined in TGA that the SPIONs are made of 80.1% of iron oxide and the remaining percentage corresponds to the organic coating of SPIONs, if this coating is considered, their saturation magnetization decreases from 73.2 to 58.7  $\text{emu.g}^{-1}$ , which is still much higher than the value obtained for the IO-OAm/mSiO<sub>2</sub>-SCD nanoparticles. However, the value obtained for these nanoparticles agrees with the value reported by Luong *et al.* (2016), which was 3.86  $\text{emu.g}^{-1}$  for MMSNs synthesised by a similar procedure.

With a decrease in temperature to 1.8 K, the saturation magnetization values are higher (83.2 and 5.2  $\text{emu.g}^{-1}$  for SPIONs and IO-OAm/mSiO<sub>2</sub>-SCD nanoparticles, respectively). However, the obtained value for IO-OAm/mSiO<sub>2</sub>-SCD nanoparticles is still very low in comparison to that of SPIONs.

Looking at the detailed curves in Figure 32.(b) and Figure 33.(b), it can be seen that both nanoparticles present hysteresis at 1.8 K. However, at 300 K, they have no hysteresis, therefore

having no coercivity and remanence, which is characteristic of superparamagnetic materials. Thus, this confirms that both the SPIONs obtained by thermal decomposition and the IO-OAm/mSiO<sub>2</sub>-SCD have superparamagnetic behaviour.

Given the similarity of the results, the analysis of the magnetization curves of the IO-OAm/mSiO<sub>2</sub>\*-APD and IO-OAm/mSiO<sub>2</sub>\*-SCD nanoparticles is presented in Appendix B. The obtained values of the saturation magnetization at 300 K for these nanoparticles (3.6 and 1.3 emu.g<sup>-1</sup> for IO-OAm/mSiO<sub>2</sub>\*-APD and IO-OAm/mSiO<sub>2</sub>\*-SCD, respectively) were both lower than for IO-OAm/mSiO<sub>2</sub>-SCD. This is a result of the higher amount of silica, confirmed by the higher average size for IO-OAm/mSiO<sub>2</sub>\*. Furthermore, the saturation magnetization of the nanoparticles dried by APD is higher than by SCD, indicating oxidation is more significant in supercritical drying.

In this analysis, the field cooled (FC) and zero-field cooled (ZFC) magnetization curves were also obtained with a magnetic field of 100 Oe. In these curves, magnetization is plotted as a function of temperature and they are represented in Figure 34 for the SPIONs and the IO-OAm/mSiO<sub>2</sub> nanoparticles.

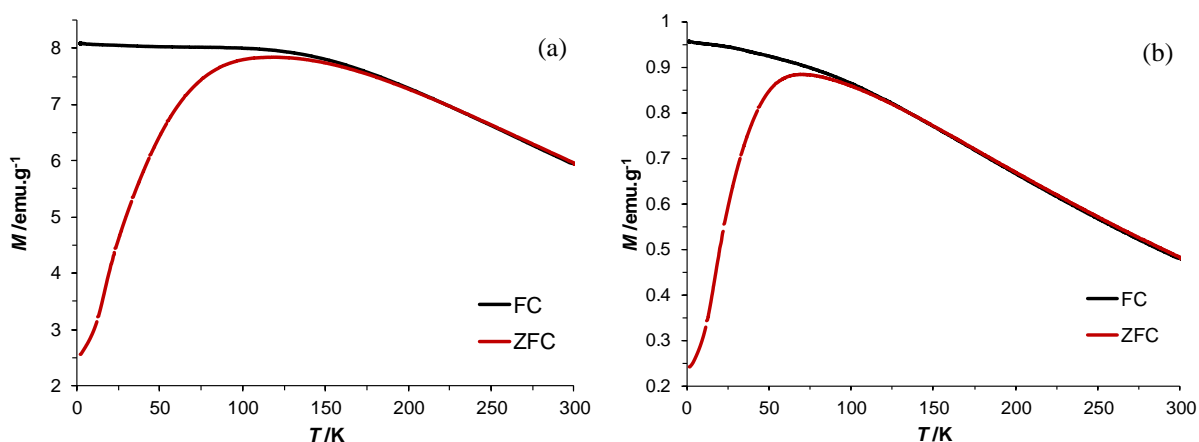


**Figure 34.** FC and ZFC curves obtained with a magnetic field of 100 Oe for (a) the SPIONs synthesised by thermal decomposition and (b) the IO-OAm/mSiO<sub>2</sub>-SCD nanoparticles.

The FC curves show that the magnetization of SPIONs is less dependent on temperature than in the case of IO-OAm/mSiO<sub>2</sub>-SCD nanoparticles.

The blocking temperature is the temperature below which the materials stop having a superparamagnetic behaviour and can be obtained from the ZFC curve, corresponding to the temperature at the maximum of this curve. Therefore, from Figure 34, the blocking temperature of SPIONs produced by thermal decomposition is ~110 K and of the IO-OAm/mSiO<sub>2</sub>-SCD nanoparticles is ~75 K.

For the intended application, the nanoparticles are used at a temperature much higher than their blocking temperature, assuring their superparamagnetic behaviour.

The FC and ZFC curves for the IO-OAm/mSiO<sub>2</sub>\* -APD and IO-OAm/mSiO<sub>2</sub>\* -SCD nanoparticles are also presented and discussed in Appendix B.

### Mössbauer Spectroscopy

In Figure 35, the Mössbauer spectra obtained for the oleylamine coated SPIONs and for the IO-OAm/mSiO<sub>2</sub> nanoparticles are presented.

The parameters of the fitting to the data points are not presented because the errors obtained were too high, particularly in the case of the IO-OAm/mSiO<sub>2</sub> -SCD nanoparticles, due to a high noise to signal ratio.

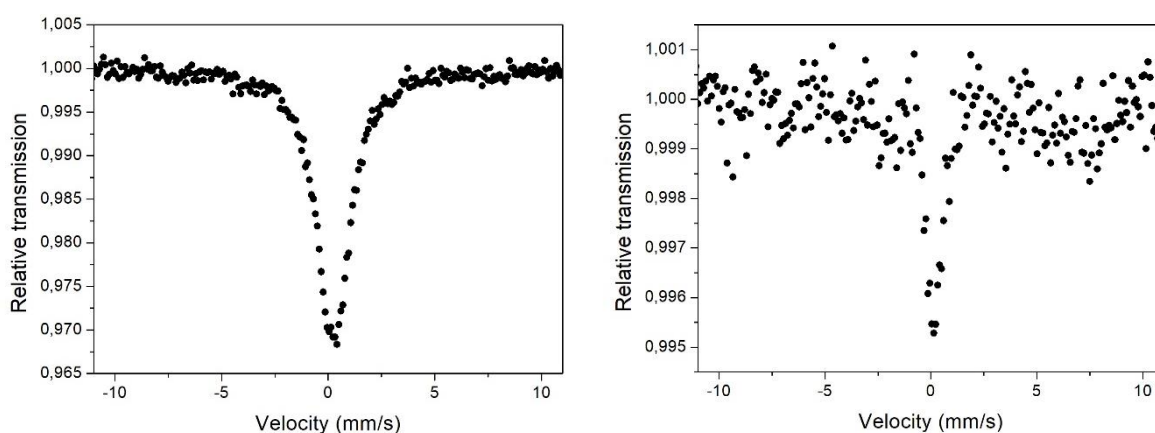


**Figure 35.** Mössbauer spectra for the oleylamine coated SPIONs (left) and for the IO-OAm/mSiO<sub>2</sub> - SCD nanoparticles (right).

In the spectrum of the oleylamine coated SPIONs, no sextets are observed. Furthermore, the existence of a broad peak, which could be both a singlet or a doublet, is characteristic of superparamagnetism and, thus, confirms the superparamagnetic behaviour of the SPIONs.

In the spectrum of the IO-OAm/mSiO<sub>2</sub> -SCD nanoparticles, the presence of magnetic phases can be observed, but it is not easy to distinguish between them. The spectrum, as well as the fitting to the data points, showed the existence of sextets, which can be attributed to those magnetic phases. The doublet that can also be observed is related to a superparamagnetic phase, confirming the superparamagnetic behaviour of these nanoparticles. This doublet has a percentage of about 80% of the spectrum, while magnetic phases occupy only about 20% of the spectrum.

The sextets were attributed to hematite, which has a very small saturation magnetization, and maghemite, indicating that the iron oxide cores suffered partial oxidation after they were synthesised. Therefore, this confirms that the decrease in the saturation magnetization observed in VSM was not only because of the high amount of silica in the nanoparticles, but also because oxidation occurred. Since hematite can be obtained from oxidation of magnetite and maghemite

at high temperatures (Cornell & Schwertmann, 2003), this might indicate that this phase was formed during supercritical drying, which explains the difference in saturation magnetization obtained in the VSM analysis of the IO-OAm/mSiO<sub>2</sub>\* -APD and IO-OAm/mSiO<sub>2</sub>\* -SCD nanoparticles.

The assignment of these sextets to maghemite and hematite was done by comparing the hyperfine parameters found in the literature for these phases with the hyperfine parameters found in the fitting procedure (for maghemite:  $H \approx 50$  T;  $QS \approx 0.02$  mm/s;  $IS \approx 0.5$  mm/s, and for hematite:  $H \approx 52$  T;  $QS \approx -0.2$  mm/s;  $IS \approx 0.4$  mm/s).

#### 4.1.3. Drug Loading

The loading of epirubicin into the IO-OAm/mSiO<sub>2</sub> - SCD nanoparticles was studied (from here on referred to as IO-OAm/mSiO<sub>2</sub>). The IO-OAm/mSiO<sub>2</sub>\* nanoparticles were not tested.

Two samples were loaded independently and are from here on referred to as loading A and loading B. In these experiments, the supernatants of the three centrifugations were collected. Posteriorly, 50  $\mu$ L aliquots were taken and diluted in water with a dilution factor of 20 and the UV-Vis quantification was done in triplicate.

In Figure 36, pictures of the nanoparticles dispersed in the drug solution and of the three supernatants of the centrifugations can be found. It was observed that almost all unloaded drug was in the first supernatant, with only residual epirubicin remaining after two washes. Furthermore, comparing the colour of the drug solution at the beginning of the loading experiment with the first supernatant, it is visible that the entrapment efficiency was very low, because the majority of the drug remained in solution.

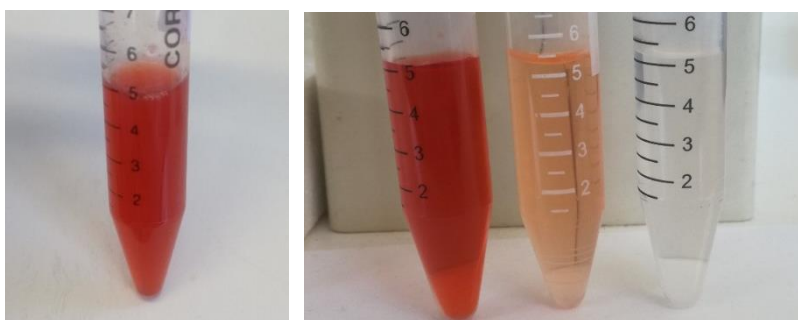


**Figure 36.** Picture of the nanoparticles dispersed in drug solution at the beginning of the loading experiment (left) and picture of the supernatants (right) from the first, second and third centrifugations, in the same order.

In order to determine the concentration of epirubicin after each centrifugation, a calibration curve was needed and a new calibration curve was made for each triplicate. The details of the determination of the calibration curve are presented next for one set of data, the

first quantification of loading A, with the other curves being calculated similarly and presented in Appendix C.

With the values of the concentration and final absorbance obtained, the calibration curve was obtained in Figure C.1 of Appendix C. Considering the Beer-Lambert law, given by equation (13), the trendline was forced to intercept the origin.

The calibration curve for this set of data is given by the following equation:

$$A = 0.0047C$$

with a  $R^2$  of 0.9995, indicating the fit was good and that the absorbance variation with concentration of epirubicin follows the Beer-Lambert law in the considered range.

With the calibration curve, the concentration could be determined. Knowing the concentration ( $C$ ) and that the aliquots had been diluted with a dilution factor of 20 and considering the volume of the supernatants ( $V$ ), the mass of epirubicin in each supernatant can be determined by the following equation:

$$m_{\text{EPI}} = 20.C.V \quad (14)$$

These results are presented in Table C.1 and Table C.2 of Appendix C for loading A and B, respectively.

Considering the initial mass of drug was 2500  $\mu\text{g}$  and the mass of nanoparticles in each loading experiment, the loading content and the entrapment efficiency can be determined using equations (5) and (6) presented before - Table 6.

**Table 6.** Loading content and entrapment efficiency for IO-OAm/mSiO<sub>2</sub> nanoparticles.

Loading	$m_{\text{NPs}}$ /mg	Quantification 1		Quantification 2		Quantification 3		Mean	
		LC (%)	EE (%)	LC (%)	EE (%)	LC (%)	EE (%)	LC (%)	EE (%)
A	5.02	2.97	5.96	3.27	6.58	3.05	6.13	3.10 ± 0.16	6.22 ± 0.32
B	4.98	2.66	5.31	3.22	6.41	3.18	6.34	3.02 ± 0.31	6.02 ± 0.62
<b>Mean</b>								3.06 ± 0.22	6.12 ± 0.45

As it can be seen in Table 6, the IO-OAm/mSiO<sub>2</sub> nanoparticles had a loading content of 3.08% (=30.8  $\mu\text{g}$  EPI/mg NPs), which is a very small percentage. However, this value agrees with those presented in Table 3 for doxorubicin: it is higher than the 15  $\mu\text{g}$  EPI/mg NPs obtained by Ronhovde *et al.* (2017) but lower than the 45.4  $\mu\text{g}$  EPI/mg NPs obtained by Tao & Zhu (2014). The entrapment efficiency is also very low, which is related to the high amount of drug initially present in order to load the nanoparticles. This quantity was chosen according to the literature and there was not enough time to test other loading conditions using less epirubicin, which would be important since the supernatants are not reused and, therefore, less drug would be wasted.

#### 4.1.4. Drug Release

For the release experiments, aliquots were taken at pre-established time points: 2, 4, 6, 22.5, 30 and 48 hours. During the early stages of the experiments, it was noticed that epirubicin suffered degradation with time in PBS at a pH of 7.4. In order to take this into account, the prepared solutions of EPI in PBS for the calibration curve were put in the shaking incubator during the experiment time and aliquots were taken at the same time points as for the drug loaded nanoparticles. Therefore, a calibration curve was obtained for each time point (Appendix D). The decrease in the slope of this curves confirms the degradation of epirubicin.

For the IO-OAm/mSiO<sub>2</sub> nanoparticles, three different samples of drug loaded nanoparticles were tested simultaneously.

The calibration curves were calculated similarly to the loading experiments and are presented in Appendix D. Knowing the concentration of released drug, it was possible to determine the percentage of released epirubicin from the nanoparticles.

The calculations of the mass at each time point had to take into account the loss of drug, in each aliquot. Therefore, in a time point  $t=i$ , the mass of epirubicin ( $m$ ) released can be determined by the following equation:

$$m_i = C_i V_i + \sum_{t=0}^{t=i-1} m_{\text{lost},t} \quad (15)$$

$$m_{\text{lost},t} = C_t V_{\text{lost},t} \quad (16)$$

where  $C$  is the concentration of epirubicin (determined from the absorbance with the calibration curve at each time point) and  $V$  is the volume of media in the vial.

Knowing the loading content and the mass of nanoparticles, the percentage of released epirubicin can be determined, through the following equation:

$$\text{EPI released (\%)} = \frac{m}{m_{\text{loaded NPs}} \cdot LC/100} \times 100 \quad (17)$$

The values related to these calculations can be found in Appendix D.

With the percentage of drug released from the three samples, the average values were calculated. The obtained profile and the standard deviation bars are represented in Figure 37.

In order to have more information of the release kinetics, this profile was also modelled. For that, the Korsmeyer-Peppas model was considered, which is given by equation (18):

$$\frac{M_t}{M_\infty} = kt^n \quad (18)$$

where  $M_t/M_\infty$  is the fraction of EPI released,  $t$  is the time,  $k$  is a release velocity constant and  $n$  is the exponent of release, dependent on the shape of the drug release system and on the drug release mechanism.



This model was chosen because it is commonly used in drug release and dissolution experiments and, furthermore, it has been used for the drug release in MMSNs (Daryasari *et al.*, 2016; Patel *et al.*, 2016; Ronhovde *et al.*, 2017; Souza *et al.*, 2009), allowing the comparison of the obtained parameters. The profile obtained with the Korsmeyer-Peppas model is also represented in Figure 37.

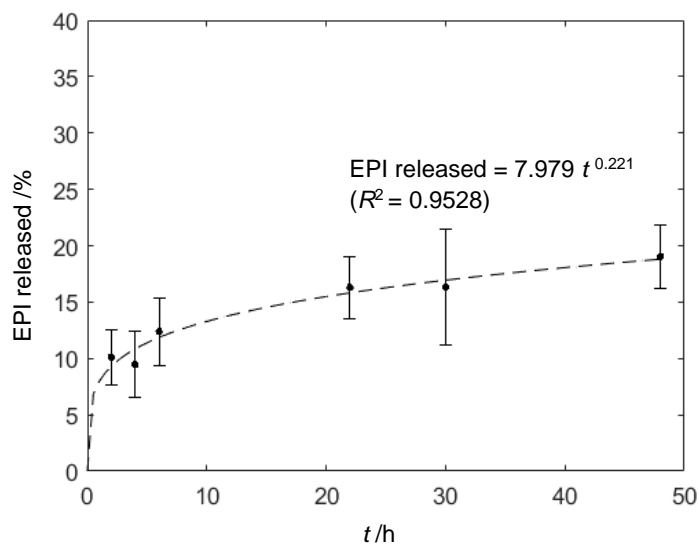


**Figure 37.** Release profile of epirubicin and correspondent Korsmeyer-Peppas model for the IO-OAm/mSiO<sub>2</sub> nanoparticles.

With the IO-OAm/mSiO<sub>2</sub> nanoparticles, 19.0±2.8% of epirubicin was released after 48 hours. This value was higher than those obtained for doxorubicin at the same pH. However, other experiments used smaller volumes for the same mass of loaded nanoparticles, which might lead to less favourable gradients of concentration for the release of drug. The Korsmeyer-Peppas parameters obtained were  $k=7.979$  and  $n=0.221$ , with a  $R^2$  of 0.9528, indicating this model can be used to describe the release kinetics of epirubicin from these nanoparticles.

For spherical particles,  $n=0.43$  indicates the drug release mechanism is Fickian diffusion; when  $0.43 < n < 1.00$  is non-Fickian diffusion occurs and  $n=1.00$  corresponds to a zero-order mechanism (Ritger & Peppas, 1987). The value obtained for the IO-OAm/mSiO<sub>2</sub> nanoparticles was much smaller than 0.43. However, this has been reported for nanoparticles: Ronhovde *et al.* (2017) and Souza *et al.* (2009) both obtained  $n$  values below 0.43 ( $n=0.20-0.384$  and  $n=0.25-0.32$ , respectively). This lowering of  $n$  can be explained by the agglomeration and dispersity of the nanoparticles. In the presence of polydisperse samples, there is an accelerated release at early time points due to the smaller particles and a retardation in release at later times because of the larger particles. These two effects combined led to the observed decrease in  $n$  (Ritger & Peppas, 1987; Ronhovde *et al.*, 2017), even when Fickian diffusion prevails.

## 4.2. IO-APTES/mSiO<sub>2</sub>

### 4.2.1. Synthesis Aspects and Chemical Characterization

For the synthesis of the IO-APTES/mSiO<sub>2</sub> nanoparticles, iron oxide was also obtained by thermal decomposition, followed by a ligand exchange procedure, in order to replace the oleylamine coating with APTES. After this stage, the SPIONs could be dispersed in water and were coated with the mesoporous silica shell, as mentioned in section 3.1.

Since it was confirmed with IO-OAm/mSiO<sub>2</sub>\* samples that SCD was the best drying option of the two, in terms of aggregation and porosity, only this type of drying was carried out for the IO-APTES/mSiO<sub>2</sub> nanoparticles. These nanoparticles, similarly to IO-OAm/mSiO<sub>2</sub>, exhibited a grey colour.

### Thermogravimetric Analysis

As discussed in section 4.1.1., the SPIONs produced by thermal decomposition had 80.1% of iron oxide and the remaining percentage of weight was attributed to the oleylamine coating. TGA was also used with IO-APTES nanoparticles, in order to confirm the success of the ligand exchange. The obtained thermogram is presented in Figure 38.

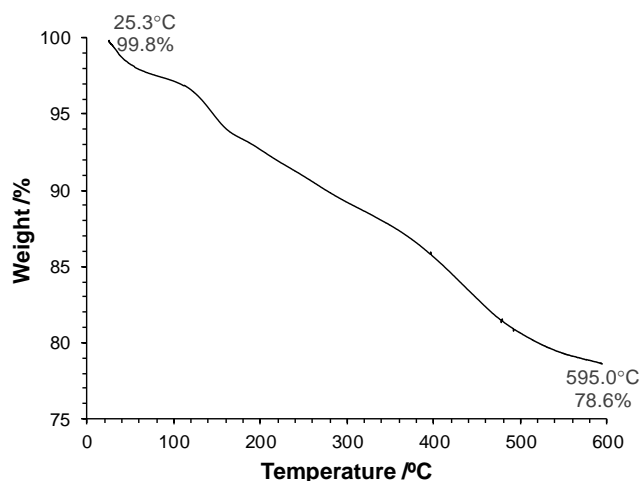


Figure 38. Thermogram of the APTES-coated SPIONs.

The weight loss profile presented in Figure 38 is different from the one presented in Figure 24 for oleylamine-coated SPIONs. There is an initial weight loss, until 130°C, which can be attributed to the evaporation of water from the surface of the nanoparticles, due to the hydrophilicity of the APTES-coated SPIONs (Pershina *et al.*, 2016). The decrease in weight above that temperature corresponds to thermal degradation, first, of the amino group and then of the organic chain of APTES (Durdureanu-Angheluta *et al.*, 2012). Furthermore, there is the

possibility that not all oleylamine molecules were replaced with APTES and these are also decomposed, particularly above 300°C.

The total weight loss was 21.2%, with the other 78.6% corresponding to iron oxide and silica.

### Fourier-Transform Infrared Spectroscopy

In Figure 39, the spectra for the iron oxide nanoparticles before and after the ligand exchange procedure are presented, as well as of the IO-APTES/mSiO<sub>2</sub> nanoparticles.

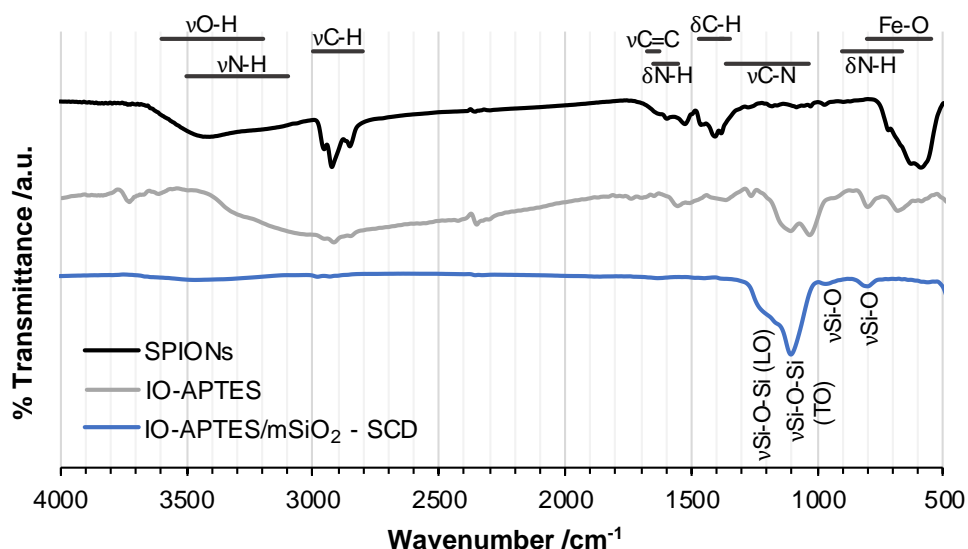


**Figure 39.** FTIR spectra obtained for SPIONs produced by thermal decomposition, for SPIONs after ligand exchange and for the final magnetic MSNs dried by SCD. (v – stretching,  $\delta$  – bending.)

Comparing the spectra of the SPIONs before and after ligand exchange, it is visible that the reaction was successful, given the presence of the bands characteristic of silica. These appear at  $\sim 1025\text{ cm}^{-1}$  and  $\sim 1100\text{ cm}^{-1}$ , corresponding to the asymmetric stretching modes of Si-O-Si and at  $\sim 915\text{ cm}^{-1}$ , corresponding to the Si-O in-plane stretch. Furthermore, the spectrum obtained for IO-APTES was similar to those found in literature for ligand exchange with APTES (Davis *et al.*, 2016).

In the spectrum of IO-APTES, the presence of iron oxide is confirmed by the bands in the region between  $550$  and  $700\text{ cm}^{-1}$ . On the other hand, the peak at  $\sim 3700\text{ cm}^{-1}$  corresponds to the stretching vibration of free OH, which along with the presence of a small peak at  $\sim 1630\text{ cm}^{-1}$ , can be related to the presence of water in the sample. There is also a broad band at around  $3300\text{ cm}^{-1}$ , as well as reduction in the baseline, which can be attributed to the stretching mode of N-H of the amino group. The bending modes of the N-H bond can be found at  $1550\text{ cm}^{-1}$  and at  $800\text{ cm}^{-1}$ ; the bands between  $2800$  and  $3000\text{ cm}^{-1}$  and between  $1350$  and  $1450\text{ cm}^{-1}$  are related

to the C-H stretching and bending, respectively, of the aminopropyl chain of APTES, as well as of the remaining oleylamine. Finally, the band at around 1260 cm<sup>-1</sup> can be related to the vibration mode of Si-C, which may overlap with the C-N vibration.

The spectrum obtained for IO-APTES/mSiO<sub>2</sub> nanoparticles is very similar to the one obtained for IO-OAm/mSiO<sub>2</sub> nanoparticles (Figure 25). Once again three bands of silica can be found at ~1200, ~1100 and ~970 cm<sup>-1</sup>. There is also a band at around 800 cm<sup>-1</sup>, which can be attributed to the Si-O symmetric stretching of the ≡Si-O-Si≡ bond and may overlap with the N-H bending mode of the amino group of APTES or residual oleylamine. The other bands related to the C-H, N-H and C-N vibration modes of these compounds, as well as the bands for Fe-O, cannot be found in the spectrum, which is probably due to the intensity of the bands of silica that fade the visualization of smaller peaks.

### Dynamic Light Scattering and Zeta Potential

In Table 7, the results of the DLS measurements for the IO-APTES/mSiO<sub>2</sub> nanoparticles are presented.

**Table 7.** DLS results for the IO-APTES/mSiO<sub>2</sub>.

Replicate	Intensity Peaks									PDI	$\bar{d}$ /nm
	Peak /nm	St. Dv. /nm	Area (%)	Peak /nm	St. Dv. /nm	Area (%)	Peak /nm	St. Dv. /nm	Area (%)		
1	82.44	22.78	18.7	376.4	172.2	77.8	5269	428.9	3.5	0.566	246.3
2	103.2	32.7	25.1	513.1	262.7	70.5	4802	726.2	4.4	0.480	262.0
3	90.22	28.18	21.7	396.0	168.7	76.1	5459	257.3	2.3	0.589	277.2
<b>Mean</b>	92.0	27.9		428.5	201.2		5177	470.8		0.545	261.8

These nanoparticles have three distinct intensity peaks, with the one around 5000 nm corresponding to aggregates of nanoparticles. The mean size of the nanoparticles is 261.8 nm, which is between the two other intensity peaks. Considering the area of each peak, it is notorious that the peak around 92.0 nm has less intensity than the one around 428.5 nm. However, as it was mentioned for the IO-OAm/mSiO<sub>2</sub> nanoparticles, this does not mean that there are more particles with a size near 428.5 nm, but only that they scatter more light because they are bigger. Therefore, it is only possible to know that there are nanoparticles with a mean size of 92.0 nm and others with a mean size of 428.5 nm.

The zeta potential of the IO-APTES/mSiO<sub>2</sub> nanoparticles was also evaluated and its results are presented in Table 8. These nanoparticles have a zeta potential of -26.3 mV, which indicates once again that the removal of surfactant was successful.

**Table 8.** Zeta potential of IO-APTES/mSiO<sub>2</sub>.

Replicate	Zeta Potential /mV	St. Dv. /mV
1	-26.5	7.5
2	-22.1	6.7
3	-30.3	7.4
Mean	-26.3	7.2

### Transmission Electron Microscopy

In Figure 40, an image obtained by TEM of the IO-APTES/mSiO<sub>2</sub>, as well as the histogram of the size distribution resulting from this analysis are presented.

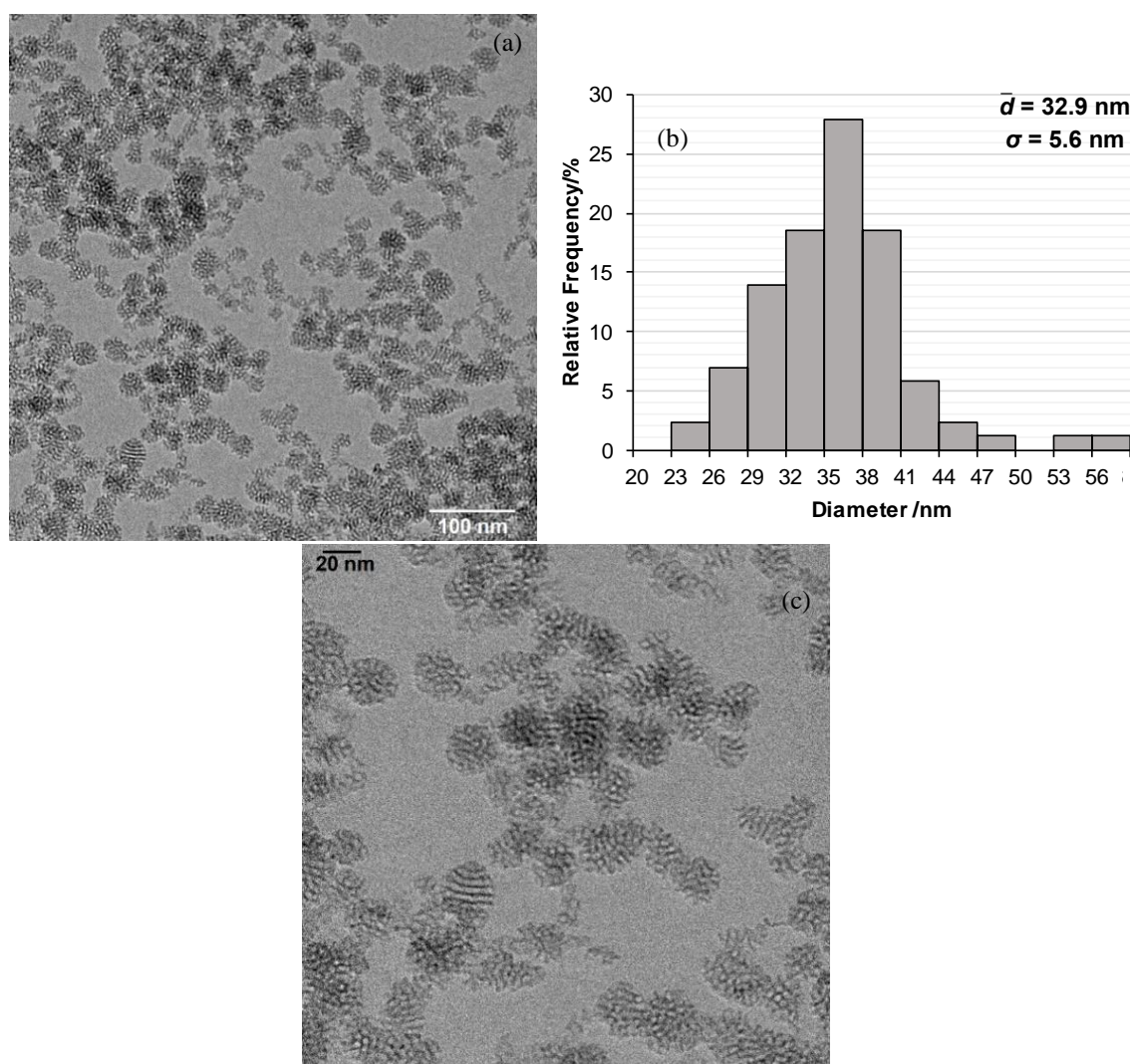


**Figure 40.** TEM images (a, c) and histogram (b) of the size distribution (n=85) for the IO-APTES/mSiO<sub>2</sub> nanoparticles.

Analysing the nanoparticles shown in Figure 40, it is visible they are much smaller than 100 nm, leading to a mean diameter of  $32.9 \pm 5.6 \text{ nm}$ . These nanoparticles are also more monodisperse in size and have a regular spherical shape. Furthermore, they appear to aggregate less than the IO-OAm/mSiO<sub>2</sub> nanoparticles. This could be a result of the presence of the

Synthesis of superparamagnetic mesoporous silica nanoparticles to mediate antitumour strategies

aminopropyl spacer in the SPIONs, which could limit the condensation of TEOS. Comparing the mean diameter obtained by TEM to the DLS results, the nanoparticles are much smaller than they appeared on the DLS analysis.

In Figure 40.(a), the porosity of the nanoparticles can also be seen. Additionally, an image of the particles with higher resolution is presented in Figure 40.(c). These nanoparticles present similar structures to those found in literature for non-magnetic mesoporous silica nanoparticles (Nandiyanto *et al.*, 2009), assuring that the porosity seen in the images is not just an effect of the magnetism of the nanoparticles.

### Scanning Electron Microscopy coupled with Energy Dispersive X-Ray Spectroscopy

Figure 41 shows an image obtained in SEM of the IO-APTES/mSiO<sub>2</sub> nanoparticles, as well as the EDS spectrum obtained in the same equipment.

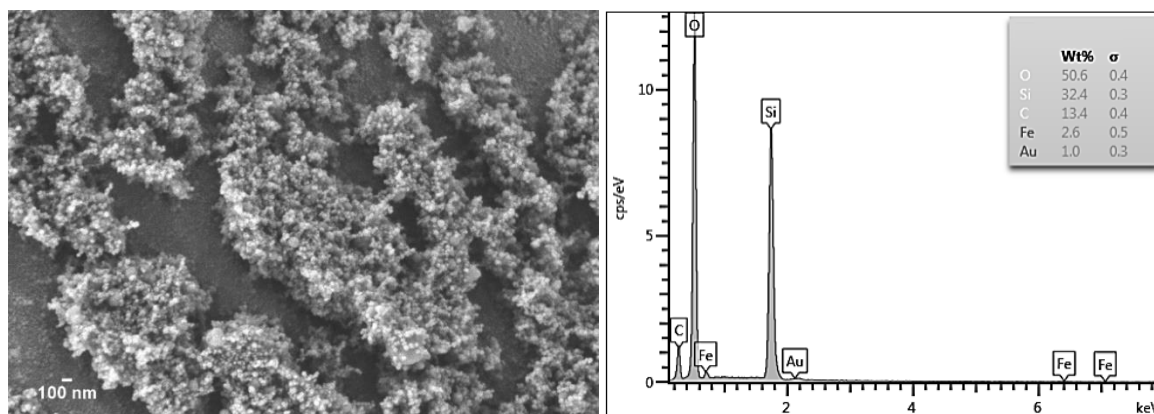


**Figure 41.** SEM image and EDS spectrum of the IO-APTES/mSiO<sub>2</sub> nanoparticles.

As seen by TEM, in Figure 41, the particles appear much smaller than 100 nm. The EDS spectrum confirms the presence of iron. As already referred for the IO-OAm/mSiO<sub>2</sub> samples, the presence of gold is due to the sputter coating on the nanoparticles and the high quantity of silicon and oxygen is expected due to the silica phase and silanol groups on the surface. Moreover, the presence of carbon can be an indication of the presence of -OCH<sub>2</sub>CH<sub>3</sub> on the surface.

#### 4.2.2. Magnetic Characterization

The IO-APTES/mSiO<sub>2</sub> nanoparticles were also observed in presence of a magnet, which can be found in Figure 42.

As it can be observed, these nanoparticles present magnetic behaviour, since they move towards the magnet in its presence.

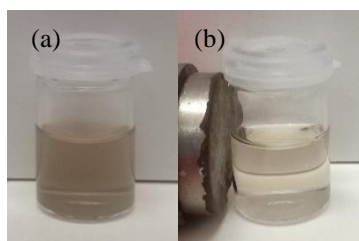


**Figure 42.** IO-APTES/mSiO<sub>2</sub> nanoparticles (a) in the absence and (b) presence of a magnet.

### Vibrating Sample Magnetometer

The magnetization curves for the IO-APTES/mSiO<sub>2</sub> nanoparticles are presented in Figure 43. The curves obtained for the IO-APTES/mSiO<sub>2</sub> nanoparticles show low saturation magnetization: 1.8 emu.g<sup>-1</sup> at 300 K and 2.3 emu.g<sup>-1</sup> at 1.8 K. This small value of saturation magnetization might be an indication that after the ligand exchange procedure the SPIONs can suffer oxidation and, thus, become less magnetic. In Figure 43.(b), it can be seen that these nanoparticles present hysteresis at 1.8 K but at 300 K there is almost no hysteresis and, thus, the IO-APTES/mSiO<sub>2</sub> nanoparticles are superparamagnetic.

The FC and ZFC curves were also plotted and are presented in Figure 44.

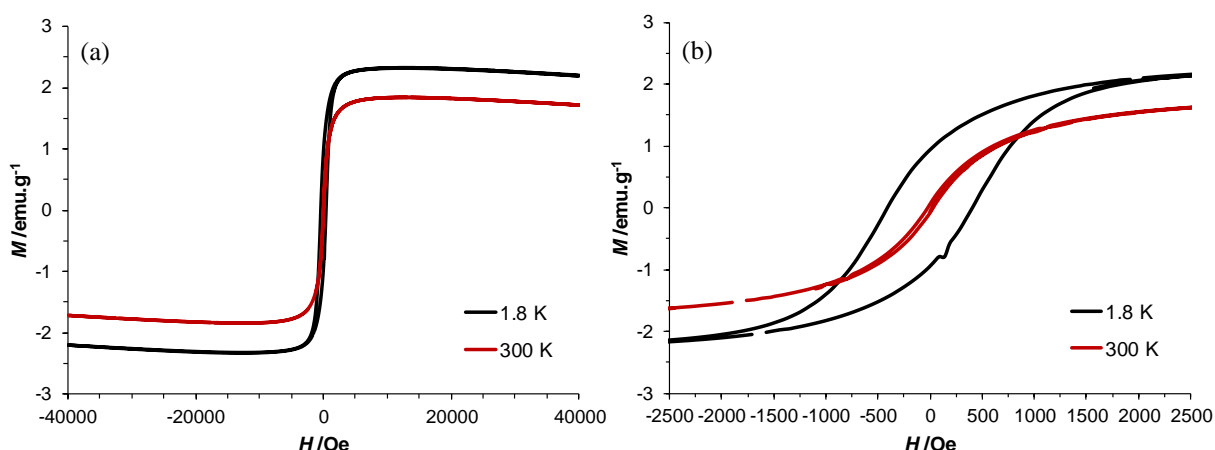


**Figure 43.** (a) Magnetization curves of the IO-APTES/mSiO<sub>2</sub> nanoparticles and (b) detailed view around the origin of the plot.

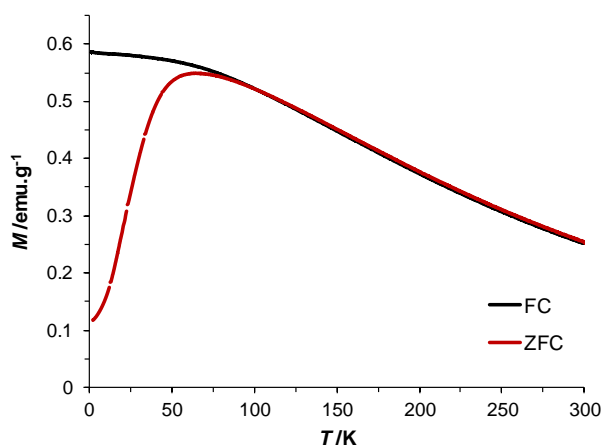


**Figure 44.** FC and ZFC curves obtained with a magnetic field of 100 Oe for the IO-APTES/mSiO<sub>2</sub> nanoparticles.

The blocking temperature of these nanoparticles is  $\sim 65$  K, which means they do not exhibit superparamagnetic behaviour below this temperature.

### Mössbauer Spectroscopy

In Figure 45, the Mössbauer spectrum obtained for the IO-APTES/mSiO<sub>2</sub> nanoparticles is presented. The spectrum obtained for the IO-APTES/mSiO<sub>2</sub> nanoparticles shows, similarly to the IO-OAm/mSiO<sub>2</sub> nanoparticles, the presence of sextets attributed to the magnetic phases, which occupy about 20% of the spectrum. In addition, a doublet, with a percentage of about 80% of the spectrum, is observed and confirms the superparamagnetism of the particles.

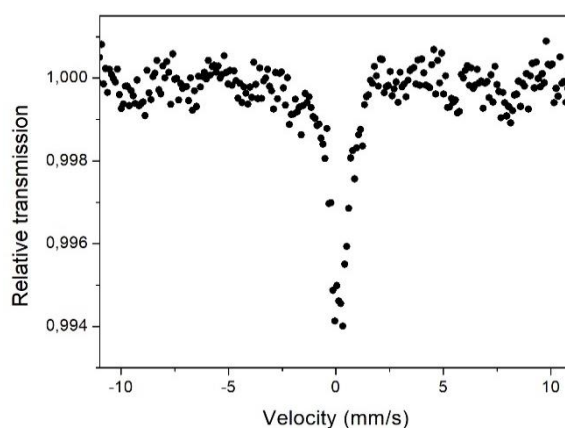


**Figure 45.** Mössbauer spectrum for the IO-APTES/mSiO<sub>2</sub> nanoparticles.

The sextets were also assigned to maghemite and hematite, indicating once more that partial oxidation of iron oxide occurred. This corroborates what had already been hypothesised considering the very low saturation magnetization obtained in VSM.

### 4.2.3. Drug Loading

The IO-APTES/mSiO<sub>2</sub> nanoparticles were also tested in the loading of epirubicin. The procedures as well as the calculations were similar to the ones presented for IO-OAm/mSiO<sub>2</sub> nanoparticles. Two different loadings (A and B) were also made and each of them was also quantified three times. The obtained values of absorbance, concentration and mass of drug are presented in Table C.3 and Table C.4 of Appendix C.

The loading content and entrapment efficiency are presented in Table 9.

According to Table 9., the loading content for the IO-APTES/mSiO<sub>2</sub> nanoparticles was 3.31%. However, it is noticeable that loading content in loading A was higher than in loading B. This is related to the fact that interaction between the nanoparticles and the drug is complex and can be affected by different parameters, such as the aggregation of the particles. The loading content values are once more in accordance with those presented for doxorubicin in Table 3.



**Table 9.** Loading content and entrapment efficiency for IO-APTES/mSiO<sub>2</sub> nanoparticles.

Loading	$m_{NPs}$ /mg	Quantification 1		Quantification 2		Quantification 3		Mean	
		LC (%)	EE (%)	LC (%)	EE (%)	LC (%)	EE (%)	LC (%)	EE (%)
A	4.98	3.71	7.40	4.80	9.56	3.19	6.36	3.90 ± 0.82	7.77 ± 1.63
B	4.97	2.76	5.48	3.12	6.21	2.29	4.56	2.72 ± 0.42	5.42 ± 0.83
<b>Mean</b>								3.31 ± 0.87	6.60 ± 1.73

#### 4.2.4. Drug Release

The epirubicin release from the IO-APTES/mSiO<sub>2</sub> nanoparticles was also studied with three different samples of nanoparticles. The calculations necessary to obtain the percentage of released epirubicin, in weight, were described for the IO-OAm/mSiO<sub>2</sub> nanoparticles.

The mean profile, as well as the standard deviation bars and the profile obtained with the Korsmeyer-Peppas model, are presented in Figure 46.

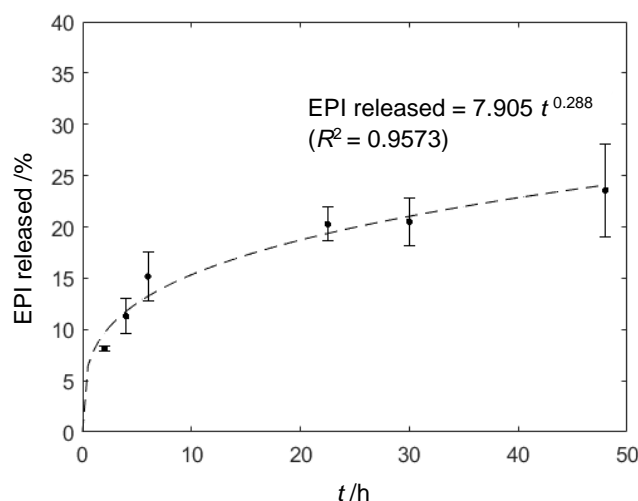


**Figure 46.** Release profile of epirubicin and correspondent Korsmeyer-Peppas model for the IO-APTES/mSiO<sub>2</sub> nanoparticles.

The release experiments in the IO-APTES/mSiO<sub>2</sub> nanoparticles led to a release of 23.6±4.5% of epirubicin after 48 hours. Looking at the release profile, it can be seen that the majority of the drug release happened in the first 6 hours of the experiment and not much more was released after the first 24 hours, where 20% had already been reached. The fitting of the Korsmeyer-Peppas model led to a  $R^2$  of 0.9573, confirming the usefulness of this model. The parameters obtained were  $k=7.905$  and  $n=0.288$ , indicating that the release kinetics mechanism was Fickian diffusin. Similarly to the IO-OAm/mSiO<sub>2</sub> nanoparticles,  $n$  was smaller than 0.43, which is characteristic of drug release from nanoparticles (Ronhovde *et al.*, 2017).

### 4.3. IO/SiO<sub>2</sub>/mSiO<sub>2</sub>

#### 4.3.1. Synthesis Aspects and Chemical Characterization

To obtain the IO/SiO<sub>2</sub>/mSiO<sub>2</sub> particles, iron oxide was synthesised by microemulsion. Afterwards, to protect the SPIONs from oxidation, they were first coated with non-porous silica and only after with a mesoporous silica shell, in order to obtain the final MMSNs. The drying process used for these nanoparticles was SCD.

Unlike the other MMSNs synthesised, IO/SiO<sub>2</sub>/mSiO<sub>2</sub> particles dried by SCD had a dark brown colour.

#### Fourier-Transform Infrared Spectroscopy

In Figure 47, the FTIR spectra obtained for SPIONs produced by microemulsion and for the final MMSNs are presented.

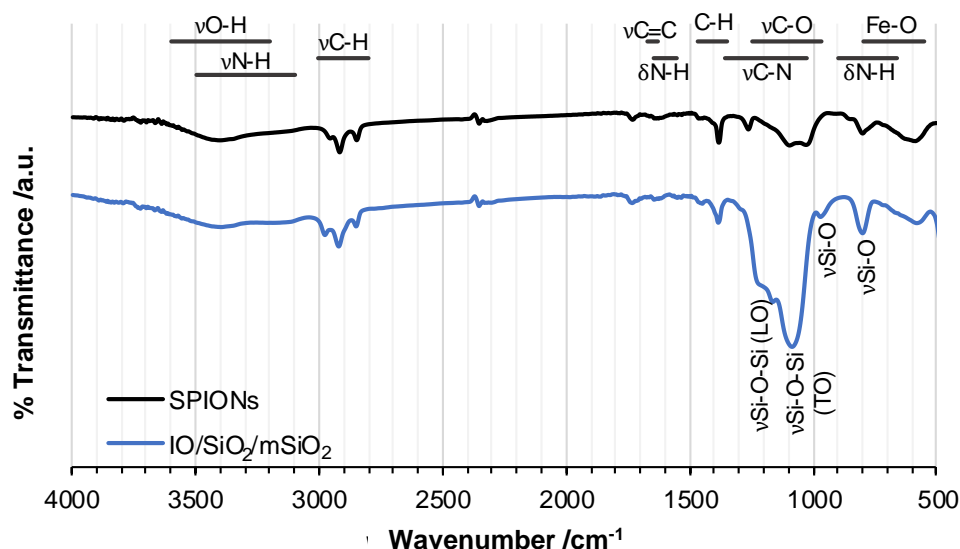


**Figure 47.** FTIR spectra of the SPIONs obtained by microemulsion and of the final magnetic MSNs dried by SCD. ( $\nu$  – stretching,  $\delta$  – bending.)

In the spectrum of SPIONs, the two important bands are the one at  $\sim 600\text{ cm}^{-1}$ , attributed to the Fe-O bond, and the one at  $3400\text{ cm}^{-1}$ , related to the stretching vibration of OH, since this group is present at the surface of the iron oxide nanoparticles. The other bands that appear on the spectrum are related to the residual presence of other organic compounds used in the synthesis.

Because of the OH groups on the surface of the nanoparticles, there is a strong interaction between them and ethanol, which is used to wash the SPIONs, and thus, it is difficult to completely remove this compound (Campos-Gonçalves *et al.*, 2017). Therefore, the band at

$\sim 1020\text{ cm}^{-1}$ , related to the stretching of C-O, as well as the bands between  $2800$  and  $3000\text{ cm}^{-1}$  and between  $1350$  and  $1500\text{ cm}^{-1}$ , which correspond to C-H stretching and bending vibrations, respectively, can be attributed to the presence of residual ethanol. On the other hand, the band near  $1260\text{ cm}^{-1}$ , in the region of the stretching of the C-N bond, indicates the presence of CTAB, suggesting that it was not completely removed during the washing step. Additionally, the presence of N-H vibration modes at  $\sim 1625\text{ cm}^{-1}$  and at  $\sim 800\text{ cm}^{-1}$ , as well as at  $\sim 3400\text{ cm}^{-1}$ , can also be attributed to presence of residual ammonium hydroxide.

In the spectrum of IO/SiO<sub>2</sub>/mSiO<sub>2</sub>, the presence of silica is clearly confirmed by the bands at  $\sim 1100\text{ cm}^{-1}$  and  $\sim 1175\text{ cm}^{-1}$ , related to the Si-O-Si asymmetric stretching modes; the band at  $\sim 975\text{ cm}^{-1}$ , corresponding to the in-plane stretching of the Si-O bond and the band at around  $800\text{ cm}^{-1}$  that can be related to the symmetric Si-O stretching vibration of the Si-O-Si bond. The band near  $570\text{ cm}^{-1}$  also confirms the presence of iron oxide in the nanoparticles. Moreover, the bands in the region of C-H stretching and bending suggest the presence of organic groups, which can be attributed to the -OCH<sub>2</sub>CH<sub>3</sub> groups formed during SCD or to residual CTAB. The bands at  $\sim 1650\text{ cm}^{-1}$  and at  $\sim 800\text{ cm}^{-1}$ , that can be related to the N-H bending, suggest the presence of residual ammonium hydroxide.

The band at  $\sim 1720\text{ cm}^{-1}$ , present in both spectra, is related to the stretching mode of the C=O vibration. Since no compounds with this bond were used in the synthesis, it can only be related to a contamination during the FTIR sample preparation, particularly during the drying step, probably of a carboxylic acid.

### Dynamic Light Scattering and Zeta Potential

The results obtained in the DLS measurements for the IO/SiO<sub>2</sub>/mSiO<sub>2</sub> particles are presented in Table 10.

As it can be seen in Table 10, the PDI for these particles is very high, indicating they are very polydisperse. This led to a mean diameter calculated by the software above  $2000\text{ nm}$ .

The IO/SiO<sub>2</sub>/mSiO<sub>2</sub> particles only presented one intensity peak, at around  $692.0\text{ nm}$ , indicating that the size of the particles might be around this value.

**Table 10.** DLS results for the IO/SiO<sub>2</sub>/mSiO<sub>2</sub>.

Replicate	Intensity Peaks			PDI	$\bar{d}$ /nm
	Peak /nm	St. Dv. /nm	Area (%)		
1	488.7	39.4	100	1.00	2388
2	725.3	99.5	100	0.765	1959
3	861.9	138.3	100	0.723	1920
<b>Mean</b>	692.0	92.4		0.829	2089

In terms of zeta potential, the results obtained can be found in Table 11.

**Table 11.** Zeta potential of IO/SiO<sub>2</sub>/mSiO<sub>2</sub>.

Replicate	Zeta Potential /mV	St. Dv. /mV
1	-30.3	3.4
2	-31.4	3.6
3	-30.9	4.7
<b>Mean</b>	-30.9	3.9

These nanoparticles have a zeta potential of -30.9 mV, which confirms that the removal of CTAB was successful. Furthermore, since the zeta potential is more negative than -30 mV, they form stable solutions in water.

### Transmission Electron Microscopy

In Figure 48, an image obtained by TEM of the IO/SiO<sub>2</sub>/mSiO<sub>2</sub> particles and the histogram of the size distribution obtained from this analysis are presented.

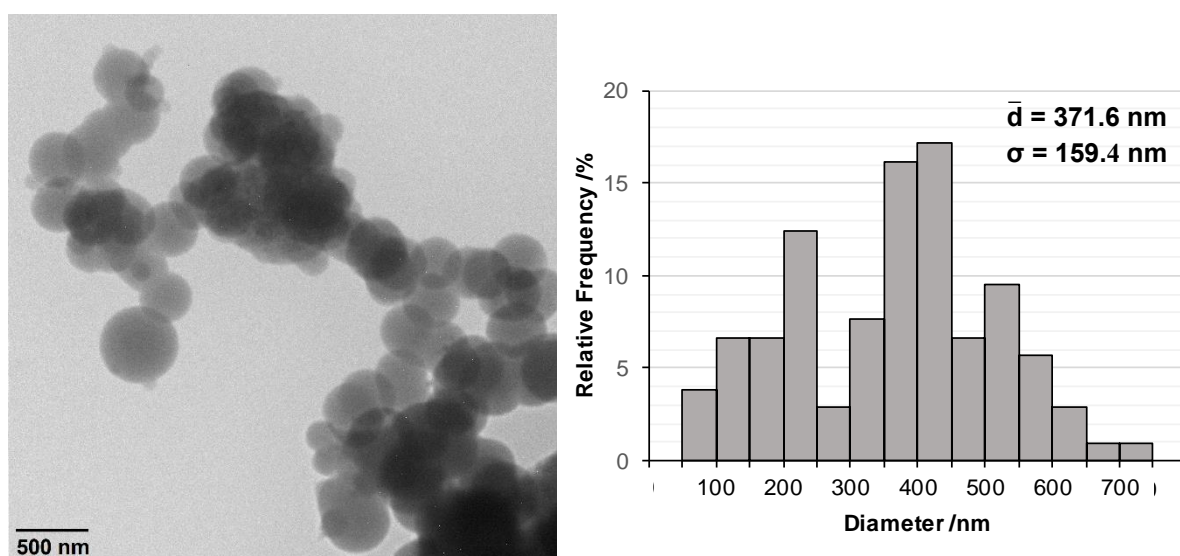


**Figure 48.** TEM image and histogram of the size distribution (n=105) for the IO/SiO<sub>2</sub>/mSiO<sub>2</sub> particles.

The IO/SiO<sub>2</sub>/mSiO<sub>2</sub> particles have a very regular round shape, with a mean size of 371.6±159.4 nm. The high standard deviation is an indication of the high polydispersity of these particles, confirming the high PDI values obtained in the DLS measurements. Similarly to the other synthesised nanoparticles, the size obtained by microscopy is much smaller than the one obtained by DLS, indicating once more that DLS is not adequate to characterize these particles.

The SPIONs synthesised by microemulsion were not characterized by TEM, but according to the literature they are expected to have a size around 9 nm (Maleki *et al.*, 2012).

In Figure 49, two other images of IO/SiO<sub>2</sub>/mSiO<sub>2</sub> obtained by TEM are presented in order to see them in more detail.

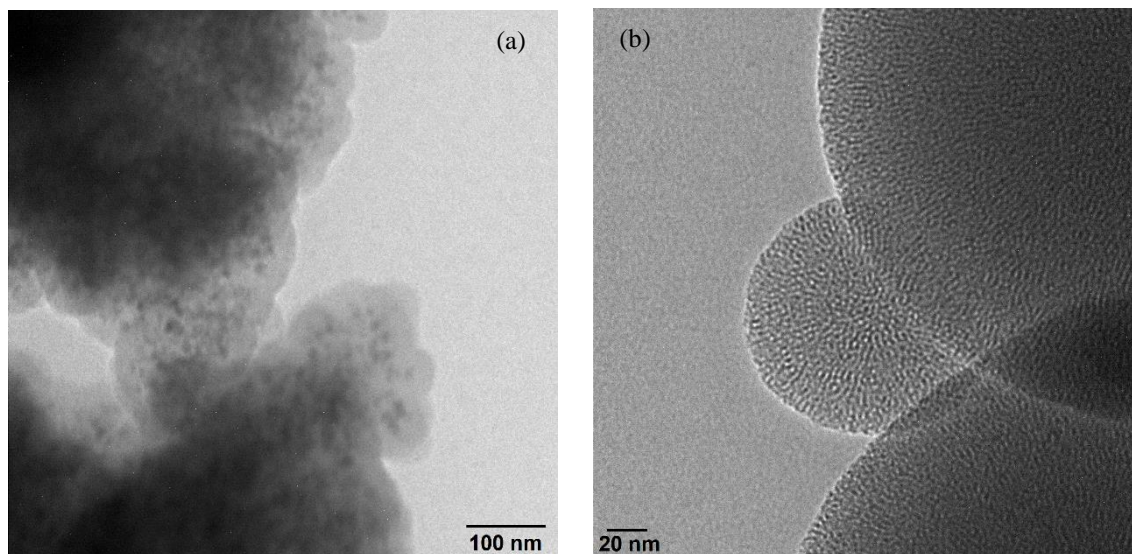


**Figure 49.** TEM images of the IO/SiO<sub>2</sub>/mSiO<sub>2</sub> nanoparticles, showing (a) the core nanoparticles and (b) the porosity.

In Figure 49.(a), small dark dots can be seen inside the silica particles and, using *Image J*, it was found that their size was around ~10 nm. Therefore, these could be the iron oxide nanoparticles inside the MMSNs, showing that, instead of having only one core particle, these are heterogeneous with multiple SPIONs inside one particle. This increased presence of iron oxide in the nanoparticles could explain why they have a dark brown colour instead of grey, like in the case of IO-OAm/mSiO<sub>2</sub> and IO-APTES/mSiO<sub>2</sub> nanoparticles. Figure 49.(b) shows the porosity of these nanoparticles, with light holes can be seen in them, corresponding to the mesopores.

#### **Scanning Electron Microscopy coupled with Energy Dispersive X-Ray Spectroscopy**

In Figure 50, a SEM micrograph of IO/SiO<sub>2</sub>/mSiO<sub>2</sub>, as well as the EDS spectrum of the IO/SiO<sub>2</sub>/mSiO<sub>2</sub> nanoparticles are shown.

Looking at the SEM micrograph, the particles appear much smaller than the average diameter obtained by TEM. However, in TEM, smaller particles could also be seen but they were present in less number. The existence of these smaller particles observed in the SEM image, contrasting with the larger particles found in the TEM image, is another evidence of the wide dispersity of the particles' size.

In the EDS spectrum, like for the other nanoparticles, the presence of iron, silicon and oxygen is confirmed. There is also a peak corresponding to carbon, even though this element

Synthesis of superparamagnetic mesoporous silica nanoparticles to mediate antitumour strategies

was not accounted for in the weight percentages calculated by the software. As said before, the presence of gold is related to the sputter coating of the nanoparticles during sample preparation. Furthermore, iron is present in 6.3% in weight, while in the other nanoparticles this value was around 2-3%. Since the IO/SiO<sub>2</sub>/mSiO<sub>2</sub> particles are much bigger than those of IO-OAm/mSiO<sub>2</sub> and IO-APTES/mSiO<sub>2</sub>, it was expected that, if only one iron oxide core existed, the amount of iron detected in EDS would be smaller. Therefore, this increase might corroborate the hypothesis that there are multiple iron oxide cores inside one IO/SiO<sub>2</sub>/mSiO<sub>2</sub> particle and, thus, more iron can be accounted for in the EDS reading.

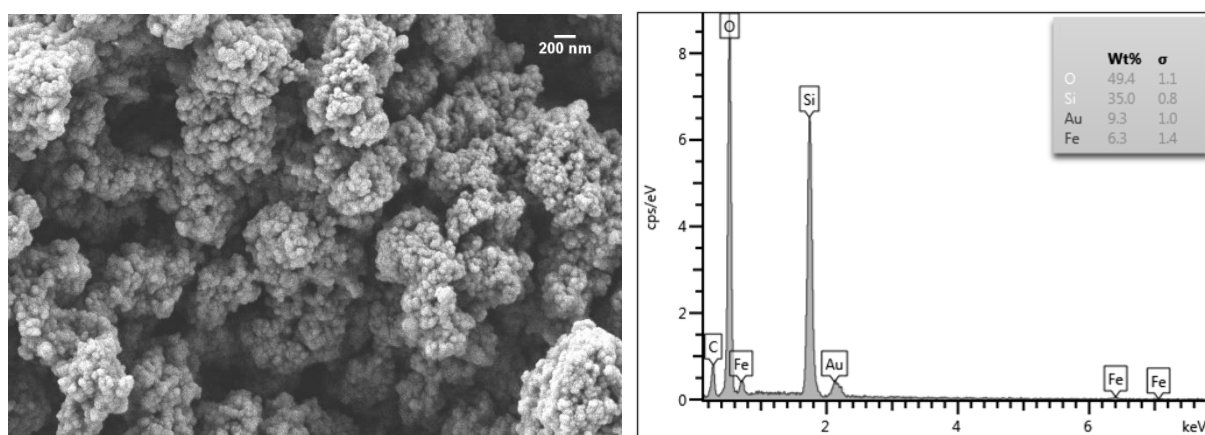


Figure 50. SEM image and EDS spectrum of the IO/SiO<sub>2</sub>/mSiO<sub>2</sub> particles.

#### 4.3.2. Magnetic Characterization

A suspension of the IO/SiO<sub>2</sub>/mSiO<sub>2</sub> particles was observed in the presence of a magnet, in order to study its magnetic behaviour – Figure 51. As it can be observed in Figure 51, these particles also exhibit magnetic behaviour in the presence of a magnet.

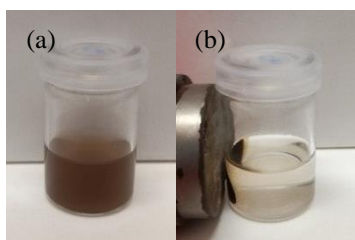
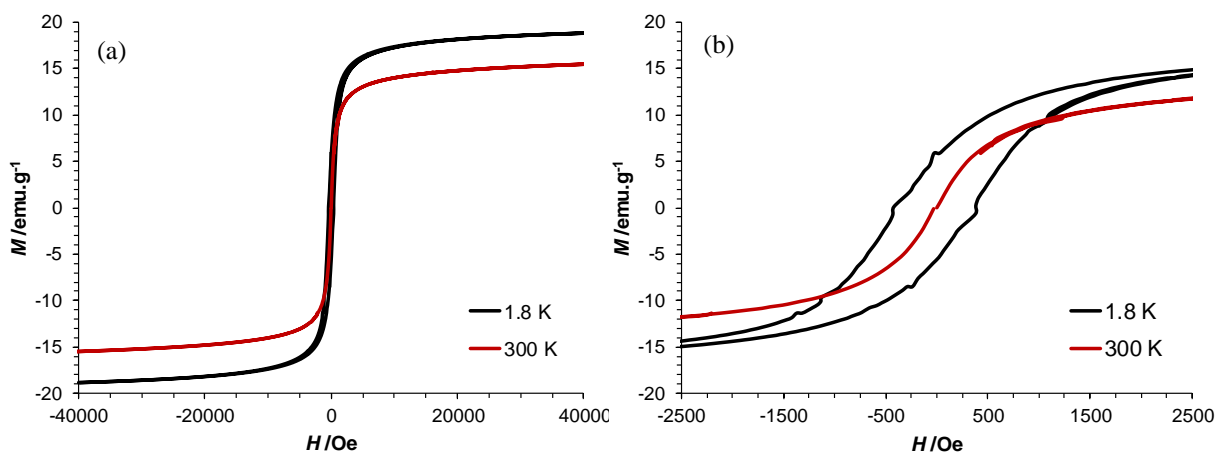


Figure 51. IO/SiO<sub>2</sub>/mSiO<sub>2</sub> particles (a) in the absence and (b) in the presence of a magnet.

#### Vibrating Sample Magnetometer

In Figure 53 and Figure 52, the magnetization curves for the SPIONs produced by microemulsion and for the IO/SiO<sub>2</sub>/mSiO<sub>2</sub> particles are presented.



**Figure 52.** (a) Magnetization curves of the SPIONs produced by microemulsion and (b) detailed view around the origin of the plot.

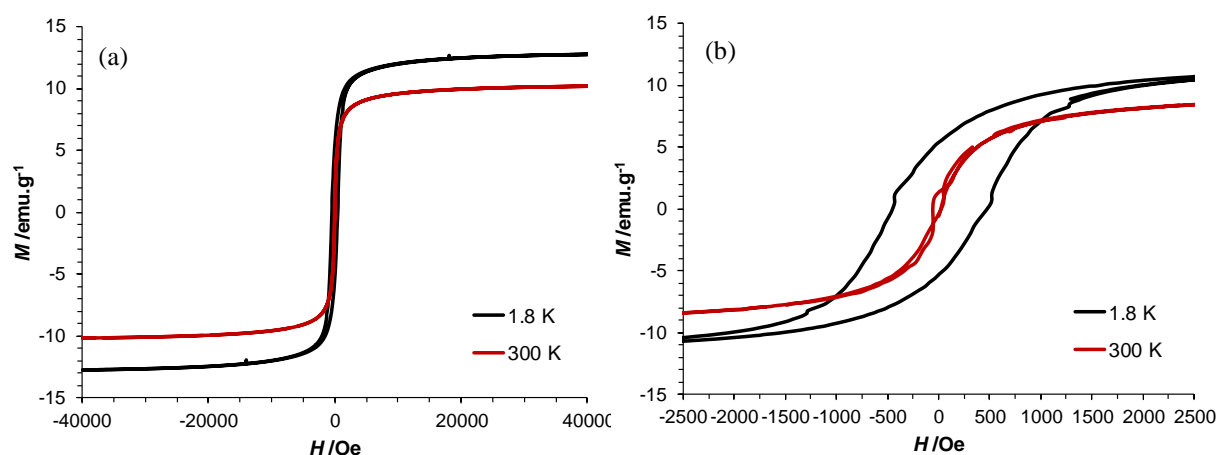


**Figure 53.** (a) Magnetization curves of the IO/SiO<sub>2</sub>/mSiO<sub>2</sub> particles and (b) detailed view around the origin of the plot.

The magnetization curves in Figure 53.(a) showed that the SPIONs obtained by microemulsion had a saturation magnetization of  $15.5 \text{ emu.g}^{-1}$  at 300 K. This value is much smaller than the one obtained for SPIONs produced by thermal decomposition ( $73.2 \text{ emu.g}^{-1}$ ). This difference is related to the oleylamine coating in the SPIONs obtained by thermal decomposition, which protects the SPIONs from oxidation. In the case of SPIONs produced by microemulsion, they have OH groups on the surface, which promotes their oxidation (Campos-Gonçalves *et al.*, 2017). The VSM measurements were made some time after these SPIONs were synthesised. Therefore, even though they were vacuum dried, partial oxidation might have occurred and, thus, their saturation magnetization might be slightly higher right after their synthesis.

For the IO/SiO<sub>2</sub>/mSiO<sub>2</sub> particles, in Figure 52.(a), it can be seen that the saturation magnetization at 300 K is  $10.2 \text{ emu.g}^{-1}$  and at 1.8 K is  $12.7 \text{ emu.g}^{-1}$ . Both these values are

smaller than those obtained for the SPIONs obtained by microemulsion, but this difference is not as significant as the difference between the SPIONs produced by thermal decomposition and the IO-OAm/mSiO<sub>2</sub> and IO-APTES/mSiO<sub>2</sub> nanoparticles. Given the size of the IO/SiO<sub>2</sub>/mSiO<sub>2</sub> particles, a higher decrease in the saturation magnetization would be expected if they only had one iron oxide core, since the amount of silica would be much higher. Therefore, this slight decrease corroborates what had already been hypothesised by TEM and EDS, which is that multiple iron oxide nanoparticles are incorporated inside IO/SiO<sub>2</sub>/mSiO<sub>2</sub> particle.

In Figure 53.(b), it can be seen that the magnetization curves have hysteresis at 1.8 K, but no hysteresis can be seen at 300 K, confirming the superparamagnetism of these iron oxide nanoparticles. Figure 52.(b) also confirms the superparamagnetic behaviour of the IO/SiO<sub>2</sub>/mSiO<sub>2</sub> particles.

The FC and ZFC magnetization curves can be found in Figure 54.

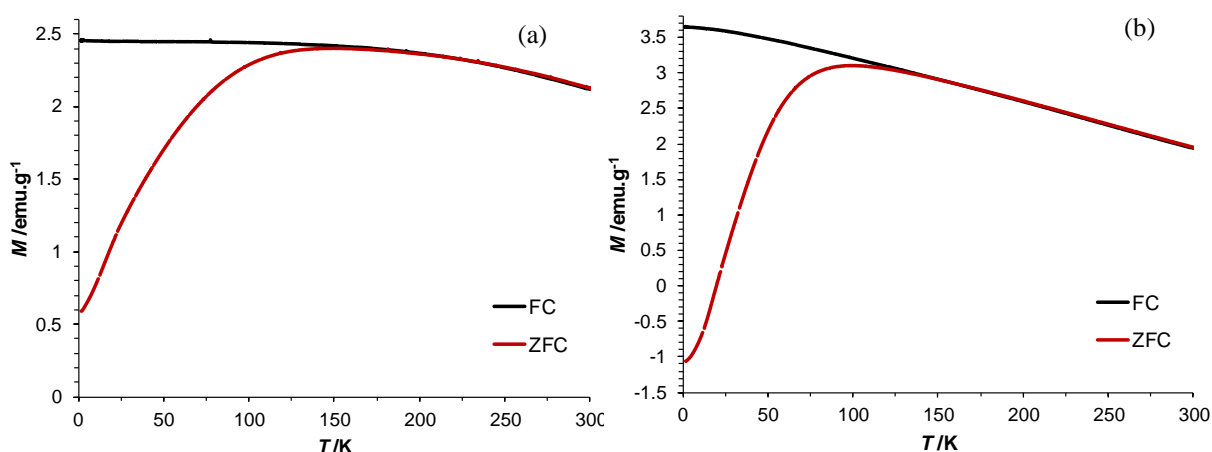


**Figure 54.** FC and ZFC curves obtained with a magnetic field of 100 Oe for (a) the SPIONs obtained by microemulsion and (b) the IO/SiO<sub>2</sub>/mSiO<sub>2</sub> particles.

The FC curves show that the magnetization of SPIONs depends less on temperature than the magnetization of IO/SiO<sub>2</sub>/mSiO<sub>2</sub> particles, which was also the case for the other synthesised nanoparticles.

From Figure 54, it can be seen that the blocking temperature of the SPIONs synthesised by microemulsion is ~130 K and of the IO/SiO<sub>2</sub>/mSiO<sub>2</sub> particles is ~90 K.

#### 4.3.3. Drug Loading

The IO/SiO<sub>2</sub>/mSiO<sub>2</sub> particles were also tested in the loading of epirubicin. The procedures as well as the calculations were similar to the ones presented for the other nanoparticles.



However, for IO/SiO<sub>2</sub>/mSiO<sub>2</sub>, only one loading experiment was carried out. The values obtained for the three quantifications of this loading are presented in Table 12.

**Table 12.** Loading content and entrapment efficiency for IO/SiO<sub>2</sub>/mSiO<sub>2</sub> particles.

$m_{NPs}$ /mg	Quantification 1		Quantification 2		Quantification 3		Mean	
	LC (%)	EE (%)	LC (%)	EE (%)	LC (%)	EE (%)	LC (%)	EE (%)
5.00	3.49	6.98	3.33	6.66	3.29	6.59	3.37 ± 0.11	6.70 ± 0.21

The IO/SiO<sub>2</sub>/mSiO<sub>2</sub> nanoparticles have a loading content of 3.37%, which is again in the same range as those obtained in MMSNs for doxorubicin in Table 3.

#### 4.3.4. Drug Release

After the loading of IO/SiO<sub>2</sub>/mSiO<sub>2</sub> particles, the release of epirubicin in PBS was tested. For these particles, only two loaded samples were used. The release profile is presented in Figure 55.

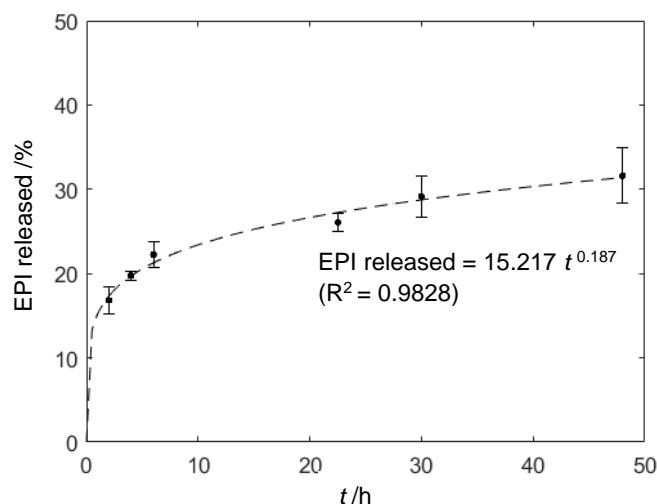


**Figure 55.** Release profile of epirubicin and Korsmeyer-Peppas model for the IO/SiO<sub>2</sub>/mSiO<sub>2</sub> nanoparticles.

These nanoparticles released 31.6±3.3% of epirubicin after 48 hours, which is a very high value for experiments at pH=7.4. The Korsmeyer-Peppas model led once more to a good fit to the data with a R<sup>2</sup> of 0.9828. The parameters of this model were  $k=15.217$  and  $n=0.187$ , indicating once more Fickian diffusion even though  $n<0.43$ . As mentioned before, Ritger and Peppas (1987) explained that the dispersity of the small particles could lead to values much smaller than the expected 0.43 and values as small as 0.12 have been found in the literature for drug release in nanoparticles (Daryasari *et al.*, 2016).

#### 4.4. Comparison between the synthesised nanoparticles

For an easier comparison of the different synthesised particles, the relevant results for IO-OAm/mSiO<sub>2</sub>, IO-APTES/mSiO<sub>2</sub> and IO/SiO<sub>2</sub>/mSiO<sub>2</sub> particles are presented in Table 13.

**Table 13.** Comparison of the different properties and performance of the synthesised particles.

	IO-OAm/mSiO <sub>2</sub>	IO-APTES/mSiO <sub>2</sub>	IO/SiO <sub>2</sub> /mSiO <sub>2</sub>
Size /nm	61.3±12.3	32.9±5.6	371.6±159.4
Zeta Potential /mV	-21.30	-26.30	-30.90
M <sub>s</sub> at 300 K /emu.g <sup>-1</sup>	~4.0	~1.8	~10.2
Drug loading Content /%	3.06±0.22	3.31±0.87	3.37±0.11
Drug release after 48 h /%	19.0±2.8	23.6±4.5	31.6±3.3
Model Parameters	$k=7.979; n=0.221$	$k=7.905; n=0.288$	$k=15.217; n=0.187$
	Fickian diffusion	Fickian diffusion	Fickian diffusion

All the synthesised nanoparticles had porosity, which was confirmed by the microscopy characterization and agrees with the obtained zeta potential, indicating that the removal of the surfactant was successful. IO/SiO<sub>2</sub>/mSiO<sub>2</sub> nanoparticles are the only that present zeta potential more negative than -30 mV and, thus, form stable dispersions in water (pH=7).

In Table 13, the magnetism of the nanoparticles can also be confirmed, with the IO/SiO<sub>2</sub>/mSiO<sub>2</sub> particles having an higher saturation magnetization at 300 K. Furthermore, in the presence of a magnet, they were all attracted to it, even the IO-APTES/mSiO<sub>2</sub> nanoparticles that showed a very small saturation magnetization.

Comparing the loading content of the three types of nanoparticles, the values obtained were very close to each other, with IO/SiO<sub>2</sub>/mSiO<sub>2</sub> particles showing a slightly higher value. The very small difference in the loading content might be an indication that the interaction between the drug and the nanoparticles is not significantly dependent on their size. Additionally, all these values were in accordance with those found in literature for MMSNs.

In terms of the release of epirubicin, all the nanoparticles showed higher percentage of release than those found in literature for doxorubicin, an analogue drug of epirubicin, with the IO/SiO<sub>2</sub>/mSiO<sub>2</sub> particles also having a higher release percentage. However, their size might be a drawback for their application in drug delivery.

The use of the Korsmeyer-Peppas model led to values of  $n$  (exponent) lower than the expected in all three cases, which has also been reported in the literature as a common behaviour for nanoparticles (Daryasari *et al.*, 2016; Patel *et al.*, 2016; Ronhovde *et al.*, 2017; Souza *et al.*, 2009). The IO-APTES/mSiO<sub>2</sub> nanoparticles had a higher value of  $n$  (0.288) than the other two

(closer to 0.43), which might be due to the fact that they are less polydisperse, as can be seen by the standard deviation of their average diameter.

Considering the magnetic properties and drug loading capacity of the nanoparticles, their application in magnetically targeted delivery of drugs appears to be promising.



## 5. Conclusions and Future Works

In this work, nanoparticles with iron oxide in the core and a mesoporous silica shell were synthesised. Different methods were studied for the synthesis of iron oxide nanoparticles and for their incorporation in the silica shell, the latter being generally synthesised by sol-gel with slight differences. Two types of drying of the nanoparticles were also employed, in order to study their effect on the structure and property of the nanoparticles.

For the IO-OAm/mSiO<sub>2</sub> and IO-APTES/mSiO<sub>2</sub> nanoparticles, iron oxide was obtained by thermal decomposition, which leads to SPIONs with high saturation magnetization (73.2 emu.g<sup>-1</sup>) and has the advantage of the oleylamine coating, which protects them from oxidation. However, they are hydrophobic and two strategies were studied to transfer them into water, in order to build on them the silica shell. For IO-OAm/mSiO<sub>2</sub>, chloroform and an aqueous solution of CTAB were used and CTAB worked both as the stabilizing agent of the SPIONs in water and as the template agent for the mesoporous structure of silica. The success of this synthesis was confirmed by the presence of the silica peaks in FTIR and, even though this analysis could barely detect the presence of iron oxide, its presence was proved by EDS and by the superparamagnetism of the nanoparticles. The saturation magnetization of these nanoparticles was low (4.0 emu.g<sup>-1</sup>) compared to the core SPIONs, which is related to the high content of silica in the nanoparticles and oxidation during the drying stage. The negative zeta potential of the nanoparticles confirmed the removal of the surfactant and thus, the existence of a mesoporous structure, also seen by electron microscopy.

Two different drying techniques were also studied for the IO-OAm/mSiO<sub>2</sub> nanoparticles: supercritical fluids drying (SCD) and ambient pressure drying (APD) at 60°C. SCD was proven to be better than APD, in terms of inducing porosity, which led to more negative zeta potential, and in terms of aggregation and polydispersity, since the SCD nanoparticles showed lower polydispersity index and diameter on DLS and lower standard deviation and size on TEM. However, SCD led to lower saturation magnetization, because significant oxidation of the nanoparticles occurred, which was confirmed by the presence of hematite by Mössbauer spectroscopy.

For the IO-APTES/mSiO<sub>2</sub> nanoparticles, a different strategy of transferring the hydrophobic SPIONs into water was employed. It consisted in a ligand exchange procedure, where the oleylamine-coated SPIONs and APTES were mixed, being the oleylamine molecules exchanged with the silica precursor, which condensates around the iron oxide nanoparticles and is hydrophilic, thus making the dispersion of the SPIONs in water possible. The success of the ligand exchange reaction was confirmed once again by FTIR, which showed both the peaks for

silica and iron oxide, and by TGA. The sol-gel reaction to obtain the mesoporous silica shell was also confirmed by FTIR and EDS and the potential zeta proves the successful removal of CTAB. The obtained nanoparticles showed superparamagnetic behaviour, but their saturation magnetization was lower than for the IO-OAm/mSiO<sub>2</sub> nanoparticles (1.8 emu.g<sup>-1</sup>). This could be justified with the fact that, after removing oleylamine from the SPIONs, these are more prone to oxidation, even with the coating of APTES.

In the literature, the strategy used to transfer hydrophobic SPIONs into water was the one used with the IO-OAm/mSiO<sub>2</sub> nanoparticles. Therefore, the synthesis of the IO-APTES/mSiO<sub>2</sub> nanoparticles is innovative, since similar nanoparticles were not found in literature.

In terms of size, both IO-OAm/mSiO<sub>2</sub> and IO-APTES/mSiO<sub>2</sub> nanoparticles were expected to have sizes around 50 nm, according to the followed procedure. Their size was characterized by SEM and TEM, respectively, and showed a diameter of 61.3±12.3 nm for IO-OAm/mSiO<sub>2</sub> and 32.9±5.6 nm for IO-APTES/mSiO<sub>2</sub>. Both of these nanoparticles have small sizes but IO-APTES/mSiO<sub>2</sub> has both smaller average diameter and standard deviation. A possible explanation for this result is that the presence of the aminopropyl spacer in the SPIONs could be restricting the condensation of TEOS due to less amount of OH groups on the SPIONs surface. Therefore, the growth of the shell is more controlled and leads to smaller and less polydisperse nanoparticles. This is confirmed by the lower PDI obtained in DLS.

In the case of the IO/SiO<sub>2</sub>/mSiO<sub>2</sub> nanoparticles, iron oxide was obtained by microemulsion, which had the advantage of the SPIONs being hydrophilic. In order to prevent oxidation, they were coated first with a non-porous silica coat, before the formation of the mesoporous silica shell. This method led to larger nanoparticles with a size of 371.6±159.4 nm, obtained by TEM. These nanoparticles had a dark brown colour, which was not expected for nanoparticles of this size with only one iron oxide core. This fact together with the higher value of saturation magnetization of these particles (10.2 emu.g<sup>-1</sup>) led to the conclusion that they must have multiple iron oxide cores, instead of just one. This was confirmed by TEM where various small black seeds with diameter around 10 nm could be seen inside a particle.

In terms of drug loading and release experiments, epirubicin was used as model drug. The loading content obtained was very similar for the three types of particles (between 3.06 and 3.37%) and it is also in the range of values found in literature. Thus, the potential of the synthesised nanoparticles to be loaded with antitumour drugs was confirmed. The release of epirubicin led to values higher than those found in literature, which also makes them promising for this application. The release profiles were modelled with the Korsmeyer-Peppas model and, considering the R<sup>2</sup> obtained, good fit to the data was achieved. Thus, it was concluded that this model could be used to predict the release behaviour of epirubicin from these nanoparticles.

The IO/SiO<sub>2</sub>/mSiO<sub>2</sub> particles appear to be the most promising in terms of drug loading and release and in terms of magnetic behaviour and, therefore, have the most potential to be used in biomedical applications, particularly for antitumour strategies. However, their size is the main drawback of these particles.

To sum up, three different types of nanoparticles were synthesised that led to very interesting results. Nevertheless, due to the short time of this work, many possibilities were left unexplored and can be a starting point for future work.

First, the DLS, TEM and SEM results showed that aggregation was a very serious problem for silica nanoparticles. Therefore, one thing that could be explored in the future is the functionalization of these nanoparticles with organosilanes, by co-condensation or by post-grafting, in order to restrict the aggregation of the nanoparticles. Furthermore, functionalization of the nanoparticles could also be used to increase the drug loading or, in the case of IO/SiO<sub>2</sub>/mSiO<sub>2</sub> particles, co-condensation with organosilanes could also help control their size, in order to obtain nanoparticles.

In the synthesis of the mesoporous silica shell, many parameters of the synthesis could be studied, such as changing the reaction time, temperature and surfactant/silica precursor ratio and assess the effect of these changes in the particle and pore sizes. Once again, this would be particularly interesting in the case of IO/SiO<sub>2</sub>/mSiO<sub>2</sub> particles, in order to reduce their size.

It would also be interesting to study the ligand exchange reaction more deeply to better understand it.

Since supercritical drying led to significant oxidation of the nanoparticles and APD caused their aggregation, lyophilization could be an alternative to explore in the future.

On the other hand, in the release experiments, it is also important to test other release conditions, particularly the release in acidic pH, since the pH in tumoral cells is around 5 and the epirubicin release from MSNs is said to be pH-dependent. Furthermore, it would also be relevant to test the influence of the presence of a magnetic field in the drug release, to confirm that these nanoparticles could be used for magnetically targeted release. The loading conditions could also be studied and optimized in order to increase the entrapment efficiency and therefore decrease the amount of drug wasted.

Finally, the study of the potential of the synthesised nanoparticles to be used as contrast agents in MRI is a natural future step, in order to confirm the ability of these systems as multifunctional platforms for biomedicine.





## References

- Al-Oweini, R., & El-Rassy, H. (2009). Synthesis and characterization by FTIR spectroscopy of silica aerogels prepared using several  $\text{Si}(\text{OR})_4$  and  $\text{R}''\text{Si}(\text{OR}')_3$  precursors. *Journal of Molecular Structure*, *919*(1–3), 140–145.
- Albulet, D., Florea, D. A., Boarca, B., Ditu, L. M., Chifiriuc, M. C., Grumezescu, A. M., & Andronescu, E. (2017). Nanotechnology for personalized medicine: cancer research, diagnosis, and therapy. In A. Ficai & A. M. Grumezescu (Eds.), *Nanostructures for Cancer Therapy* (pp. 1–21). Amsterdam, Netherlands: Elsevier.
- Allothman, Z. A. (2012). A Review: Fundamental Aspects of Silicate Mesoporous Materials. *Materials*, *5*(12), 2874–2902.
- Alvarez-Berriós, M. P., Sosa-Cintrón, N., Rodríguez-Lugo, M., Juneja, R., & Vivero-Escoto, J. L. (2016). Hybrid Nanomaterials Based on Iron Oxide Nanoparticles and Mesoporous Silica Nanoparticles: Overcoming Challenges in Current Cancer Treatments. *Journal of Chemistry*, *2016*, 1–15.
- Angelakeris, M. (2017). Magnetic nanoparticles: A multifunctional vehicle for modern theranostics. *Biochimica et Biophysica Acta (BBA) - General Subjects*, *1861*(6), 1642–1651.
- Asefa, T., & Tao, Z. (2012). Biocompatibility of Mesoporous Silica Nanoparticles. *Chemical Research in Toxicology*, *25*(11), 2265–2284.
- Avedian, N., Zaaeri, F., Daryasari, M. P., Akbari Javar, H., & Khoobi, M. (2018). pH-sensitive biocompatible mesoporous magnetic nanoparticles labeled with folic acid as an efficient carrier for controlled anticancer drug delivery. *Journal of Drug Delivery Science and Technology*, *44*(January), 323–332.
- Blundell, S. (2001). *Magnetism in Condensed Matter (Oxford Master Series in Physics)*. New York, NY: Oxford University Press.
- Buschow, K. H. J., & de Boer, F. R. (2003a). Introduction. In *Physics of Magnetism and Magnetic Materials* (pp. 1–2). Boston, MA: Springer US.
- Buschow, K. H. J., & de Boer, F. R. (2003b). Measurement Techniques. In *Physics of Magnetism and Magnetic Materials* (pp. 85–89). Boston, MA: Springer US.
- Campbell, W. H. (2001). Nature's Magnetism. In *Earth Magnetism. A Guided Tour through Magnetic Fields*. (pp. 1–23). San Diego, CA: Harcourt-Academic Press (Elsevier Science).
- Campos-Gonçalves, I., Costa, B. F. O., Santos, R. F., & Durães, L. (2017). Superparamagnetic core-shell nanocomplexes doped with  $\text{Yb}^{3+}$ :  $\text{Er}^{3+}$ / $\text{Ho}^{3+}$  + rare-earths for upconversion fluorescence. *Materials & Design*, *130*, 263–274.
- Chang, B., Guo, J., Liu, C., Qian, J., & Yang, W. (2010). Surface functionalization of magnetic mesoporous silica nanoparticles for controlled drug release. *Journal of Materials Chemistry*, *20*(44), 9941–9947.
- Chen, Y., Zhang, H., Cai, X., Ji, J., He, S., & Zhai, G. (2016). Multifunctional mesoporous silica nanocarriers for stimuli-responsive target delivery of anticancer drugs. *RSC Advances*, *6*(94), 92073–92091.
- Chirayil, C. J., Abraham, J., Mishra, R. K., George, S. C., & Thomas, S. (2017). Instrumental Techniques for the Characterization of Nanoparticles. In S. Thomas, R. Thomas, A. K. Zachariah, & R. K. Mishra (Eds.), *Thermal and Rheological Measurement Techniques*

for *Nanomaterials Characterization* (pp. 1–36). Amsterdam, Netherlands: Elsevier.

Colilla, M., González, B., & Vallet-Regí, M. (2013). Mesoporous silica nanoparticles for the design of smart delivery nanodevices. *Biomaterials Science*, *1*(2), 114–134.

Cornell, R. M., & Schwertmann, U. (2003). *The iron oxides : structure, properties, reactions, occurrences, and uses*. Weinheim, Germany: Wiley-VCH.

Daryasari, M. P., Akhgar, M. R., Mamashli, F., Bigdeli, B., & Khoobi, M. (2016). Chitosan-folate coated mesoporous silica nanoparticles as a smart and pH-sensitive system for curcumin delivery. *RSC Advances*, *6*(107), 105578–105588.

Davis, K., Cole, B., Ghelardini, M., Powell, B. A., & Mefford, O. T. (2016). Quantitative Measurement of Ligand Exchange with Small-Molecule Ligands on Iron Oxide Nanoparticles via Radioanalytical Techniques. *Langmuir*, *32*(51), 13716–13727.

De Palma, R., Peeters, S., Van Bael, M. J., Van den Rul, H., Bonroy, K., Laureyn, W., Mullens, J., Borghs, G., & Maes, G. (2007). Silane Ligand Exchange to Make Hydrophobic Superparamagnetic Nanoparticles Water-Dispersible. *Chemistry of Materials*, *19*(7), 1821–1831.

Douroumis, D., Onyesom, I., Maniruzzaman, M., & Mitchell, J. (2013). Mesoporous silica nanoparticles in nanotechnology. *Critical Reviews in Biotechnology*, *33*(3), 229–245.

Durdureanu-Angheluta, A., Dascalu, A., Fifere, A., Coroaba, A., Pricop, L., Chiriac, H., Tura, V., Pinteala, M., & Simionescu, B. C. (2012). Progress in the synthesis and characterization of magnetite nanoparticles with amino groups on the surface. *Journal of Magnetism and Magnetic Materials*, *324*(9), 1679–1689.

Feng, Y., Panwar, N., Tng, D. J. H., Tjin, S. C., Wang, K., & Yong, K.-T. (2016). The application of mesoporous silica nanoparticle family in cancer theranostics. *Coordination Chemistry Reviews*, *319*, 86–109.

Figueiredo, M. (2013). Sizing Nanoparticles in Liquids: An Overview of Methods. In J. Coelho (Ed.), *Drug Delivery Systems: Advanced Technologies Potentially Applicable in Personalised Treatment* (pp. 87–107). Dordrecht: Springer Netherlands.

Gan, Q., Lu, X., Yuan, Y., Qian, J., Zhou, H., Lu, X., Shi, J., & Liu, C. (2011). A magnetic, reversible pH-responsive nanogated ensemble based on Fe<sub>3</sub>O<sub>4</sub> nanoparticles-capped mesoporous silica. *Biomaterials*, *32*(7), 1932–1942.

Gaspar, A. S., Wagner, F. E., Amaral, V. S., Costa Lima, S. A., Khomchenko, V. A., Santos, J. G., Costa, B. F. O., & Durães, L. (2017). Development of a biocompatible magnetic nanofluid by incorporating SPIONs in Amazonian oils. *Spectrochimica Acta Part A: Molecular and Biomolecular Spectroscopy*, *172*, 135–146.

Gonçalves, I. (2016). *Fluorescência por upconversion de nanocomplexos multifuncionais de Fe<sub>3</sub>O<sub>4</sub> dopados com lantanídeos*. Tese de Mestrado. Universidade de Coimbra.

Goodhew, P., Humphreys, J., & Beanland, R. (2001). The scanning electron microscope. In *Electron Microscopy and Analysis* (3rd ed., pp. 122–168). London, England: Taylor & Francis.

He, Y., Luo, L., Liang, S., Long, M., & Xu, H. (2017). Amino-functionalized mesoporous silica nanoparticles as efficient carriers for anticancer drug delivery. *Journal of Biomaterials Applications*, *32*(4), 524–532.

Knežević, N. Ž., Ruiz-Hernandez, E., Hennink, W. E., & Vallet-Regí, M. (2013). Magnetic mesoporous silica-based core/shell nanoparticles for biomedical applications. *RSC*

*Advances*, 3(25), 9584–9593.

Knežević, N. Ž., Slowing, I. I., & Lin, V. S. Y. (2012). Tuning the release of anticancer drugs from magnetic iron oxide/mesoporous silica core/shell nanoparticles. *ChemPlusChem*, 77(1), 48–55.

Larsen, B. A., Hurst, K. M., Ashurst, W. R., Serkova, N. J., & Stoldt, C. R. (2012). Mono and dialkoxysilane surface modification of superparamagnetic iron oxide nanoparticles for application as magnetic resonance imaging contrast agents. *Journal of Materials Research*, 27(14), 1846–1852.

Laurent, S., Forge, D., Port, M., Roch, A., Robic, C., Vander Elst, L., & Muller, R. N. (2008). Magnetic Iron Oxide Nanoparticles: Synthesis, Stabilization, Vectorization, Physicochemical Characterizations, and Biological Applications. *Chemical Reviews*, 108(6), 2064–2110.

Li, T., Shen, X., Geng, Y., Chen, Z., Li, L., Li, S., Yang, H., Wu, C., Zeng, H., & Liu, Y. (2016). Folate-Functionalized Magnetic-Mesoporous Silica Nanoparticles for Drug/Gene Codelivery to Potentiate the Antitumor Efficacy. *ACS Applied Materials and Interfaces*, 8(22), 13748–13758.

Li, Z., Barnes, J. C., Bosoy, A., Stoddart, J. F., & Zink, J. I. (2012). Mesoporous silica nanoparticles in biomedical applications. *Chemical Society Reviews*, 41(7), 2590–2605.

Lieberman, A., Mendez, N., Trogler, W. C., & Kummel, A. C. (2014). Synthesis and surface functionalization of silica nanoparticles for nanomedicine. *Surface Science Reports*, 69(2–3), 132–158.

Liong, M., Lu, J., Kovoichich, M., Xia, T., Ruehm, S. G., Nel, A. E., Tamanoi, F., & Zink, J. I. (2008). Multifunctional inorganic nanoparticles for imaging, targeting, and drug delivery. *ACS Nano*, 2(5), 889–896.

Loganathan, S., Valapa, R. B., Mishra, R. K., Pugazhenthii, G., & Thomas, S. (2017). Thermogravimetric Analysis for Characterization of Nanomaterials. In S. Thomas, R. Thomas, A. K. Zachariah, & R. K. Mishra (Eds.), *Thermal and Rheological Measurement Techniques for Nanomaterials Characterization* (pp. 67–108). Amsterdam, Netherlands: Elsevier.

Luo, L., Liang, Y., Erichsen, E. S., & Anwender, R. (2017). Monodisperse mesoporous silica nanoparticles of distinct topology. *Journal of Colloid and Interface Science*, 495, 84–93.

Luong, T. T., Knoppe, S., Bloemen, M., Brullot, W., Strobbe, R., Locquet, J. P., & Verbiest, T. (2016). Magnetothermal release of payload from iron oxide/silica drug delivery agents. *Journal of Magnetism and Magnetic Materials*, 416, 194–199.

Mahmoudi, M., Sant, S., Wang, B., Laurent, S., & Sen, T. (2011). Superparamagnetic iron oxide nanoparticles (SPIONs): Development, surface modification and applications in chemotherapy. *Advanced Drug Delivery Reviews*, 63(1–2), 24–46.

Mai, W. X., & Meng, H. (2013). Mesoporous silica nanoparticles: A multifunctional nano therapeutic system. *Integrative Biology*, 5(1), 19–28.

Maleki, H., Simchi, A., Imani, M., & Costa, B. F. O. (2012). Size-controlled synthesis of superparamagnetic iron oxide nanoparticles and their surface coating by gold for biomedical applications. *Journal of Magnetism and Magnetic Materials*, 324(23), 3997–4005.

Malekigorji, M., Curtis, A. D., & Hoskins, C. (2014). The Use of Iron Oxide Nanoparticles for Pancreatic Cancer Therapy. *Journal of Nanomedicine Research*, 1(1), 1–12.

Mohammed, L., Gomaa, H. G., Ragab, D., & Zhu, J. (2017). Magnetic nanoparticles for

environmental and biomedical applications: A review. *Particuology*, 30, 1–14.

Mueller, P. S., Parker, C. P., & Larsen, S. C. (2015). One-pot synthesis of iron oxide mesoporous silica core/shell nanocomposites. *Microporous and Mesoporous Materials*, 204(C), 173–179.

Nandiyanto, A. B. D., Kim, S.-G., Iskandar, F., & Okuyama, K. (2009). Synthesis of spherical mesoporous silica nanoparticles with nanometer-size controllable pores and outer diameters. *Microporous and Mesoporous Materials*, 120(3), 447–453.

Nooney, R. I., Thirunavukkarasu, D., Chen, Y., Josephs, R., & Ostafin, A. E. (2002). Synthesis of Nanoscale Mesoporous Silica Spheres with Controlled Particle Size. *Chemistry of Materials*, 14(11), 4721–4728.

O' Connor, C. J., Jinke, T., & Zhang, J. H. (2001). Nanostructured Magnetic Materials. In *Magnetism: Molecules to Materials III* (pp. 1–36). Wiley-Blackwell.

Omar, H., Croissant, J. G., Alamoudi, K., Alsaiani, S., Alradwan, I., Majrashi, M. A., Anjum, D. H., Martins, P., Laamarti, R., Eppinger, J., Moosa, B., Almalik, A., & Khashab, N. M. (2017). Biodegradable Magnetic Silica@Iron Oxide Nanovectors with Ultra-Large Mesopores for High Protein Loading, Magnetothermal Release, and Delivery. *Journal of Controlled Release*, 259, 187–194.

Patel, K., Sundara Raj, B., Chen, Y., & Lou, X. (2016). Cytotoxicity of folic acid conjugated hollow silica nanoparticles toward Caco2 and 3T3 cells, with and without encapsulated DOX. *Colloids and Surfaces B: Biointerfaces*, 140, 213–222.

Pednekar, P. P., Godiyal, S. C., Jadhav, K. R., & Kadam, V. J. (2017). Mesoporous silica nanoparticles: a promising multifunctional drug delivery system. In A. Ficaí & A. M. Grumezescu (Eds.), *Nanostructures for Cancer Therapy* (pp. 593–621). Amsterdam, Netherlands: Elsevier.

Pedrosa, J., Costa, B. F. O., Portugal, A., & Durães, L. (2015). Controlled phase formation of nanocrystalline iron oxides/hydroxides in solution – An insight on the phase transformation mechanisms. *Materials Chemistry and Physics*, 163, 88–98.

Perkampus, H.-H. (1992). Principles. In *UV-VIS Spectroscopy and Its Applications* (pp. 3–9). Berlin, Heidelberg: Springer Berlin Heidelberg.

Pershina, A., Demin, A., V Ivanov, V., Nevskaya, K., Shevelev, O., Minin, A., Byzov, I., Sazanov, A., Krasnov, V. P., & Ogorodova, L. M. (2016). 3-Aminopropylsilane-modified iron oxide nanoparticles for contrast-enhanced magnetic resonance imaging of liver lesions induced by *Opisthorchis felinus*. *International Journal of Nanomedicine*, Volume 11, 4451–4463.

Pierre, A. C., & Rigacci, A. (2011). SiO<sub>2</sub> Aerogels. In M. A. Aegerter, N. Leventis, & M. M. Koebel (Eds.), *Aerogels Handbook* (pp. 21–45). New York, NY: Springer New York.

Qiao, R., Yang, C., & Gao, M. (2009). Superparamagnetic iron oxide nanoparticles: from preparations to in vivo MRI applications. *Journal of Materials Chemistry*, 19(35), 6274–6293.

Rahman, I. A., & Padavettan, V. (2012). Synthesis of Silica nanoparticles by Sol-Gel: Size-dependent properties, surface modification, and applications in silica-polymer nanocomposites: a review. *Journal of Nanomaterials*, 2012, 1–15.

Ritger, P. L., & Peppas, N. A. (1987). A simple equation for description of solute release I. Fickian and non-fickian release from non-swellable devices in the form of slabs, spheres, cylinders or discs. *Journal of Controlled Release*, 5(1), 23–36.

- Roca, A. G., Costo, R., Rebolledo, A. F., Veintemillas-Verdaguer, S., Tartaj, P., González-Carreño, T., Morales, M. P., & Sernas, C. J. (2009). Progress in the preparation of magnetic nanoparticles for applications in biomedicine. *Journal of Physics D: Applied Physics*, 42(22), 224002.
- Ronhovde, C. J., Baer, J., & Larsen, S. C. (2017). Effects of pore topology and iron oxide core on doxorubicin loading and release from mesoporous silica nanoparticles. *Journal of Nanoparticle Research*, 19(6), 215.
- Santos, P. (2015). *Desenvolvimento de um Nanofluido Biodegradável para Libertação de Fármaco no Cérebro*. Tese de Mestrado. Universidade de Coimbra.
- Saroj, S., & Rajput, S. J. (2018). Composite smart mesoporous silica nanoparticles as promising therapeutic and diagnostic candidates: Recent trends and applications. *Journal of Drug Delivery Science and Technology*, 44, 349–365.
- Sayari, A. (2003). Mesoporous Materials. In P. Yang (Ed.), *The chemistry of nanostructured materials* (pp. 39–68). New Jersey: World Scientific.
- Shi, Y., Miller, M. L., & Di Pasqua, A. J. (2016). Biocompatibility of Mesoporous Silica Nanoparticles? *Comments on Inorganic Chemistry*, 36(2), 61–80.
- Singh, L. P., Bhattacharyya, S. K., Kumar, R., Mishra, G., Sharma, U., Singh, G., & Ahalawat, S. (2014). Sol-Gel processing of silica nanoparticles and their applications. *Advances in Colloid and Interface Science*, 214, 17–37.
- Sodipo, B. K., & Aziz, A. A. (2016). Recent advances in synthesis and surface modification of superparamagnetic iron oxide nanoparticles with silica. *Journal of Magnetism and Magnetic Materials*, 416, 275–291.
- Souza, K. C., Ardisson, J. D., & Sousa, E. M. B. (2009). Study of mesoporous silica/magnetite systems in drug controlled release. *Journal of Materials Science: Materials in Medicine*, 20(2), 507–512.
- Stanicki, D., Elst, L. Vander, Muller, R. N., & Laurent, S. (2015). Synthesis and processing of magnetic nanoparticles. *Current Opinion in Chemical Engineering*, 8, 7–14.
- Stuart, B. (2004). *Infrared spectroscopy: fundamentals and applications*. West Sussex, England: John Wiley & Sons.
- Suri, S., Ruan, G., Winter, J., & Schmidt, C. E. (2013). Microparticles and Nanoparticles. In B. D. Ratner, A. S. Hoffman, F. J. Schoen, & J. E. Lemmon (Eds.), *Biomaterials Science* (pp. 360–388). Oxford: Academic Press.
- Suteewong, T., Sai, H., Lee, J., Bradbury, M., Hyeon, T., Gruner, S. M., & Wiesner, U. (2010). Ordered mesoporous silica nanoparticles with and without embedded iron oxide nanoparticles: Structure evolution during synthesis. *Journal of Materials Chemistry*, 20(36), 7807–7814.
- Suzuki, K., Ikari, K., & Imai, H. (2004). Synthesis of Silica Nanoparticles Having a Well-Ordered Mesostructure Using a Double Surfactant System. *Journal of the American Chemical Society*, 126(2), 462–463.
- Tao, C., & Zhu, Y. (2014). Magnetic mesoporous silica nanoparticles for potential delivery of chemotherapeutic drugs and hyperthermia. *Dalton Transactions*, 43(41), 15482–15490.
- Teja, A., & Koh, P. Y. (2009). Synthesis, properties, and applications of magnetic iron oxide nanoparticles. *Progress in Crystal Growth and Characterization of Materials*, 55, 22–45.

Thompson, R., & Oldfield, F. (1986). Techniques of magnetic measurements. In *Environmental Magnetism* (pp. 49–64). Dordrecht: Springer Netherlands.

Tombácz, E., Turcu, R., Socoliuc, V., & Vékás, L. (2015). Magnetic iron oxide nanoparticles: Recent trends in design and synthesis of magnetoresponsive nanosystems. *Biochemical and Biophysical Research Communications*, 468(3), 442–453.

Wu, S.-H., Hung, Y., & Mou, C.-Y. (2011). Mesoporous silica nanoparticles as nanocarriers. *Chemical Communications*, 47(36), 9972–9985.

Wu, S.-H., Mou, C.-Y., & Lin, H.-P. (2013). Synthesis of mesoporous silica nanoparticles. *Chemical Society Reviews*, 42(9), 3862–3875.

Wu, W., Jiang, C. Z., & Roy, V. A. L. (2016). Designed synthesis and surface engineering strategies of magnetic iron oxide nanoparticles for biomedical applications. *Nanoscale*, 8(47), 19421–19474.

Xu, R. (2002). Electrophoretic Light Scattering. In B. Scarlett (Ed.), *Particle Characterization: Light Scattering Methods* (pp. 289–343). Dordrecht: Springer Netherlands.

Yamamoto, E., & Kuroda, K. (2016). Colloidal Mesoporous Silica Nanoparticles. *Bulletin of the Chemical Society of Japan*, 89(5), 501–539.

Yang, P., Quan, Z., Hou, Z., Li, C., Kang, X., Cheng, Z., & Lin, J. (2009). A magnetic, luminescent and mesoporous core–shell structured composite material as drug carrier. *Biomaterials*, 30(27), 4786–4795.

Ye, F., Laurent, S., Fornara, A., Astolfi, L., Qin, J., Roch, A., Martini, A., Toprak, M. S., Muller, R. N., & Muhammed, M. (2012). Uniform mesoporous silica coated iron oxide nanoparticles as a highly efficient, nontoxic MRI T2 contrast agent with tunable proton relaxivities. *Contrast Media & Molecular Imaging*, 7(5), 460–468.

Yoshikawa, S., Kato, N., & Obara, G. (2017). Mesoporous silica hollow capsules embedded with magnetic nanoparticles. *MATEC Web Conference*, 98, 05001.

Zapotoczny, B., Guskos, N., Koziół, J. J., & Dudek, M. R. (2015). Preparation of the narrow size distribution USPIO in mesoporous silica for magnetic field guided drug delivery and release. *Journal of Magnetism and Magnetic Materials*, 374, 96–102.

## **APPENDICES**







## APPENDIX A – Safety of the used chemical substances

When handling chemical substances, their dangers must be taken into account so that the right precautionary measures can be followed. In the next tables, information of the safety and hazards of the different used compounds is presented, compiled from the MSDS of these substances provided by the suppliers.


**Table A.1.** Safety information for iron(III) acetylacetonate

<b>Substance</b>	<b>Iron(III) acetylacetonate</b>
<b>Chemical Formula</b>	$C_{15}H_{21}FeO_6$
<b>Appearance</b>	Dark red powder
<b>Pictograms</b>	
<b>Hazards Statements</b>	H302 - Harmful if swallowed. H319 - Causes serious eye irritation.
<b>Precautionary Statements</b>	P305 + P351 + P338 - If in eyes: rinse cautiously with water for several minutes; remove contact lenses, if present and easy to do; continue rinsing.


**Table A.2.** Safety information for oleylamine

<b>Substance</b>	<b>Oleylamine</b>
<b>Chemical Formula</b>	$C_{18}H_{37}N$
<b>Appearance</b>	Colourless liquid
<b>Pictograms</b>	
<b>Hazards Statements</b>	H302 - Harmful if swallowed. H304 - May be fatal if swallowed and enters airways. H314 - Causes severe skin burns and eye damage. H335 - May cause respiratory irritation. H373 - May cause damage to organs (liver, gastrointestinal tract, immune system) through prolonged or repeated exposure. H410 - Very toxic to aquatic life with long lasting effects.
<b>Precautionary Statements</b>	P260 - Do not breathe dust/ fume/ gas/ mist/ vapours/ spray. P280 - Wear protective gloves/ protective clothing/ eye protection/ face protection. P301 + P310 - If swallowed: immediately call a poison center/doctor. P303 + P361 + P353 - If on skin (or hair): take off immediately all contaminated clothing; rinse skin with water/shower. P304 + P340 + P310 - If inhaled: remove person to fresh air and keep comfortable for breathing; immediately call a poison center/doctor. P305 + P351 + P338 - If in eyes: rinse cautiously with water for several minutes; remove contact lenses, if present and easy to do; continue rinsing.


**Table A.3.** Safety information for benzyl ether

<b>Substance</b>	<b>Benzyl ether</b>
<b>Chemical Formula</b>	C <sub>14</sub> H <sub>14</sub> O
<b>Appearance</b>	Colourless clear liquid
<b>Pictograms</b>	
<b>Hazards Statements</b>	H335 - May cause respiratory irritation. H410 - Very toxic to aquatic life with long lasting effects.
<b>Precautionary Statements</b>	P273 - Avoid release to the environment. P304 + P340 + P312 - If inhaled: remove person to fresh air and keep comfortable for breathing; call a poison center/doctor if you feel unwell. P391 - Collect spillage. P501 - Dispose of contents/ container to an approved waste disposal plant.


**Table A.4.** Safety information for n-hexane

<b>Substance</b>	<b>n-hexane</b>
<b>Chemical Formula</b>	H <sub>3</sub> C(CH <sub>2</sub> ) <sub>4</sub> CH <sub>3</sub>
<b>Appearance</b>	Colourless liquid
<b>Pictograms</b>	
<b>Hazards Statements</b>	H225 - Highly flammable liquid and vapour. H361f - Suspected of damaging fertility. H373 - May cause damage to organs through prolonged or repeated exposure. H304 - May be fatal if swallowed and enters airways. H315 - Causes skin irritation. H336 - May cause drowsiness or dizziness. H411 - Toxic to aquatic life with long lasting effects.
<b>Precautionary Statements</b>	P201 - Obtain special instructions before use. P210 - Keep away from heat, hot surfaces, sparks, open flames and other ignition sources. No smoking. P243 - Take precautionary measures against static discharge. P280 - Wear protective gloves/protective clothing/eye protection/face protection. P273 - Avoid release to the environment. P301+P330+P331 - If swallowed: rinse mouth; do not induce vomiting. P302+P352 - If on skin: wash with plenty of water/... P304+P340 - If inhaled: remove person to fresh air and keep comfortable for breathing. P308+P310 - If exposed or concerned: immediately call a poison center/doctor. P403+P235 - Store in a well-ventilated place. Keep cool.


**Table A.5.** Safety information for ethanol

<b>Substance</b>	<b>Ethanol</b>
<b>Chemical Formula</b>	C <sub>2</sub> H <sub>6</sub> O
<b>Appearance</b>	Colourless clear liquid
<b>Pictograms</b>	
<b>Hazards Statements</b>	H225 - Highly flammable liquid and vapour. H319 - Causes serious eye irritation.
<b>Precautionary Statements</b>	P210 - Keep away from heat, hot surfaces, sparks, open flames and other ignition sources. No smoking. P280 - Wear eye protection/ face protection. P305 + P351 + P338 - If in eyes: rinse cautiously with water for several minutes; remove contact lenses, if present and easy to do; continue rinsing. P337 + P313 - If eye irritation persists: get medical advice/ attention. P403 + P235 - Store in a well-ventilated place. Keep cool.


**Table A.6.** Safety information for chloroform

<b>Substance</b>	<b>Chloroform</b>
<b>Chemical Formula</b>	CHCl <sub>3</sub>
<b>Appearance</b>	Colourless clear liquid
<b>Pictograms</b>	
<b>Hazards Statements</b>	H302 - Harmful if swallowed. H315 - Causes skin irritation. H319 - Causes serious eye irritation. H331 - Toxic if inhaled. H336 - May cause drowsiness or dizziness. H351 - Suspected of causing cancer. H361d - Suspected of damaging the unborn child. H372 - Causes damage to organs through prolonged or repeated exposure.
<b>Precautionary Statements</b>	P201 - Obtain special instructions before use. P260 - Do not breathe dust/ fume/ gas/ mist/ vapours/ spray. P264 - Wash skin thoroughly after handling. P280 - Wear protective gloves/ protective clothing/ eye protection/ face protection. P304 + P340 + P311 - If inhaled: remove person to fresh air and keep comfortable for breathing; call a poison center/doctor. P403 + P233 - Store in a well-ventilated place. Keep container tightly closed


**Table A.7.** Safety information for CTAB

<b>Substance</b>	<b>Hexadecyltrimethylammonium bromide (CTAB)</b>
<b>Chemical Formula</b>	C <sub>19</sub> H <sub>42</sub> BrN
<b>Appearance</b>	Solid
<b>Pictograms</b>	
<b>Hazards Statements</b>	H302 - Harmful if swallowed. H315 - Causes skin irritation. H318 - Causes serious eye damage. H335 - May cause respiratory irritation. H373 - May cause damage to organs (Gastrointestinal tract) through prolonged or repeated exposure if swallowed. H400 - Very toxic to aquatic life
<b>Precautionary Statements</b>	P260 - Do not breathe dust/ fume/ gas/ mist/ vapours/ spray. P280 - Wear eye protection/ face protection. P301 + P312 + P330 - If swallowed: call a poison center/doctor if you feel unwell; rinse mouth. P305 + P351 + P338 + P310 - If in eyes: rinse cautiously with water for several minutes; remove contact lenses, if present and easy to do; continue rinsing; immediately call a poison center/doctor.


**Table A.8.** Safety information for sodium hydroxide

<b>Substance</b>	<b>Sodium hydroxide</b>
<b>Chemical Formula</b>	NaOH
<b>Appearance</b>	White powder/pellets
<b>Pictograms</b>	
<b>Hazards Statements</b>	H290 - May be corrosive to metals. H314 - Causes severe skin burns and eye damage.
<b>Precautionary Statements</b>	P280 - Wear protective gloves/ protective clothing/ eye protection/ face protection. P303 + P361 + P353 - If on skin (or hair): take off immediately all contaminated clothing; rinse skin with water/shower. P304 + P340 + P310 - If inhaled: remove person to fresh air and keep comfortable for breathing; immediately call a poison center/doctor. P305 + P351 + P338 - If in eyes: rinse cautiously with water for several minutes; remove contact lenses, if present and easy to do; continue rinsing.


**Table A.9.** Safety information for ethyl acetate

<b>Substance</b>	<b>Ethyl acetate</b>
<b>Chemical Formula</b>	C <sub>4</sub> H <sub>8</sub> O <sub>2</sub>
<b>Appearance</b>	Clear colourless liquid
<b>Pictograms</b>	
<b>Hazards Statements</b>	H225 - Highly flammable liquid and vapour. H319 - Causes serious eye irritation. H336 - May cause drowsiness or dizziness.
<b>Precautionary Statements</b>	P210 - Keep away from heat/sparks/open flames/hot surfaces. No smoking. P261 - Avoid breathing dust/ fume/ gas/ mist/ vapours/ spray. P305 + P351 + P338 - If in eyes: rinse cautiously with water for several minutes; remove contact lenses, if present and easy to do; continue rinsing.


**Table A.10.** Safety information for TEOS

<b>Substance</b>	<b>Tetraethyl orthosilicate (TEOS)</b>
<b>Chemical Formula</b>	$C_8H_{20}O_4Si$
<b>Appearance</b>	Colourless liquid
<b>Pictograms</b>	
<b>Hazards Statements</b>	H226 - Flammable liquid and vapour. H319 - Causes serious eye irritation. H332 - Harmful if inhaled. H335 - May cause respiratory irritation.
<b>Precautionary Statements</b>	P210 - Keep away from heat, hot surfaces, sparks, open flames and other ignition sources. No smoking. P261 - Avoid breathing dust/ fume/ gas/ mist/ vapours/ spray. P280 - Wear eye protection/ face protection. P304 + P340 + P312 - If inhaled: remove person to fresh air and keep comfortable for breathing; call a poison center/doctor if you feel unwell. P337 + P313 - If eye irritation persists: Get medical advice/ attention. P403 + P235 - Store in a well-ventilated place. Keep cool.


**Table A.11.** Safety information for ammonium nitrate

<b>Substance</b>	<b>Ammonium Nitrate</b>
<b>Chemical Formula</b>	$NH_4NO_3$
<b>Appearance</b>	White crystals with lumps
<b>Pictograms</b>	
<b>Hazards Statements</b>	H272 - May intensify fire; oxidizer. H319 - Causes serious eye irritation.
<b>Precautionary Statements</b>	P210 - Keep away from heat, hot surfaces, sparks, open flames and other ignition sources. No smoking. P220 - Keep/Store away from clothing/ combustible materials. P221 - Take any precaution to avoid mixing with combustibles. P305 + P351 + P338 - If in eyes: rinse cautiously with water for several minutes; remove contact lenses, if present and easy to do; continue rinsing. P370 + P378 - In case of fire: use dry powder or dry sand to extinguish.


**Table A.12.** Safety information for acetic acid

<b>Substance</b>	<b>Acetic Acid</b>
<b>Chemical Formula</b>	$C_2H_4O_2$
<b>Appearance</b>	Colourless liquid
<b>Pictograms</b>	
<b>Hazards Statements</b>	H226 - Flammable liquid and vapour. H314 - Causes severe skin burns and eye damage.
<b>Precautionary Statements</b>	P280 - Wear protective gloves/ protective clothing/ eye protection/ face protection. P305 + P351 + P338 - If in eyes: rinse cautiously with water for several minutes; remove contact lenses, if present and easy to do; continue rinsing. P310 - Immediately call a poison center/doctor


**Table A.13.** Safety information for toluene

<b>Substance</b>	<b>Toluene</b>
<b>Chemical Formula</b>	C <sub>7</sub> H <sub>8</sub>
<b>Appearance</b>	Colourless liquid
<b>Pictograms</b>	
<b>Hazards Statements</b>	H225 - Highly flammable liquid and vapour. H304 - May be fatal if swallowed and enters airways. H315 - Causes skin irritation. H336 - May cause drowsiness or dizziness. H361d - Suspected of damaging the unborn child. H373 - May cause damage to organs through prolonged or repeated exposure.
<b>Precautionary Statements</b>	P210 - Keep away from heat, hot surfaces, sparks, open flames and other ignition sources. No smoking. P260 - Do not breathe dust/ fume/ gas/ mist/ vapours/ spray. P280 - Wear protective gloves/ protective clothing/ eye protection/ face protection. P301 + P310 - If swallowed: immediately call a poison center/doctor. P370 + P378 - In case of fire: use dry powder or dry sand to extinguish. P403 + P235 - Store in a well-ventilated place. Keep cool.
<b>Other health effects</b>	Drowsiness, irritant effects, dizziness, convulsions, headache, nausea, vomiting, circulatory collapse, somnolence, inebriation, unconsciousness, respiratory arrest, CNS disorders, death, respiratory paralysis.


**Table A.14.** Safety information for APTES

<b>Substance</b>	<b>(3-Aminopropyl)triethoxysilane (APTES)</b>
<b>Chemical Formula</b>	C <sub>9</sub> H <sub>23</sub> NO <sub>3</sub> Si
<b>Appearance</b>	Clear colourless liquid
<b>Pictograms</b>	
<b>Hazards Statements</b>	H302 - Harmful if swallowed. H314 - Causes severe skin burns and eye damage. H317 - May cause an allergic skin reaction.
<b>Precautionary Statements</b>	P260 - Do not breathe dust/ fume/ gas/ mist/ vapours/ spray. P280 - Wear protective gloves/ protective clothing/ eye protection/ face protection. P301 + P312 + P330 - If swallowed: call a poison center/doctor if you feel unwell; rinse mouth. P303 + P361 + P353 - If on skin (or hair): take off immediately all contaminated clothing; rinse skin with water/shower. P304 + P340 + P310 - If inhaled: remove person to fresh air and keep comfortable for breathing; immediately call a poison center/doctor. P305 + P351 + P338 - If in eyes: rinse cautiously with water for several minutes; remove contact lenses, if present and easy to do; continue rinsing.


**Table A.15.** Safety information for iron(II) chloride tetrahydrate

<b>Substance</b>	<b>Iron(II) chloride tetrahydrate</b>
<b>Chemical Formula</b>	FeCl <sub>2</sub> ·4H <sub>2</sub> O
<b>Appearance</b>	Light green crystals and fragments
<b>Pictograms</b>	
<b>Hazards Statements</b>	H302 - Harmful if swallowed. H314 - Causes severe skin burns and eye damage.
<b>Precautionary Statements</b>	P280 - Wear protective gloves/ protective clothing/ eye protection/ face protection. P305 + P351 + P338 - If in eyes: rinse cautiously with water for several minutes; remove contact lenses, if present and easy to do; continue rinsing. P310 - Immediately call a poison center or doctor/ physician


**Table A.16.** Safety information for iron(III) chloride hexahydrate

<b>Substance</b>	<b>Iron(III) chloride hexahydrate</b>
<b>Chemical Formula</b>	FeCl <sub>3</sub> ·6H <sub>2</sub> O
<b>Appearance</b>	Yellow solid
<b>Pictograms</b>	
<b>Hazards Statements</b>	H290 - May be corrosive to metals. H302 - Harmful if swallowed. H315 - Causes skin irritation. H318 - Causes serious eye damage.
<b>Precautionary Statements</b>	P280 - Wear protective gloves/ eye protection/ face protection. P305 + P351 + P338 - If in eyes: rinse cautiously with water for several minutes; remove contact lenses, if present and easy to do; continue rinsing.

**Table A.17.** Safety information for n-butanol

<b>Substance</b>	<b>n-Butanol</b>
<b>Chemical Formula</b>	C <sub>4</sub> H <sub>10</sub> O
<b>Appearance</b>	Clear colourless liquid
<b>Pictograms</b>	
<b>Hazards Statements</b>	H226 - Flammable liquid and vapour. H302 - Harmful if swallowed. H315 - Causes skin irritation. H318 - Causes serious eye damage. H335 - May cause respiratory irritation. H336 - May cause drowsiness or dizziness.
<b>Precautionary Statements</b>	P210 - Keep away from heat, hot surfaces, sparks, open flames and other ignition sources. No smoking. P280 - Wear eye protection/ face protection. P301 + P312 + P330 - If swallowed: call a poison center/doctor if you feel unwell; rinse mouth. P304 + P340 + P312 - If inhaled: remove person to fresh air and keep comfortable for breathing; call a poison center /doctor if you feel unwell. P305 + P351 + P338 + P310 - If in eyes: rinse cautiously with water for several minutes; remove contact lenses, if present and easy to do; continue rinsing; immediately call a poison center/doctor. P403 + P235 - Store in a well-ventilated place. Keep cool

**Table A.18.** Safety information for ammonium hydroxide

<b>Substance</b>	<b>Ammonium hydroxide</b>
<b>Chemical Formula</b>	NH <sub>4</sub> OH
<b>Appearance</b>	Clear colourless liquid
<b>Pictograms</b>	
<b>Hazards Statements</b>	H302 - Harmful if swallowed. H314 - Causes severe skin burns and eye damage. H335 - May cause respiratory irritation. H410 - Very toxic to aquatic life with long lasting effects.
<b>Precautionary Statements</b>	P260 - Do not breathe dust/ fume/ gas/ mist/ vapours/ spray. P280 - Wear protective gloves/ protective clothing/ eye protection/ face protection. P301 + P312 + P330 - If swallowed: call a poison center/doctor if you feel unwell; rinse mouth. P303 + P361 + P353 - If on skin (or hair): take off immediately all contaminated clothing; rinse skin with water/shower. P304 + P340 + P310 - If inhaled: remove person to fresh air and keep comfortable for breathing; immediately call a poison center/doctor. P305 + P351 + P338 - If in eyes: rinse cautiously with water for several minutes; remove contact lenses, if present and easy to do; continue rinsing.

**Table A.19.** Handling precautions with epirubicin solutions

<b>Substance</b>	<b>Epirubicin</b>
<b>Chemical Formula</b>	C <sub>27</sub> H <sub>29</sub> NO <sub>11</sub>
<b>Appearance</b>	Red solution
<b>Precautions</b>	Personnel handling epirubicin solutions should wear PVC gloves, safety glasses and protective clothing. If epirubicin solutions contact the skin or mucosa, the area should be washed with soap and water or sodium bicarbonate immediately; do not abrade the skin by using a scrub brush and always wash hands after removing gloves. In case of contact with the eye(s), hold back the eyelid of the affected eye(s) and flush with copious amounts of water for at least 15 minutes and proceed to a physician for medical evaluation. All items used, including gloves, should be placed in high-risk, waste disposal bags for high temperature incineration. Spillage or leakage should be treated with dilute sodium hypochlorite solution, preferably by soaking, and then water.



## APPENDIX B – VSM results of the IO-OAm/mSiO<sub>2</sub>\*-APD and IO-OAm/mSiO<sub>2</sub>\*-SCD nanoparticles

The magnetization curves at 1.8 K and 300 K obtained for the IO-OAm/mSiO<sub>2</sub>\* - APD and IO-OAm/mSiO<sub>2</sub>\* - SCD nanoparticles are presented in Figure B.1 and Figure B.2, respectively.

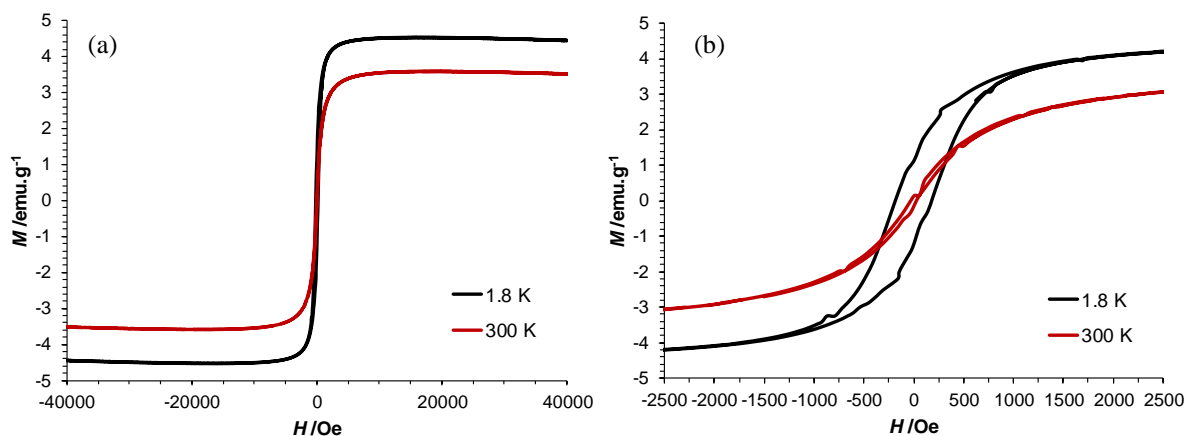


**Figure B.1.** (a) Magnetization curves of the IO-OAm/mSiO<sub>2</sub>\* - APD nanoparticles and (b) detailed view around the origin of the plot.

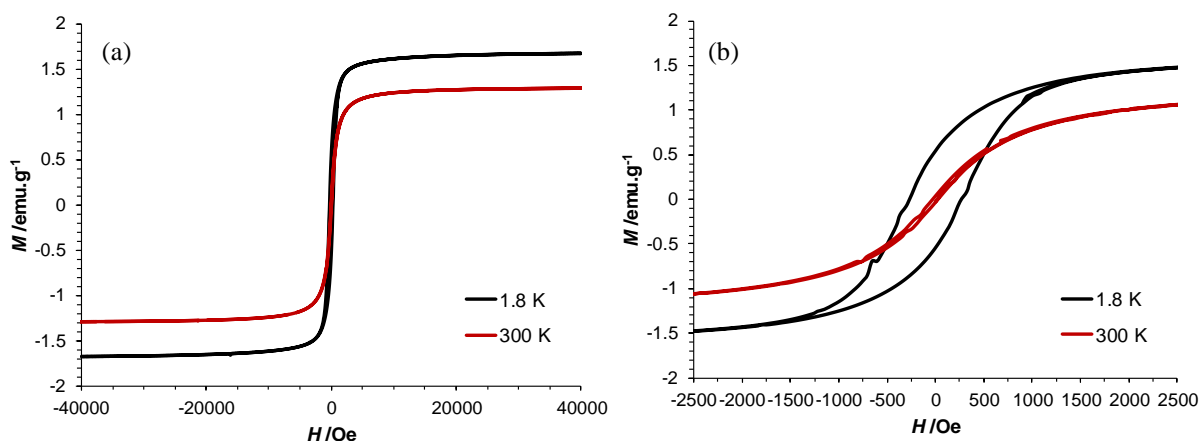


**Figure B.2.** (a) Magnetization curves of the IO-OAm/mSiO<sub>2</sub>\* - SCD nanoparticles and (b) detailed view around the origin of the plot.

In Figure B.1, it can be seen that the IO-OAm/mSiO<sub>2</sub>\* - APD nanoparticles have a saturation magnetization of 3.6 emu.g<sup>-1</sup> at 300 K and 4.5 emu.g<sup>-1</sup> at 1.8 K. Similarly, in Figure B.2, it can be observed that the saturation magnetization of the IO-OAm/mSiO<sub>2</sub>\* - SCD nanoparticles is 1.3 emu.g<sup>-1</sup> at 300 K and 1.7 emu.g<sup>-1</sup> at 1.8 K. The difference in the saturation magnetization between the two types of nanoparticles indicates that more oxidation occurs

during supercritical drying. Oxidation might have also happened during APD, but to a smaller extent, since high pressure and temperature are not used.

Looking at the detailed curves in Figure B.1.(b) and Figure B.2.(b), it can be observed that both nanoparticles present hysteresis at 1.8 K, but have no hysteresis at 300 K, confirming their superparamagnetic behaviour.

The FC and ZFC magnetization curves for these nanoparticles are presented in Figure B.3.

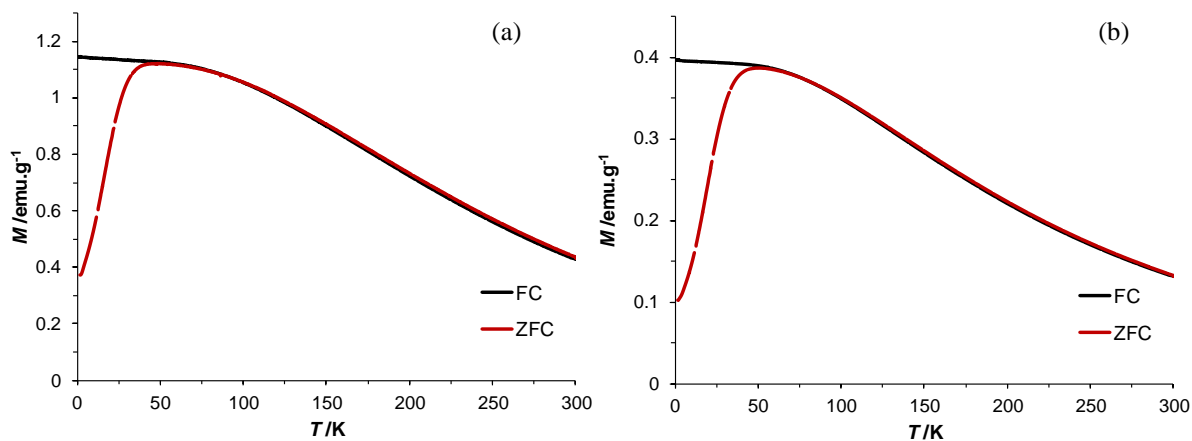


**Figure B.3.** FC and ZFC curves obtained with a magnetic field of 100 Oe for (a) the IO-OAm/mSiO<sub>2</sub>\*-APD and (b) IO-OAm/mSiO<sub>2</sub>\*-SCD nanoparticles.

From Figure B.3, it can be seen that the blocking temperature of both the IO-OAm/mSiO<sub>2</sub>\* - APD and the IO-OAm/mSiO<sub>2</sub>\* - SCD nanoparticles is around 50 K, which means that below this temperature their superparamagnetic behaviour ceases to occur.

## APPENDIX C – Additional data of the loading experiments

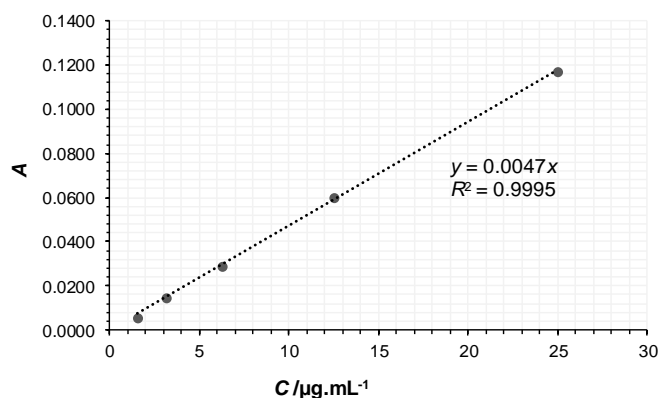


**Figure C.1.** Calibration curve used in quantification 1/ loading A of the IO-OAm/mSiO<sub>2</sub> nanoparticles and quantification 2/ loading A of the IO-APTES/mSiO<sub>2</sub> nanoparticles.

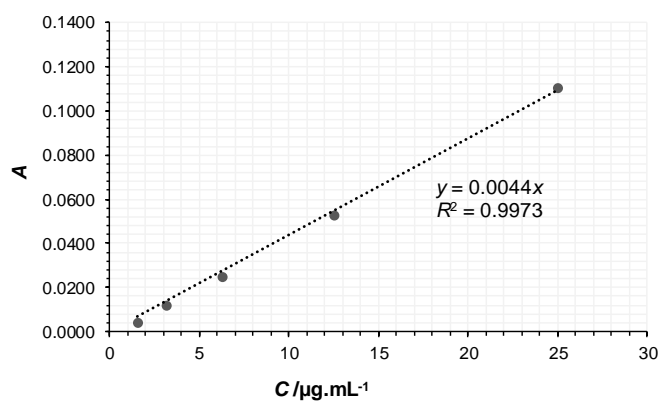


**Figure C.2.** Calibration curve used in quantification 2/ loading A and quantification 1/ loading B of the IO-OAm/mSiO<sub>2</sub> nanoparticles and in quantification 3/ loading A and quantification 1/ loading B of the IO-APTES/mSiO<sub>2</sub> nanoparticles.

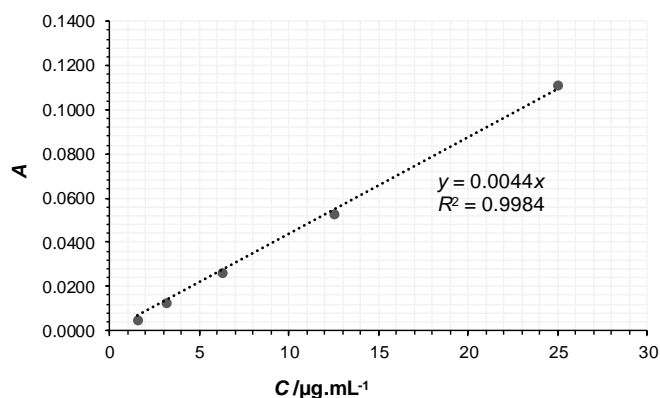


**Figure C.3.** Calibration curve used in quantification 3/ loading A and quantification 2/ loading B of the IO-OAm/mSiO<sub>2</sub> nanoparticles, in quantification 2/ loading B of the IO-APTES/mSiO<sub>2</sub> nanoparticles and in quantification 1 of loading of the IO/SiO<sub>2</sub>/mSiO<sub>2</sub> nanoparticles.

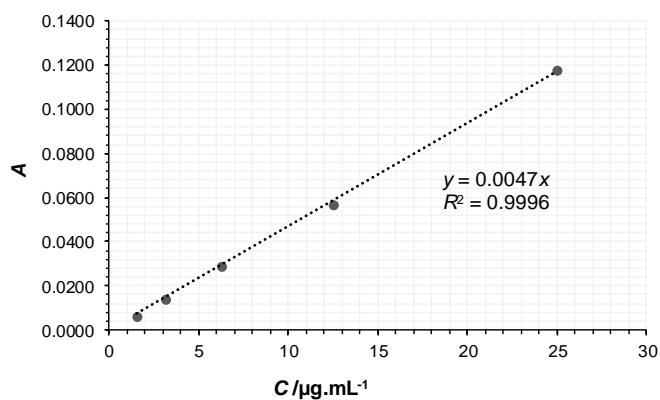


**Figure C.4.** Calibration curve used in quantification 3/ loading B of the IO-OAm/mSiO<sub>2</sub> nanoparticles and in quantification 3/ loading B of IO-APTES/mSiO<sub>2</sub> nanoparticles.

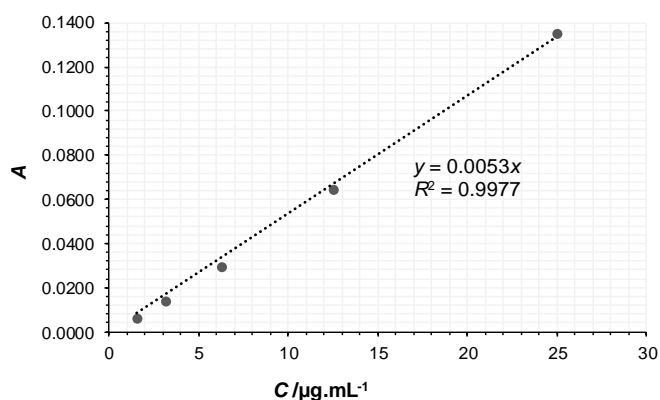


**Figure C.5.** Calibration curve used in quantification 1/ loading A of the IO-APTES/mSiO<sub>2</sub> nanoparticles.

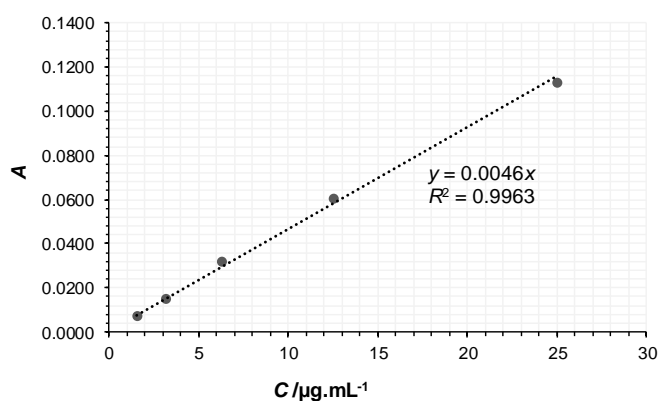


**Figure C.6.** Calibration curve used in quantification 2 of loading of the IO/SiO<sub>2</sub>/mSiO<sub>2</sub> nanoparticles.

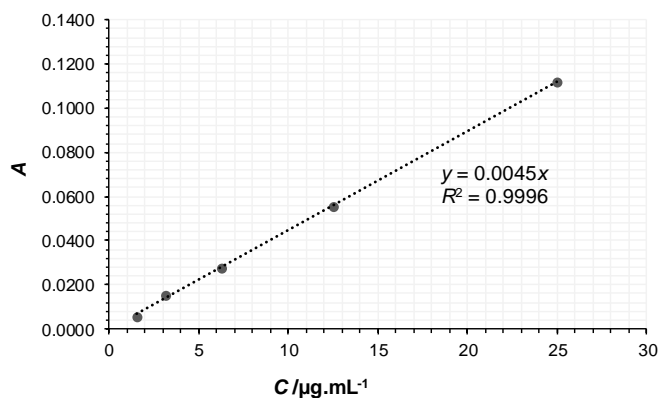


**Figure C.7.** Calibration curve used in quantification 3 of loading of the IO/SiO<sub>2</sub>/mSiO<sub>2</sub> nanoparticles.

**Table C.1.** Results obtained for loading A of the IO-OAm/mSiO<sub>2</sub> nanoparticles.

Supernatant	V /mL	Quantification 1			Quantification 2			Quantification 3		
		A	C /μg.mL <sup>-1</sup>	m <sub>EPI</sub> /μg	A	C /μg.mL <sup>-1</sup>	m <sub>EPI</sub> /μg	A	C /μg.mL <sup>-1</sup>	m <sub>EPI</sub> /μg
1	5.00	0.1046	22.26	2226	0.0990	22.49	2249	0.0980	22.28	2228
2	5.00	0.0048	1.03	103	0.0037	0.84	84	0.0045	1.03	102
3	5.00	0.0010	0.22	22	0.0001	0.02	2	0.0007	0.16	16
<b>Total</b>				2351			2336			2347
<b>Calibration Curve</b>		A=0.0047C (R <sup>2</sup> =0.9995)			A=0.0044C (R <sup>2</sup> =0.9973)			A=0.0044C (R <sup>2</sup> =0.9984)		

**Table C.2.** Results obtained for loading B of the IO-OAm/mSiO<sub>2</sub> nanoparticles.

Supernatant	V /mL	Quantification 1			Quantification 2			Quantification 3		
		A	C /μg.mL <sup>-1</sup>	m <sub>EPI</sub> /μg	A	C /μg.mL <sup>-1</sup>	m <sub>EPI</sub> /μg	A	C /μg.mL <sup>-1</sup>	m <sub>EPI</sub> /μg
1	4.95	0.1033	23.48	2325	0.1012	23.01	2278	0.1064	22.64	2241
2	4.90	0.0019	0.42	42	0.0022	0.49	49	0.0042	0.89	87
3	5.00	3x10 <sup>-5</sup>	0.01	1	0.0006	0.13	13	0.0006	0.13	13
<b>Total</b>				2391			2340			2341
<b>Calibration Curve</b>		A=0.0044C (R <sup>2</sup> =0.9973)			A=0.0044C (R <sup>2</sup> =0.9984)			A=0.0047C (R <sup>2</sup> =0.9996)		

**Table C.3.** Results obtained for loading A of IO-APTES/mSiO<sub>2</sub> nanoparticles.

Supernatant	V /mL	Quantification 1			Quantification 2			Quantification 3		
		A	C /μg.mL <sup>-1</sup>	m <sub>EPI</sub> /μg	A	C /μg.mL <sup>-1</sup>	m <sub>EPI</sub> /μg	A	C /μg.mL <sup>-1</sup>	m <sub>EPI</sub> /μg
1	5.00	0.1175	22.17	2217	0.1008	21.45	2145	0.1007	22.88	2288
2	5.00	0.0044	0.84	84	0.0045	0.96	96	0.0022	0.51	51
3	5.00	0.0008	0.14	14	0.0010	0.21	21	0.0001	0.02	2
<b>Total</b>				2315			2260			2341
<b>Calibration Curve</b>		A=0.0053C (R <sup>2</sup> =0.9977)			A=0.0047C (R <sup>2</sup> =0.9995)			A=0.0044C (R <sup>2</sup> =0.9973)		

**Table C.4.** Results obtained for loading B of IO-APTES/mSiO<sub>2</sub> nanoparticles.

Supernatant	V /mL	Quantification 1			Quantification 2			Quantification 3		
		A	C /μg.mL <sup>-1</sup>	m <sub>EPI</sub> /μg	A	C /μg.mL <sup>-1</sup>	m <sub>EPI</sub> /μg	A	C /μg.mL <sup>-1</sup>	m <sub>EPI</sub> /μg
1	5.00	0.1016	23.08	2308	0.1007	22.89	2289	0.1097	23.34	2334
2	5.00	0.0019	0.42	42	0.0016	0.36	36	0.0024	0.51	51
3	5.00	0.0005	0.13	13	0.0009	0.20	20	1.4x10 <sup>-5</sup>	3x10 <sup>-3</sup>	0
<b>Total</b>				2363			2345			2386
<b>Calibration Curve</b>		A=0.0044C (R <sup>2</sup> =0.9973)			A=0.0044C (R <sup>2</sup> =0.9984)			A=0.0047C (R <sup>2</sup> =0.9996)		

**Table C.5.** Results of the loading of the IO/SiO<sub>2</sub>/mSiO<sub>2</sub> particles.

Supernatant	V /mL	Quantification 1			Quantification 2			Quantification 3		
		A	C /μg.mL <sup>-1</sup>	m <sub>EPI</sub> /μg	A	C /μg.mL <sup>-1</sup>	m <sub>EPI</sub> /μg	A	C /μg.mL <sup>-1</sup>	m <sub>EPI</sub> /μg
1	4.90	0.1014	23.04	2258	0.1065	23.16	2270	0.0969	21.52	2109
2	4.90	0.0023	0.53	51	0.0028	0.61	61	0.0061	1.36	133
3	5.00	0.0007	0.16	16	0.0001	0.03	3	0.0042	0.93	93
<b>Total</b>				2326			2334			2335
<b>Calibration Curve</b>		A=0.0044C (R <sup>2</sup> =0.9984)			A=0.0046C (R <sup>2</sup> =0.9963)			A=0.0045C (R <sup>2</sup> =0.9996)		

## APPENDIX D – Additional data of the release experiments

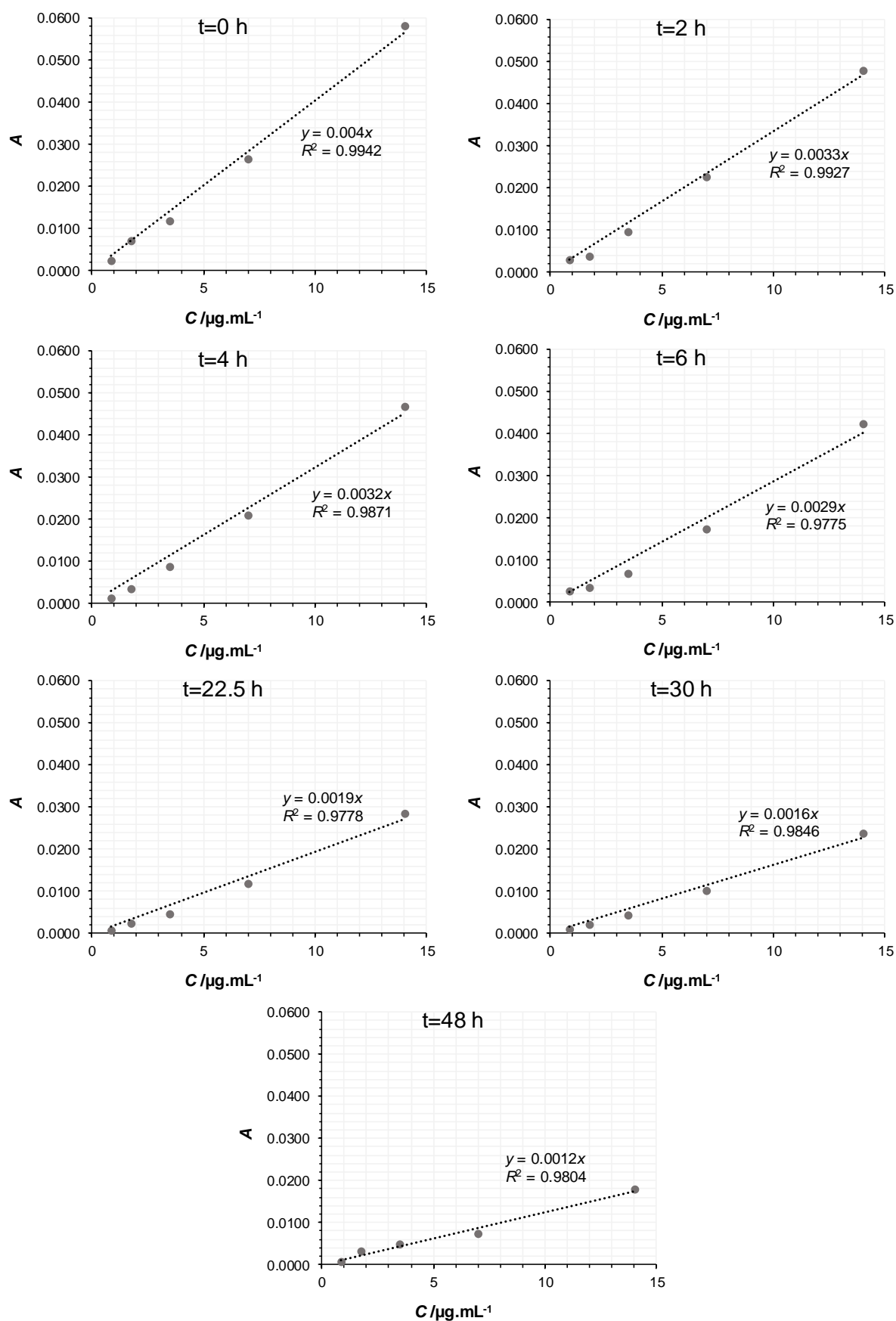


Figure D.1. Calibration curves obtained for each time point of the release experiments.

**Table D.1.** Results for the first sample of the release experiments of the IO-OAm/mSiO<sub>2</sub> nanoparticles.

$t/h$	$A$	$C$ / $\mu\text{g.mL}^{-1}$	$V_{\text{lost}}/\text{mL}$	$m_{\text{lost}}/\mu\text{g}$	$m/\mu\text{g}$	EPI released /%
2	0.0053	1.62	0.010	0.0162	3.25	11.5
4	0.0057	1.78	0.010	0.0178	3.56	12.7
6	0.0049	1.69	0.012	0.0202	3.38	12.0
22.5	0.0052	2.76	0.014	0.0386	5.47	19.4
30	0.0045	2.84	0.010	0.0284	5.63	20.0
48	0.0038	3.17	-	-	6.27	22.3

**Table D.2.** Results for the second sample of the release experiments of the IO-OAm/mSiO<sub>2</sub> nanoparticles.

$t/h$	$A$	$C$ / $\mu\text{g.mL}^{-1}$	$V_{\text{lost}}/\text{mL}$	$m_{\text{lost}}/\mu\text{g}$	$m/\mu\text{g}$	EPI released /%
2	0.0049	1.50	0.010	0.0150	3.07	11.5
4	0.0036	1.14	0.012	0.0136	2.36	8.9
6	0.0036	1.24	0.010	0.0124	2.56	9.6
22.5	0.0038	2.02	0.010	0.0202	4.08	15.3
30	0.0039	2.46	0.010	0.0246	4.94	18.5
48	0.0027	2.25	-	-	4.54	17.0

**Table D.3.** Results for the third sample of the release experiments of the IO-OAm/mSiO<sub>2</sub> nanoparticles.

$t/h$	$A$	$C$ / $\mu\text{g.mL}^{-1}$	$V_{\text{lost}}/\text{mL}$	$m_{\text{lost}}/\mu\text{g}$	$m/\mu\text{g}$	EPI released /%
2	0.0035	1.06	0.010	0.0106	2.13	7.2
4	0.0032	1.00	0.008	0.0080	2.01	6.8
6	0.0067	2.30	0.010	0.0230	4.57	15.6
22.5	0.0040	2.08	0.006	0.0125	4.15	14.1
30	0.0025	1.54	0.009	0.0138	3.07	10.5
48	0.0032	2.63	-	-	5.22	17.8

**Table D.4.** Results for the first sample of the release experiments of the IO-APTES/mSiO<sub>2</sub> nanoparticles.

$t/h$	$A$	$C$ / $\mu\text{g.mL}^{-1}$	$V_{\text{lost}}/\text{mL}$	$m_{\text{lost}}/\mu\text{g}$	$m/\mu\text{g}$	EPI released /%
2	0.0040	1.20	0.012	0.0144	2.41	7.8
4	0.0048	1.50	0.010	0.0150	3.00	9.7
6	0.0062	2.14	0.012	0.0257	4.27	13.9
22.5	0.0063	3.29	0.010	0.0329	6.53	21.2
30	0.0045	2.82	0.012	0.0338	5.60	18.2
48	0.0046	3.84	-	-	7.58	24.6

**Table D.5.** Results for the second sample of the release experiments of the IO-APTES/mSiO<sub>2</sub> nanoparticles.

$t/h$	$A$	$C$ / $\mu\text{g.mL}^{-1}$	$V_{\text{lost}}/\text{mL}$	$m_{\text{lost}}/\mu\text{g}$	$m/\mu\text{g}$	EPI released /%
2	0.0042	1.28	0.012	0.0154	2.56	8.3
4	0.0055	1.72	0.010	0.0172	3.43	11.1
6	0.0062	2.12	0.012	0.0255	4.23	13.7
22.5	0.0063	3.31	0.010	0.0331	6.55	21.3
30	0.0057	3.57	0.012	0.0428	7.05	22.9
48	0.0052	4.30	-	-	8.46	27.5



**Table D.6.** Results for the third sample of the release experiments of the IO-APTES/mSiO<sub>2</sub> nanoparticles.

<i>t</i> /h	<i>A</i>	<i>C</i> /μg.mL <sup>-1</sup>	<i>V</i> <sub>lost</sub> /mL	<i>m</i> <sub>lost</sub> /μg	<i>m</i> /μg	EPI released /%
2	0.0039	1.19	0.014	0.0167	2.38	8.2
4	0.0061	1.92	0.009	0.0173	3.81	13.1
6	0.0076	2.64	0.030	0.0791	5.21	17.9
22.5	0.0051	2.71	0.010	0.0271	5.34	18.3
30	0.0048	3.03	0.010	0.0303	5.96	20.4
48	0.0043	2.71	-	-	5.43	18.6

**Table D.7.** Results for the first sample of the release experiments of the IO/SiO<sub>2</sub>/mSiO<sub>2</sub> nanoparticles.

<i>t</i> /h	<i>A</i>	<i>C</i> /μg.mL <sup>-1</sup>	<i>V</i> <sub>lost</sub> /mL	<i>m</i> <sub>lost</sub> /μg	<i>m</i> /μg	EPI released /%
2	0.0072	2.17	0.010	0.0217	4.34	15.7
4	0.0089	2.78	0.008	0.0223	5.56	20.2
6	0.0094	3.23	0.010	0.0323	6.44	23.3
22.5	0.0071	3.71	0.006	0.0223	7.40	26.8
30	0.0069	4.29	0.009	0.0386	8.52	30.9
48	0.0057	4.71	-	-	9.36	33.9

**Table D.8.** Results for the second sample of the release experiments of the IO/SiO<sub>2</sub>/mSiO<sub>2</sub> nanoparticles.

<i>t</i> /h	<i>A</i>	<i>C</i> /μg.mL <sup>-1</sup>	<i>V</i> <sub>lost</sub> /mL	<i>m</i> <sub>lost</sub> /μg	<i>m</i> /μg	EPI released /%
2	0.0079	2.38	0.010	0.0238	4.76	17.9
4	0.0083	2.58	0.008	0.0206	5.15	19.4
6	0.0082	2.81	0.010	0.0281	5.61	21.1
22.5	0.0064	3.37	0.006	0.0202	6.72	25.3
30	0.0059	3.66	0.009	0.0329	7.28	27.4
48	0.0047	3.91	-	-	7.77	29.3

**Table D.9.** Mean values obtained for the percentage of EPI released in the different nanoparticles.

<i>t</i> /h	EPI released /%		
	IO-OAm/mSiO <sub>2</sub>	IO-APTES/mSiO <sub>2</sub>	IO/SiO <sub>2</sub> /mSiO <sub>2</sub>
2	10.1±2.5	8.1±0.3	16.8±1.6
4	9.4±3.0	11.3±1.7	19.8±0.5
6	12.4±3.0	15.2±2.3	22.2±1.5
22.5	16.3±2.8	20.3±1.7	26.1±1.1
30	16.3±5.1	20.5±2.4	29.2±2.4
48	19.0±2.8	23.6±4.5	31.6±3.3